Performance Study of MUCH (detector) of CBM Experiment at FAIR

THESIS

SUBMITTED FOR THE AWARD OF THE DEGREE OF

Doctor of Philosophy

In

Physics

By

HusHnud

Under The Supervision Of

Dr. Nazeer Ahmad

Department of Physics
Aligarh Muslim University
Aligarh -202002, INDIA
2015

Candidate's Declaration

I, ***Hushnud***, Department of Physics, Aligarh Muslim University, Aligarh certify that the work embodied in this Ph.D. thesis is my own bonafide work carried out by me under the supervision of ***Dr. Nazeer Ahmad*** at the Department of Physics, Aligarh Muslim University, Aligarh. The matter embodied in this Ph.D. thesis has not been submitted for the award of any other degree.

I declare that I have faithfully acknowledged, given credit to and referred to the research workers wherever their works have been cited in the text and the body of the thesis. I further certify that I have not willfully lifted up some other's works, paragraph, text, data, result, etc., reported in the journals, books, magazines, reports, dissertations, thesis, etc., or available at web-sites and included them in this Ph.D. thesis and cited as my own work.

Date: ……………………

(Hushnud)

……………………………………………………………………………………………………

Certificate from the Supervisor

This is to certify that the above statement made by the candidate is correct to the best of my knowledge.

Signature of the Supervisor : ……………….…………..

Name and Designation : Dr. Nazeer Ahmad (Assistant Professor)

Department : Physics, A. M. U., Aligarh

(Signature of the Chairman of the Department with seal)

Course / Comprehensive Examination / Pre-Submission Seminar Completion Certificate

---

This is to certify that **Ms. Hushnud**, Department of Physics, Aligarh Muslim University, Aligarh has satisfactorily completed the Course Work/Comprehensive examination and Pre-submission Seminar requirement, which is part of her Ph.D. programme.

Date:……………… **(Signature of the Chairman of the Department)**

Copyright Transfer Certificate

Title of the Thesis : **Performance Study of MUCH (detector) of CBM Experiment at FAIR**

Candidate's Name : **HUSHNUD**

Copyright Transfer

The undersigned hereby assigns to the Aligarh Muslim University, Aligarh copyright that may exist in and for the above thesis submitted for the award of the Ph.D. degree.

Signature of the candidate

Note: However, the author may reproduce or authorize others to reproduce material extracted verbatim from the thesis or derivative of the thesis for author's personal use provide that the source and the University's copyright notice are indicated.

Dedicated
To my
Beloved Parents

Acknowledgement

First and foremost, all praise to Allah, the Almighty, the Merciful, the Beneficent and the Omniscient Whose Blessings and Mercy enabled me to complete this thesis in the present form within the stipulated time period.

It is indeed my privilege and pleasure to express my profound sense of gratitude to my Supervisor, Dr. Nazeer Ahmad Assistant Professor, Department of Phyiscs, for not only being dedicated and persevering but also for his guidance, unflinching encouragement and support in umpteen number of ways throughout my work. I must appreciate him for his great involvement, moral support, constructive criticism and sympathetic attitude, which enabled me to complete this work.

My sincere thanks are due to Dr. Subhasis Chattopadhayay , an eminent Scientist of experimental high energy physics, VECC, Kolkata for his invaluable suggestions and timely help in the completion of my analysis work.

It is also my bound duty to express my gratitude to Professor Rahimullah Khan, Ex-Chairman and Professor M. Afzal Ansari, Chairman, Department of Physics, Aligarh Muslim University, Aligarh, for providing all the possible research facilities throughout this work.

I would like to acknowledge Professor Muhammad Irfan, sir, for his generous support and encouragement. I am very much indebted to him for his constant motivation and deep insights and knowledge of the subject. I would like to extend my thanks for his patience with which he dealt me; his critical remarks and valuable suggestions are also appreciated.

I am particularly indebted to Dr. M. Danish Azmi, Dr.M. Mohshin Khan, Mr. Mohammad Tariq, Mr. Tahir Hussain, Dr. Kushal Das and Kausar Saleem for their valuable suggestions, keen interest and encouragement.

I am grateful to the colleagues of CBM Collaboration, who helped me in the completion of Ph.D. thesis. I especially thank Professor Peter Senger, Spokesperson of CBM Collaboration, Dr. Volker Friese, Dr. Ana Senger, Dr. Iouri Vasliev and all other collaborators, who immensely helped me in interpreting the results of the simulation studies.

My affectionate and sincere thanks are due to my senior research colleagues and well-wishers, who encouraged me throughout this work. I am especially grateful to Ms. Hala, Ms. Huma Haider and Mrs. Fainana Mustajab for sharing ideas and creating a healthy academic environment.

I am fortunate enough to have friends like Ms. Shahla Jameel, Mrs. Tarrannum Afrin, Ms. Shabista Bano, Ms. Himanshu Gupta, Afsana 'Aapa', Nishat ' Appa', Farhat 'Aapa', Mrs. Shabana Khan, Mrs. Amna Ali, Mrs. Ritu Sharma, Mrs. Fauzia Haseeb, Ms. Jaya and Ms. Samiya Manzoor, whom I always found standing by my side, especially when I needed them the most. I thank my room-partner, Mrs. Sanam Haseen with whom I always felt at home, away from home.

I am grateful to Mr. Shabir Ahmad (KU) and Mr. Kalyan Dey (GU) for their constant help, support and timely suggestions throughout my analysis work. I also thank Dr. P. P. Bhaduri (SO), Mrs. Maityree Mukharjee, Ms. Shabnam Mohsina, Mr. Sumit Basu (VECC), Ms. Nirupama Sen Sharma (DU), Ms. Rohini Sharrma (JU), Mr. Waseem Raja, Mr. Firdous Ahmad and Ms. Surraiyya Bashir (KU) for their help, support and good wishes.

I sincerely thank all the non-teaching staff of the Department of Physics, AMU, for their affection and kind co-operation.

I have no words to express my gratitude to my parents, two brothers, sisters-in-law, two sisters, brother-in-law and close friends for bearing with me throughout my Ph.D work. I shall always remain indebted to them for their unstinting support.

I am thankful to UGC and DST, Govt. of India for the financial support to pursue research programme, culminating in the completion of my Ph.D. thesis.

Hushnud

Contents

Preface

Facility for Antiproton and Ion Research (FAIR) is an accelerator facility for research with antiprotons and ions, proposed to be created in the coming years at GSI, Darmstadt, Germany. Heavy-ion beams of unique quality, high intensities of up to 10^9 $ions/s$ and widely different energies (E_{Lab} = 2 - 40 $AGeV$), will be delivered by Superconducting Synchrotrons, SIS100 and SIS300, with bending powers of 100 and 300 Tm respectively. The accelerators at FAIR will deliver ion beams in two-stages depending on the availability of the accelerators (SIS100 and SIS300). It will provide a unique opportunity to study the QCD phase diagram in the domain of moderate temperatures and high baryonic densities. These conditions are achievable in the Compressed Baryonic Matter (CBM) experiment. The CBM experiment program will investigate the occurrence of the novel phase transition from hadronic to quarkyonic matter or quark-gluon plasma, onset of chiral symmetry restoration and equation-of-state of nuclear matter; a critical point of the superdense baryonic matter will also be searched for. The CBM physics program is essentially complementary to the heavy-ion researches being conducted at Relativistic Heavy Ion Collider (RHIC), BNL, USA and Large Hadron Collider (LHC), CERN, Geneva, Switzerland, which explore Quantum Chromodynamics (QCD) phase diagram of nuclear matter at extremely high temperatures and/or low net baryonic densities.

The main aim of the research programs of the CBM experiment is to measure diagnostic rare probes of the early and dense phase of the fireball evolution such as production of charmed mesons (low production cross section), multi-strange hyperons and lepton pairs created by the decays of low mass vector mesons (LMVM) having small branching ratios. Due to extremely low values of these observables, they are referred to as rare probes. The CBM experiment will be performed in the fixed-target mode and will measure

e^+e^-, $\mu^+\mu^-$, photons and charged hadrons. Their measurements require fast detector systems, capable of handling high interaction rates of up to 10 MHz. These experimental constraints have led to the development of ultra-fast and radiation hard detectors, free streaming readout electronics, an ultra-fast online event-selection, and high-speed data acquisition (DAQ) and processing system. A particular challenge faced by the detectors, the front-end electronics and the data acquisition is to perform a high-speed online tracking and selection of displaced vertices with high precision, which is essentially required for open charm measurements.
The thesis is organized as described below:

Chapter 1 gives an introduction to the high-energy heavy-ion physics. It begins with a general description of quarks and their interactions. A brief description of the phase diagram of strongly interacting matter is also presented. The details of the experiments done in the past and ongoing heavy-ion experiments are given. Finally, details of future CBM experiments to be performed at FAIR are presented.

Chapter 2 introduces FAIR accelerator facility and the CBM experiment. The outlines of the CBM experiment physics programs along with the observables are given in this chapter.

FAIR comprises of two superconducting synchrotrons, SIS100 and SIS300, SIS100 will deliver beams of 11 $AGeV$ gold nuclei, 14 $AGeV$ light nuclei and 29 GeV protons and SIS300 will produce beams of 89 GeV protons, 35 $AGeV$ gold nuclei and light nuclei of 45 $AGeV$ energy. These beams shall be used by the CBM experiment to study various physics phenomena.

The *yields, collective flow and phase space distributions* of hadrons will provide information about *equation-of-state* of nuclear matter over a wide range of net baryonic densities. Study of *anomalous charmonia suppression and strangeness enhancement* will help in search of the *phase transition* from hadronic to deconfined state of nuclear matter at high net baryonic density. A precise measurement of *dilepton invariant mass spectrum* up to 1 *GeV* will provide information about the in-medium properties of vector mesons such as, ρ^0, ω^0, ϕ^0, etc., spectral function, which is a signal of the *chiral symmetry restoration* in the hot and dense medium. Study of *event-by-event fluctuations* of charged particle number, baryon number, ratio of the yields of strange hadrons and pions (K/π), average transverse momentum, etc., will provide information about the location of *QCD critical point.*

Chapter 3 starts with the description of the CBM experiment. The detector will measure bulk hadrons, multi-strange hyperons, hypernuclei with high accuracy and statistics despite their low multiplicities, which require a detector system of larger acceptance for handling high interaction rates. The proposed CBM experiment consists of the following sub-detectors: Silicon Tracking System (STS), Micro-Vertex Detector (MVD), Time-of-Flight (TOF) detector, Ring Imaging Cherenkov (RICH) detector, Transition Radiation Detector (TRD) , Muon Chamber (MuCh), Electromagnetic Calorimeter (ECAL) and Projectile Spectator Detector (PSD).

The STS, placed inside the superconducting dipole magnet, is the central part of the CBM experiment detector set-up, which will measure the trajectories of the produced charged particles and their momenta. The dipole magnet will provide a vertical magnetic field with a bending power of 1 Tm over a length of 1 m from the target. MVD measures secondary vertices of charmed hadrons with high accuracy. TOF containing RPC walls will help in identifying the hadrons. RICH will be used for the identification of e^+e^- pairs coming from the decays of LMVM. TRD will be used to match tracks reconstructed in the STS and TOF measurements. MuCh will identify muons created by the decays of charmonia and LMVM. ECAL is deployed for the measurement of photons coming from the decays of LMVM and PSD is used for determining collision centrality and reaction plane of the projectile spectators.

In **Chapter 4** the details of optimization of the detector set-up for muon identification are presented. The CBM experiment basically aims to measure rare probes such as charmonia (J/Ψ, Ψ', etc.) with low production cross sections, and LMVM with low branching ratios, at the FAIR energies. Both of these can be measured through their decays to dimuons. Hence, muon detection system, Muon Chambers, are required for their detection. Depending upon the energy, two sets of MuCh, SIS100 having 3 (SIS100-A) or 4 (SIS100-B) absorbers and SIS300 with 6 absorbers, will be fabricated. The MuCh consists of alternate layers of segmented absorbers and triplets of tracking chambers, with first few tracking chambers made up of GEM.

Systematic simulation studies have been performed for optimizing the values of the various parameters. These parameters are : number, thickness and material of the absorber and number and granularity of the tracking chambers, required for the fabrication of MuCh detector set-up. The optimization of the detector set-up has been done in the CBMRoot framework, which allows full event simulation and reconstruction. The simulation chain followed is : (a) generation of signal particles (LMVM and J/Ψ) by PLUTO and background particles by UrQMD, whereas the number of signal mesons are obtained using HSD transport code, (b) generated particles are transported through the detector set-up by employing GEANT3 transport engines, (c) the detector set-up is segmented into small segments called pads and digitization scheme has been implemented for the creation of digits, (d) digits are grouped into clusters and then deconvoluted into hits, (e) tracks are reconstructed by *cellular automaton* method, propagated by *Kalman-Filter* technique, *nearest-neighbour* and *branching method* has been implemented for track finding, and finally track selection is based on sorting by χ^2 of tracks and vertex finding and (f) selection of the muon candidates is done on the basis of following cuts : (i) number of hits in STS layers; (ii) number of hits in MuCh layers; (iii) χ^2_{vertex}/d.o.f for STS track segments and (iv) χ^2/d.o.f for MuCh track segments. The selection of the number of MuCh stations will help in determining whether the muons coming from LMVM or charmonia. The muons arising from the decays of

LMVM will travel shorter distances in comparison to those coming from J/Ψ decays, which crosses the thick absorber and reach up to the last station. The required number of MuCh hits for the muons from LMVM decays will not exceed 15 for the SIS300 set-up and 11 for the SIS100 set-up. However, for the case of muons coming from decays of J/Ψ, should have at least 16 MuCh hits for the SIS300 set-up and 12 hits for the SIS100 set-up.

In **Chapter 5** the details of the optimized detector set-up for the SIS100 energy (8 $AGeV$) used for performing a feasibility study of ω^0 meson are given. One million embedded signal ω^0 meson are generated by employing PLUTO generator, whereas, unembedded background events are produced by UrQMD model in Au+Au collisions at 8 $AGeV$. The invariant mass distribution of both signal and background has been plotted. This study indicates that LMVM can be identified above the combinatorial background, which is dominated by the muons from meson decays.

This chapter also gives the details of segmentation optimization of MuCh. The segmentation study is important for : (i) determining occupancy ($\sim 5\%$) and multi-hit probability for measurement of tracking and efficiency of muons, (ii) total number of pads for the estimation of cost and (iii) dimensions of the pads needed for the fabrication and estimation of signal strength. Hence, a simulation study has been performed by employing one million signal embedded in the background at 8 $AGeV$ for SIS100 set-up and varying the azimuthal angle from 0.4 to 1.2°. This study is based on the effect of segmentation angle on the following parameters : (a) *hit density* and *occupancy*, which will help to estimate the maximum hit rate and data taking rate of the tracking chambers, (b) *efficiency* and *signal to background ratio* for investigating the performance of the MuCh for detection of ω^0 meson by using the real detector set-up.

Chapter 6 presents the results of the study of the production of the multi-strange particles at the FAIR energies. These results are obtained by exploiting the transport models, AMPT and UrQMD, for one million event in central Au

+ Au collisions in the FAIR energy range. The motivation behind the present study is essentially the realization that at lower energies net baryon densities of up to 5 - 6 times the normal nuclear matter density are attainable. Such high baryon densities lead to deconfinment of hadrons into quarks. Under such conditions enhanced production of s and $\bar{s}$ quarks takes place, which leads to higher production of strange hadrons after the freeze-out.

Strangeness enhancement, especially of multi-strange hyperons, is therefore, one of the proposed signatures of the QGP formation. As experimental data on the production of multi-strange hyperons in the FAIR energy range is scarce, it is, therefore, considered an important physics issue to be addressed by the CBM experiment. Average yields of multi-strange hyperons and the ratios of the average yields of multi-strange hyperons and pions are determined and compared with the available experimental data at AGS and SPS energies.

Chapter 7 contains the summary and outlook on the basis of the findings of the study presented in this thesis. It provides some insights into the possible activities at FAIR.

List of Figures

List of Tables

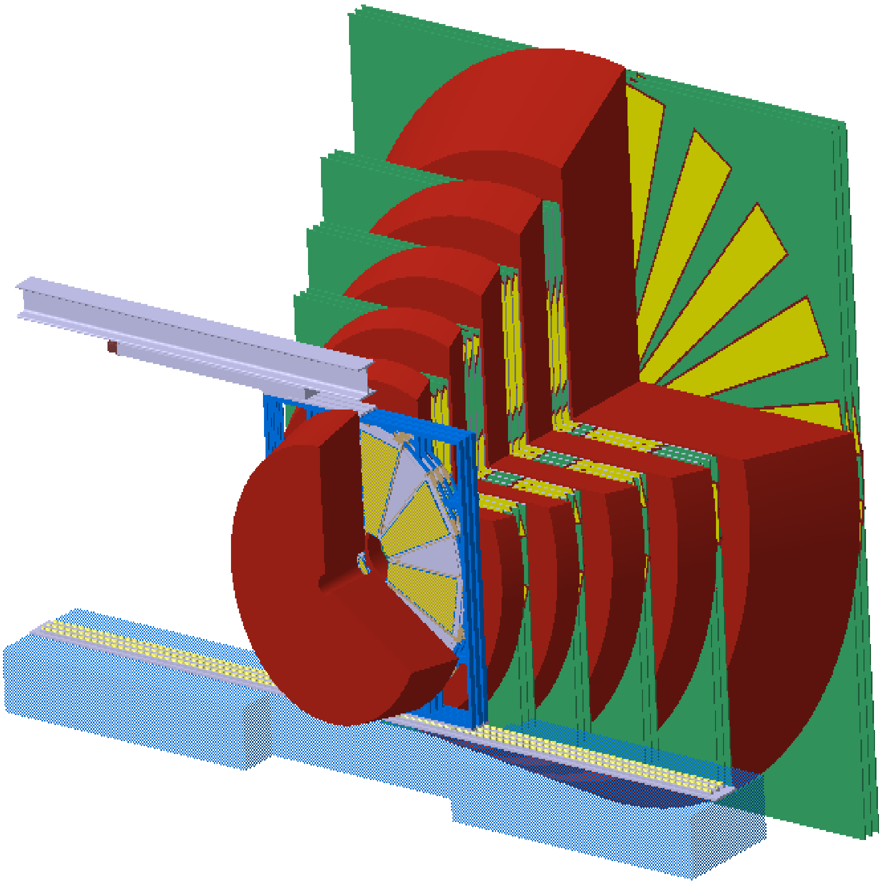

Introduction

Chapter 1

Introduction

1.1 Elementary particles

Until the beginning of the 20^{th} century, atoms were considered to be the fundamental building blocks of matter. However, Rutherford experiment revealed that an atom is made of massive nucleus and electrons and they were regarded as the fundamental particles. In early 1960's, with the advancement in technology, sophisticated devices were developed to accelerate elementary particles to high energies for colliding them to produce new particles [1]. The produced particles included various baryons, mesons and leptons. However, the deep inelastic electron-proton scattering experiments [2] established that baryons and mesons are not fundamental particles and they have sub-structures. A model was postulated in 1964 by Gell-Mann [3] and independently by Zweig [4, 5] dealing with such sub-particles, called quarks. There are six flavours of quarks : up (u), down (d), strange (s), charm (c), bottom (b) and top (t) and their corresponding antiquarks : $\bar{u}$, $\bar{d}$, $\bar{s}$, $\bar{c}$, $\bar{b}$ and $\bar{t}$, grouped into three generations. The properties of the quarks are presented in Table 1.1 [6]. Antiquarks are the antiparticles of the quarks and have the same masses as the quarks, but opposite charges and other quantum numbers. Table 1.2 [7] gives the details of the experiments in which these quarks were discovered. The mesons contain one quark and antiquark ($q\bar{q}$), whereas baryons are made up of three quarks (qqq). These quarks are confined within the hadrons by strong forces.

Table 1.1 Some basic properties of the quarks [6].

Flavour	Symbol	Mass (MeV/c^2)	Q/e	Quantum number
up	u	$2.3^{+0.7}_{-0.5}$	$+\frac{2}{3}$	3^{rd} component of Isospin $I_Z = +\frac{1}{2}$
down	d	$4.8^{+0.7}_{-0.5}$	$-\frac{1}{3}$	3^{rd} component of Isospin $I_Z = -\frac{1}{2}$
strange	s	95 ± 5	$-\frac{1}{3}$	strangeness S= -1
charm	c	1275 ± 25	$+\frac{2}{3}$	charm C = +1
bottom	b	1418 ± 30	$-\frac{1}{3}$	bottom B'= -1
top	t	173210 ± 510 ± 710	$+\frac{2}{3}$	top T = +1

Table 1.2 The details of the experiments which discovered the quarks [7].

Flavour	Symbol	Year	Experiment Location	Reaction
up	u	1968	SLAC	inelastic $e^- - p$ scattering
down	d	1968	SLAC	inelastic $e^- - p$ scattering
strange	s	1968	SLAC	inelastic $e^- - p$ scattering
charm	c	1974	SLAC and AGS at BNL	e^+e^- annihilation, p+Be collisions at 28 GeV
bottom	b	1977	Fermilab	pA collisions at 400 GeV
top	t	1995	CDF and DØ Collaboration, Fermilab	$\bar{p}p$ collisions at $\sqrt{s} = 1.8\ TeV$

1.2 Quantum Chromodynamics (QCD)

The Quantum Chromodynamics (QCD), a non-abelian gauge theory, describes the strong interactions between quarks and gluons and obey SU(3) color symmetry. The quarks come in three colors say, red, blue and green, analogus to electric charge in Quantum Electrodynamics (QED). According to QCD, all combinations of quarks must contain admixtures of these colors so as to produce colorless hadrons. The quarks interact with each other by the exchange of massless quanta, called gluons.

1.2.1 Quark confinement and asymptotic freedom

Quarks are bound inside the hadrons by exchange of gluons by strong forces. In QCD, the potential between two quarks separated by a distance r is given as [8]:

$$V_s(r) = -\frac{4}{3}\frac{\alpha_s}{r} \; + \; kr \tag{1.1}$$

where α_s is the strong coupling constant and k is a spring constant of magnitude $\sim 1 \ GeV/fm$. Second linear term in Eq. 1.1 dominates at larger distances, $r \ > \ 1 \ fm$ and $V(r) \rightarrow \ \infty$ for $r \rightarrow \ \infty$. When two quarks or quark-antiquark pairs separate, the self-coupling of gluons interaction causes the color field lines to be pulled together, forming a tube or a string. The potential at larger distances, therefore, increases linearly with separation of the quarks and the density of field lines remain constant. Hence, the enormous amount of energy is required for their separation. However, if these strings are stretched enough, they become energetically suitable to break and terminate the field lines with the creation of $q\bar{q}$ pairs out of the QCD vacuum. Hence, two quarks can't be separated to very large distances and hence lead to "confinement".

The first term in Eq. 1.1 dominates at shorter distances, $r \ < \ 1 \ fm$, arising from single gluon exchange similar to the Coulomb potential between the elementary charges. At shorter distances, $V(r)$ is governed by the first term, deconfinement is possible if α_s tends to become 0 faster than r. Two phenomena are responsible for the deconfinement of quarks at relatively shorter distances : one is asymptotic freedom, which takes place at high energies, whereas the other which occurs at high hadronic density is Debye screening.

At short distances, the strong coupling constant, $\alpha_s(r)$, has a strong dependence on Q^2 (and also r), where Q is the momentum transfer between

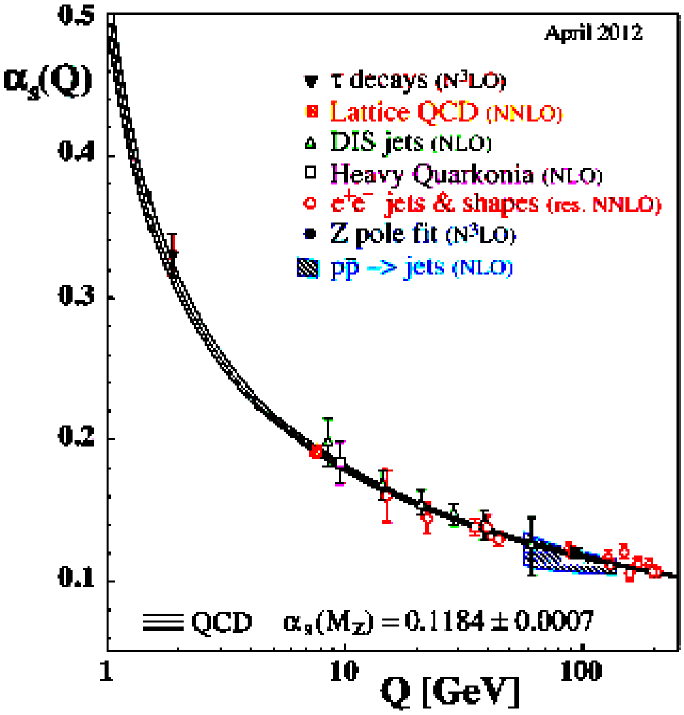

Fig. 1.1 The strong coupling constant, α_s, plotted as a function of Q measured in different experiments and from theoretical calculations. The figure has been take from [9].

interacting quarks. The dependence of the strong coupling constant is expressed as:

$$\alpha_s(Q^2) = -\frac{12\pi}{(33 \; - \; 2n_f)\ln{(Q^2/\Lambda^2_{QCD})}} \tag{1.2}$$

where n_f is the number of quark flavours, Λ_{QCD} is QCD scale parameter. The variation of coupling strength as a function of energy scale is exhibited in Fig. 1.1. For asymptotically large Q^2, $\alpha_s \to 0$, i.e., quarks behave as if free. This phenomenon is known as “asymptotic freedom”, first discovered by Frank Wilczek, David Gross and David Politzer [10, 11].

An alternative consideration, which results in the deconfinement of quarks and gluons is the Debye screening, analogous to the effect of charge screening in QED. In dense matter, the Debye screening radius r_D depends on the number density as

$$r_D \; \sim \; \frac{1}{\sqrt[3]{n_D}} \tag{1.3}$$

Eq. 1.3 implies that with increasing number density, Debye screening radius becomes smaller than the electron binding radius, and the exponential term in Eq. 1.1 tends to zero. Because of the Debye screening, the outermost electrons are freed from their host atom and the material becomes an electrical conductor. In compressed quark matter, compression due to strong forces is expected to produce color conducting system of deconfined quarks and gluons, known as quark-gluon plasma (QGP) [12].

Creation of QGP under extreme conditions of high temperatures and/or baryon densities motivates experimentalists world-wide to perform high-energy heavy-ion collision experiments in the laboratory.

1.2.2 Chiral symmetry

Chiral symmetry predicts that for every particle, there exists a mirror particle of the same mass. Masses of the light quarks are generated by the spontaneous breaking of the chiral symmetry, which is illustrated in Fig. 1.2, where masses of the quarks are displayed in the QCD and Higgs vacua. However, the masses

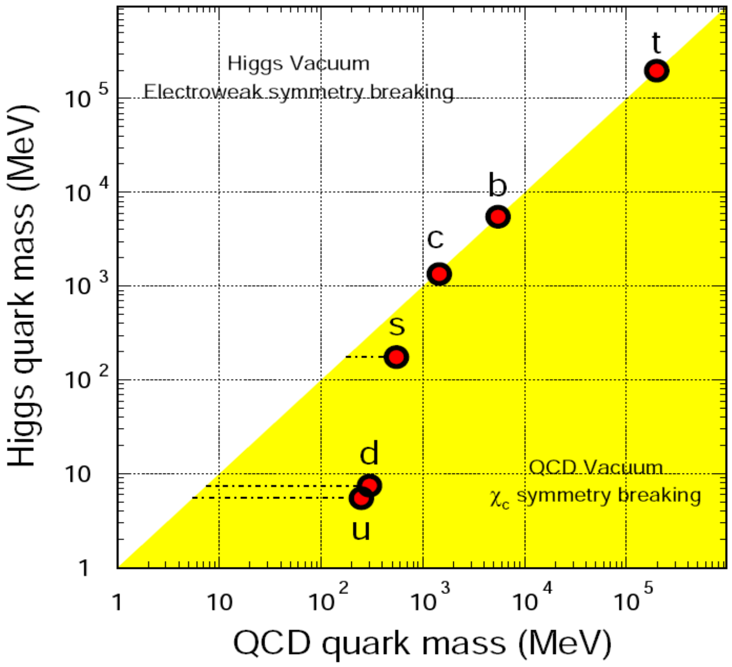

Fig. 1.2 Quark masses in the QCD and Higgs vacua. Large fractions of the light quark masses are created due to the spontaneous breaking of chiral symmetry in the QCD vacuum [13].

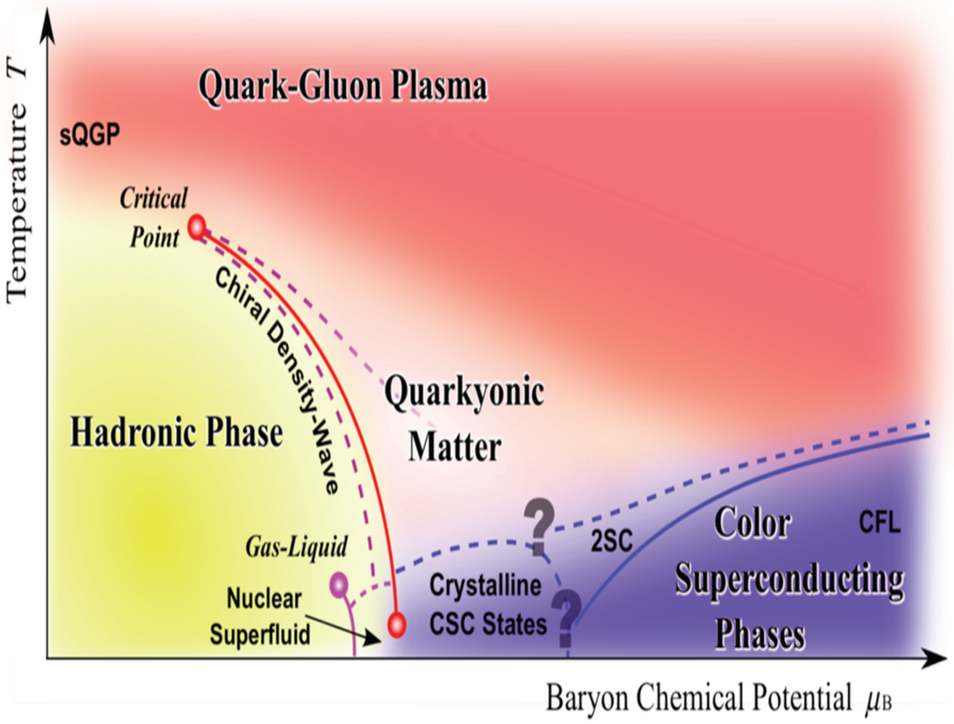

Fig. 1.3 Sketch of the phase diagram of strongly interacting matter plotted as function of the temperature and the net baryon density [14].

of the heavier quarks are not affected by the spontaneous breaking of chiral symmetry. At high temperatures and/or densities, a new state of matter, QGP, is envisaged to be formed, restoring complete chiral symmetry.

1.3 Phase diagram of strongly interacting matter

Huge experimental and theoretical efforts worldwide have been made to explore the phase diagram of strongly interacting nuclear matter. Fig. 1.3 shows the possible states of nuclear matter in the plane of temperature T and baryon chemical potential μ_B [14]. Based on the fundamental property of deconfinement, three different states of matter are discernible : the hadronic matter at low μ_B and T, QGP at high T [15] and the color superconductor at high μ_B and low temperature.

- ***Hadronic matter :*** At zero temperature and $\rho_B = 0.17\ nucleons/fm^3$, matter exists as a liquid and at finite temperature and density, phase transition from liquid to gas occurs. At this temperature matter consists of nucleons only. At moderate temperatures and densities, nucleons are excited to short-lived states, baryonic resonances, and emit mesons in their decays. At higher temperatures, enough energy is available for the creation of baryon-antibaryon pairs. This mixture of baryons, antibaryons and mesons, all strongly interacting particles, is called hadronic matter and is represented by a region of yellow colour in the phase diagram, displayed in Fig. 1.3.

- ***QGP :*** At very high temperatures and/or baryonic densities, hadrons melt into its constituent quarks and gluons, creating a new form of matter, known as Quark-Gluon Plasma, QGP. The deconfined partonic matter can be created either by compressing cold nuclear matter or by heating the matter at nearly zero net baryon density. The heating process increases the temperature of the system, which can be achieved at high energies, whereas compression mode consists of increasing baryon density for a given volume.

  At high temperatures and low net baryon densities, where the number of particles and antiparticles are approximately equal, lattice QCD predicts a smooth phase transition from hadronic to partonic matter, known as crossover [16], taking place at a critical temperature of $T_c \simeq 170\ MeV$ [17] and is displayed by a region of red colour in the phase diagram shown in Fig. 1.3. The QGP state is believed to have existed just before a few microseconds after the Big Bang. A second order phase transition in this region is predicted by lattice QCD.

  In the region of baryonic density beyond $\mu_B \sim T_c$, where the number of particles is relatively more than the number of antiparticles, no reliable information is available from the lattice QCD calculations. Model calculations reveal the existence of QCD critical point [18] at high baryon chemical potential and occurrence of phase transition of first-order from hadronic to deconfined partonic matter and is depicted by a region of pink colour in the phase diagram displayed in Fig. 1.3 . A new phase of so called quarkyonic matter is also envisaged to exist beyond the first-order phase transition at large baryon chemical potentials and moderate temperatures [19]. It may be of interest to mention that high baryon density, but cold nuclear matter is visualized to exist in the core of neutron stars.

- ***Super conductor :*** At asymptotically large baryonic density and low temperature, two quark pairs near the Fermi condensate (Cooper pairs) are predicted to form a color superconductor [20], shown by blue colour region in the phase diagram shown in Fig. 1.3.

The exploration of the phase diagram of strongly interacting matter has also strong implications in cosmology, particularly for astrophysical compact objects. The experimental discovery of the prominent landmarks of the QCD phase diagram is a major breakthrough in our understanding of the properties of nuclear matter. Equally important is quantitative experimental information on the properties of hadrons in dense matter, which may shed light on chiral symmetry restoration and the origin of hadron masses.

Experimentally, one needs to vary temperature and/or the net baryonic density in order to create hot and dense matter, which can be achieved in high-energy heavy-ion collisions in laboratory by varying the collision energy and sizes of the colliding nuclei. High-energy heavy-ion collisions are, therefore, excellent tools to probe the phase diagram of strongly interacting matter.

1.4 Relativistic heavy-ion collisions : to probe the QCD phase diagram

In order to study nuclear matter under extreme conditions of temperatures and/or baryonic densities, it is essential to create hot and dense nuclear matter in laboratory. This can be achieved in the collisions of heavy nuclei, either by bombarding accelerated ions at stationary targets or by the head-on collisions of two ion beams. When relativistic nuclei undergo collisions, dense hadronic matter is envisaged to be produced. In such collisions, an energy density greater than 1 $GeV fm^{-3}$ is attained and corresponding relativistic matter pressure is P $\simeq 1/3\epsilon = 0.52 \times 10^{35}$ *Pascal* [21]. Dense matter with these characteristics must have existed in the early Universe, before a few μs after the big bang. Experimental study of the physics of the early Universe requires, in principle, a large, practically infinite volume of matter. It is, therefore, necessary to study high-energy collisions of the heaviest nuclei such as lead (Pb) and gold (Au) nuclei. Available experimental results reveal that such collisions lead to the formation of dense hadronic fireball, well localized in the space with an energy density of $\epsilon = 1\ GeV fm^{-3}$. Because of high internal pressure, the fireball, with life time characterized by the size of the system, $\tau \simeq 2R/c$, explodes rapidly, where R is the radius of the fireball and c is the speed of light in vacuum. In relativistic heavy-ion collisions, the collision energy is shared among numerous newly produced hadrons. It is, therefore, believed that the deconfined state creates a large number of low-energy hadrons but a few high-energy particles, as happens in hard elementary particle interactions. It is also expected that high baryon densities, as in the core of neutron stars, can be reached in high-energy heavy-ion collisions. This idea forms the basis of performing Compressed Baryonic Matter (CBM) experiment at FAIR. The CBM research program aims to explore the structure of high-density matter, particularly relating to deconfinement and chiral symmetry restoration.

1.4.1 Space-time evolution of a High Energy Heavy-Ion Collision

Space-time evolution of a high energy heavy-ion collision is illustrated in Fig. 1.4 and may be studied in terms of the Bjorken model [22]. In high energy heavy-ion collisions the Lorentz contracted nuclei moving at relativistic velocities are colliding. After the initial collision phase, two scenarios are possible based on the energy density as shown in Fig. 1.4. The left-hand side corresponds to the case where the energy density is not sufficiently high for the formation of QGP, a purely hadronic scenario, while the right-hand side exhibits the expected collision evolution above the threshold energy density for the creation of QGP [22, 23]. In a scenario with QGP formation, time

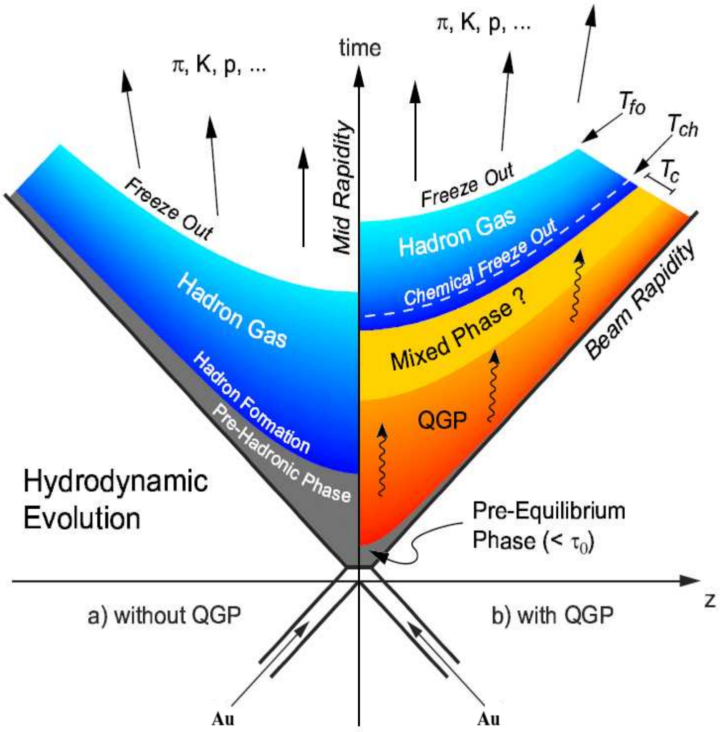

Fig. 1.4 A schematic diagram showing evolution of the fireball produced in a relativistic heavy-ion collision in the light cone picture. The left-hand side shows the evolution in the case of a purely hadronic scenario without QGP formation, while the right-hand side illustrates the expected evolution of the system producing QGP. The different phases based on different times, include the pre-equilibrium partonic phase, thermalized quark-gluon plasma, hadronization and its subsequent freeze-out. [24].

evolution of the fireball proceeds by the following steps :

- ***Initial state and pre-equilibrium :*** The two highly energetic Lorentz-contracted nuclei travel along the light cone for $t < 0$ and collide at the origin ($t = 0$, $z = 0$) with an impact parameter b. Depending upon the impact parameter, two colliding nuclei overlap either partially for $b > 0$ or fully in the case of $b \simeq 0$ and deposit large amounts of their kinetic energies inside a small volume in the centre of the collision zone. The deposited high-energy causes liberation of a large number of partons, quarks and gluons. This phase is termed as a pre-equilibrium phase of $\tau \sim 1\ fm/c$, where τ is the longitudinal proper time $\tau = \sqrt{t^2 - z^2}$.

- ***Thermalization :*** The created partons of high energies rescatter both elastically and inelastically. After adequate interactions for $\tau_0 = 0.5 - 1\ fm/c$, these partons undergo thermal equilibration and QGP is supposedly created. Driven by the pressure gradient, the QGP expands and cools for a duration of $\tau_{QGP} \sim 3 - 5\ fm/c$.

- ***Mixed phase :*** The QGP expands and cools down to a temperature up to T_c, reaching the hadronization stage in which hadrons are formed. Before complete transformation to a hadron gas, a mixed phase comprising of deconfined quarks and hadrons is formed.

- ***Hadronization and Freeze-out :*** Hadronization then follows as the energy density falls below the critical value, $\epsilon_c \sim 1\ GeV/fm^3$ required for plasma formation by crossing the phase boundary. Further expansion occurs in the hadronic stage until the "chemical freeze-out" point when inelastic interaction stops, thereby, fixing the chemical composition of the matter. After that, further expansion/cooling takes place until "kinetic freeze-out" or "thermal freeze-out" is reached. A thermal freeze-out is defined as a point in temperature where the density of particles with elastic cross section, σ, becomes small enough so that the mean free path $\lambda = 1/n\sigma$ is larger than the system size and elastic collisions among them stop. The total fireball lifetime is $\approx 10 - 15\ fm/c$ depending upon the beam energy.

1.4.2 Energy regions of heavy-ion collisions

In laboratory, hot and dense nuclear matter can be created over wide ranges of temperatures and/or densities by colliding nuclei at high energies. In order to understand whether high temperature or high baryonic density is responsible for the creation of the dense nuclear matter, the relativistic heavy-ion collisions can be divided into two separate regions : the stopping and transparent region.

- ***Stopping region***, where baryons coming from the projectile and the target are fully or partly stopped by each other, forming a fairly baryon rich matter in the middle of the reaction zone. The first experimental results available from SPS, CERN and AGS, BNL up to $E_{Lab} \sim 60\ AGeV$, indicate almost complete stopping of ^{32}S and ^{28}Si projectiles in the collisions. Some theoretical estimates indicate that with ^{208}Pb collisions at $\sqrt{s_{NN}} = 200\ GeV$ (RHIC energy) will result in stopping of the baryons in the middle of reaction zone and phase-space [25]. Hence, these reactions are regarded to be the best tools to study the baryon rich matter. This region is also of Astrophysical importance associated with possible hybrid stars such as neutron stars with dense baryonic matter core [26]. The Compressed Baryonic Matter experiment at FAIR, Germany, a fixed-target experiment, will be devoted to the exploration of matter at high baryon density by exploiting the beams of intensities up to $10^9\ ions/s$ supplied by FAIR. Details regarding the FAIR facility will be presented in Chapter 2.

- ***Transparent region***, where initial target and projectile baryons are so far apart in the phase-space that the heavy-ion collisions cannot slow them down completely. For $\sqrt{s_{NN}} > 100\ GeV$, theoretical prediction is that the initial baryons from the projectile and target will not slow down completely. The baryon will keep on moving with their initial velocities and the reaction zone will be essentially baryon free; energy will also be deposited in this region. The large energy density matter in the central region may form a baryon free quark-gluon plasma, which is of immense theoretical interest. Furthermore, high energy density and low baryon density matter are believed to have existed in the early Universe. The heavy-ion accelerators which would achieve this energy regime in the collisions are: Large Hadron Collider at CERN, Relativistic Heavy Ion Collider at BNL and Tevatron at Fermilab [26].

1.4.3 Relativistic heavy-ion experiments

A summary of the past and on going heavy-ion collision experiments is given in Table 1.3. The forthcoming experimental facilities include the dedicated *Fixed-target* experiments at the FAIR, GSI, is expected to be operational in 2018 [27], the NA61 experiment at CERN-SPS, heavy-ion collider project (NICA) at Dubna. Different heavy-ion experiments with different beam energies probe different regions of the QCD phase diagram. It is of interest to note that the matter created in the central region of the collisions with higher beam energies is more symmetric between baryons and antibaryons, while the low energy experiments, such as FAIR, enable to study the properties of dense baryonic matter.

Table 1.3 On going and future experimental facilities for high-energy nuclear collisions alongwith the details regarding the beams and the center-of-mass energies.

Accelerator	Starting Year	Type	Collision System	$\sqrt{s_{NN}}$ GeV/A
AGS@BNL	1986	Fixed-Target	^{28}Si+^{197}Au	5
SPS@CERN	1986	Fixed-Target	^{32}S+^{208}Pb ^{16}O+^{208}Pb	19
AGS@BNL	1992	Fixed-Target	^{197}Au+^{197}Au	5
SPS@CERN	1994	Fixed-Target	^{208}Pb+^{208}Pb	17
RHIC@BNL	2000	Collider	^{197}Au+^{197}Au	200
LHC@CERN	2008	Collider	^{208}Pb+^{208}Pb	5500
SIS100 and SIS300 @FAIR	$\sim$ 2018	Fixed-Traget	^{197}Au+^{197}Au	2.3 - 9.3

1.5 Signatures of QGP formation

It is commonly believed that the QGP, if formed in relativistic heavy-ion collisions, will have transient life time $\sim\ 10^{-23}\ s$ and hence cannot be directly observed. One has, therefore, to look for the particles that escape from the fireball and detect in experiments. These particles provide indirect evidence regarding QGP formation. In this section, the proposed signatures are briefly described.

1.5.1 Direct photon production

Photons, real or virtual (i.e., decaying to lepton pairs e^+e^- and $\mu^+\mu^-$), produced in relativistic heavy-ion collisions are collectively called as electromagnetic probes. Emission of electromagnetic radiation is believed to be one of the most promising and efficient tools to characterize the initial state of heavy-ion collisions. Virtual photons decay into dileptons which carry the memory of the formation of the direct photons. Following are the main processes for direct photon production in the QGP medium :
(a) Annihilation Process : The annihilation process involves production of a gluon and a photon

$$q + \bar{q} \rightarrow \gamma + g \tag{1.4}$$

(b) QCD Compton scattering : This process involves scattering of a gluon off a quark or an antiquark

$$\left.\begin{aligned} g + q &\rightarrow \gamma + q \\ g + \bar{q} &\rightarrow \gamma + \bar{q} \end{aligned}\right\} \tag{1.5}$$

Besides the emission of photons from the quark-gluon plasma, photons can also be emitted from the hadronic processes such as, pion annihilation, interaction of pion with ρ^0 meson and interaction of charged pion with neutral pion. Hard nucleon-nucleon collision as well as the decays of final-state mesons after freeze-out also contribute in the photon production.

As no further interaction of photons takes place with the medium, thus carry the intact information about the interior of the fireball. the photon production rate and photon momentum distribution provide the information on the thermodynamic condition of the medium at the moment of their formation [28].

1.5.2 Dilepton production

In QGP, the quarks and antiquarks annihilate to create virtual photons, γ^*, which decay into lepton pairs (l^+l^-) as shown in Fig. 1.5(a). The system of the produced lepton - antilepton pair is referred to as dilepton or l^+l^- pair. The dilepton (l^+l^-) is characterized by dilepton invariant mass squared $M^2 = (P_l^+ + P_l^-)^2$, where P_l^+ and P_l^- are the four-momenta of the dilepton and dilepton's transverse momentum $p_T = (p_l^+)_T + (p_l^-)_T$, where $(p_l^+)_T$ and $(p_l^-)_T$ are the transverse momenta of the dilepton.

Once these dileptons are created, they must pass through the collision region to particle detectors. They interact electromagnetically and have large mean free paths. The produced lepton pairs, therefore, do not suffer further collisions before reaching the detectors and thus carry the unscathed information about the interiors of the fireball [28].

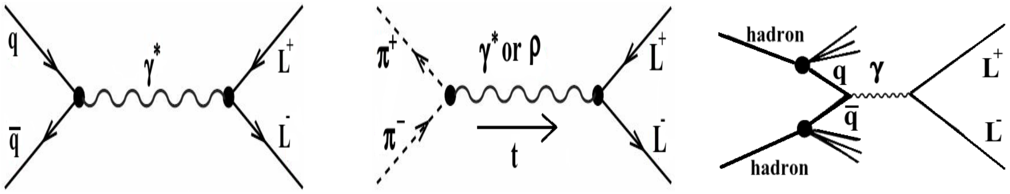

(a) *(b)* *(c)*

Fig. 1.5 Various reaction mechanisms for the creation of lepton pairs : (a) reaction $q\bar{q} \rightarrow l^+l^-$ in the QGP medium. Fig. (b) and (c) show Drell-Yan process and hadron decay modes for the creation of a lepton pair, which contribute to background [28].

The lepton pair production can also take place via Drell- Yan process, decays of hadron resonances and charmonia and $\pi^+\pi^-$ annihilation.

1.5.3 Heavy quarkonia suppression

Bound states of heavy quarks and corresponding antiquarks are collectively called quarkonia. During the pre-equilibrium phase, the hard scattering among partons lead to production of heavy quarks and antiquarks, which later bind into J/Ψ $(c\bar{c})$ and Υ $(b\bar{b})$ having masses 3.1 and 9.4 GeV/c^2 respectively. The suppression of these quarkonia are considered as one of the most important probes for investigating the occurrence of phase transition from hadronic medium to QGP.

According to Matsui and Satz [29], J/Ψ and Υ productions are sensitive to the nature of the created medium. In the partonic medium at a certain temperature $T > T_c$, where T_c is the critical deconfinement temperature, quarkonia states would melt through color screening. Their suppression in heavy-ion collisions would indicate towards formation of the QGP. If QGP is formed, the interaction potential would be screened beyond a certain distance called, Debye screening radius, λ_D, due to the presence of quarks, antiquarks and gluons in the plasma. The Debye screening radius, λ_D, represents the range up to which the interaction between quarks and antiquraks are effective. The interactions between quarks and antiquarks get weakened exponentially beyond this separation distance. When the resonance dimensions become larger than λ_D, dissociation of quark and antiquark pairs start taking place. It may be interesting to note that λ_D is inversely proportional to the temperature as reflected in Fig. 1.6.

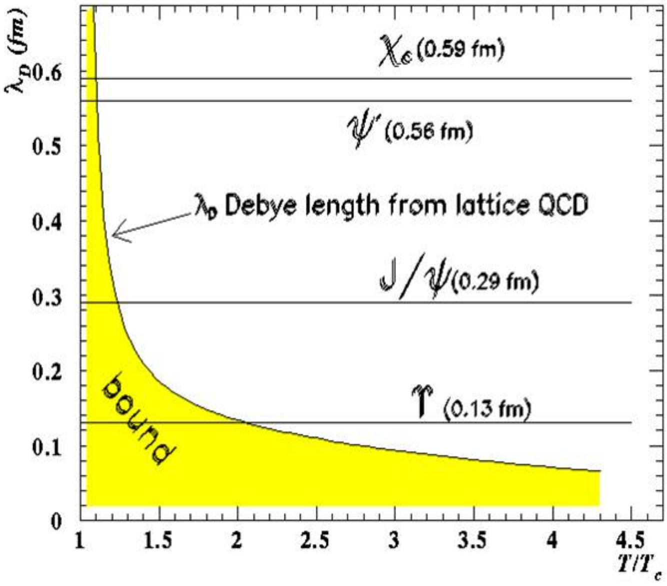

Fig. 1.6 Debye radius as a function of T/T_c. The lines correspond to the critical Debye radius for different quarkonia states.

1.5.4 Strangeness enhancement

In 1982 Rafelski and M$\ddot{u}$ller [30] proposed strangeness enhancement as one of the signals of the QGP formation. Since, valence strange quark are not present in the nucleons of the colliding nuclei, therefore, strangeness provides information about the reaction dynamics in partonic or hadronic phase. In a thermally and chemically equilibrated QGP medium, the energy levels for '*u*' and '*d*' quarks are almost filled up to the Fermi's level. According to Pauli exclusion principle, creation of additional $u\bar{u}$ or $u\bar{d}$ pair in the system would require $2\epsilon_F$ energy, where ϵ_F represents Fermi energy of the light quarks. However, due to chiral symmetry restoration, creation of $s\bar{s}$ is easier with the maximum threshold energy for their production being $\sim\ 2m_s\ \sim$ 300 MeV.

For purely hot hadronic medium, production probability of strange particles is suppressed due to its being more massive in comparison to the particles containing u or d quarks. The dominant channels for strange hadron production are : $N\ +\ N\ \rightarrow\ N\ +\ \Lambda\ +\ K$ and $\pi\ +\ \pi\ \rightarrow\ K\ +\ \bar{K}$ having Q values $\sim$ 670 and 700 MeV respectively, which are much higher than $s\bar{s}$ production threshold.

In the QGP medium, production of strange quarks and their antiparticles predominantly occur through two processes :

a) Collision of light quarks and antiquarks

$$q\ +\ \bar{q}\ \rightarrow\ X\ +\ \bar{X} \tag{1.6}$$

where q represents light quarks, u and d, while X represents a moderate or heavy quark, c or s;

b) Fusion of two gluons

$$g\ +\ \bar{g}\ \rightarrow\ X\ +\ \bar{X} \tag{1.7}$$

Mass of deconfined s and $\bar{s}$ quarks are predicted to be around 350 MeV/c^2, less than the mass when s, $\bar{s}$ are confined within the hadrons due to partial restoration of the chiral symmetry. Its bare mass is around 100 MeV/c^2.

Hence, strangeness production should be enhanced in the deconfined medium as the mass goes down to a value comparable with T_c, $\sim 170\ MeV$. Eventually, the plasma cools down, hadronizes, leading, therefore, to an increase in the number of strange hadrons. Such enhancements should be comparatively more in the case of multi-strange hadrons.

1.5.5 Jet quenching

Jet production in hadronic collisions is a standard hard QCD process. An elastic ($1 + 2 \rightarrow 1 + 2$) or inelastic ($1 + 2 \rightarrow 1 + 2 + X$) scattering of two partons from each of the colliding hadrons results in the production of two or more partons in the final state. The two outgoing partons have a large virtuality Q, which they reduce by subsequently radiating gluons and/or splitting into quark-antiquark pairs. Such a parton branching evolution is governed by the QCD radiation probabilities given by Dokshitzer-Gribov-Lipatov-Altarelli-Parisi (DGLAP) equations [31] down to virtualities 1 GeV^2. In such a scenario, the produced partons fragment non-perturbatively into a set of final-state hadrons. When the jets propagate through the hot and dense medium produced in the relativistic nuclear collisions, due to multiple scattering they suffer further interactions with the medium and suffer loss of energy. The resulting attenuation or disappearance of the spray of hadrons coming out from the fragmentation of a hard parton due to energy loss in the dense medium is called “jet quenching”. It was one of the first proposed “smoking gun” signatures of QGP formation in relativistic heavy-ion collisions. Jets lose their energies via both radiative and collisional process. The energy loss is proportional to both initial gluon density and lifetime of the dense matter.

1.5.6 Flow

Anisotropic flow is an important observable, being sensitive to the effective degrees of freedom in relativistic heavy-ion collisions. It provides information about the Equation-Of-State (EOS) and collective properties and confirms early thermalization in the hot and dense fireball created in a collision. In non-central heavy-ion collisions, initial spatial anisotropy of the nuclear overlap zone is converted into momentum space anisotropy of particle distribution via the operation of azimuthally anisotropic pressure gradient. This leads to an anisotropic azimuthal distribution, $dN/d\phi$, of particles emitted from the collision zone. Anisotropic particle distributions were first suggested [32] as a signal of collective flow in ultra-relativistic heavy-ion collisions. The azimuthal distribution of particle emission is analyzed with respect to the reaction plane in terms of the following Fourier expansion [33] :

$$\begin{aligned} E\frac{d^3N}{d^3p} &= E\frac{d^3N}{dp_T^2dyd\phi} = \frac{1}{2\pi}\frac{d^2N}{p_Tdp_Tdy}(1+2\sum_{n=1}^{\infty}v_n\cos[n(\phi-\Psi_R)]) \\ &= \frac{1}{2\pi}\frac{d^2N(b)}{p_Tdp_Tdy}(1+2v_1\cos(\phi-\Psi_R)+2v_2\cos(\phi-\Psi_R)+...) \end{aligned} \tag{1.8}$$

where v_n are referred to as Fourier or flow coefficients, which depends on N$_{part}$, ϕ is the azimuthal angle of the particle and Ψ is the azimuthal angle of the reaction plane in the laboratory frame.

The first two coefficients in the Fourier expansion, are known as the directed and elliptic flows. The $v_1 = <\cos\phi>$ corresponds to the strength of the directed flow, whereas $v_2 = <\cos 2\phi>$ quantifies the strength of the elliptic flow. The magnitude of v_2 is sensitive to the initial conditions and EOS of the hot and dense fireball. The higher order flow harmonics, such as v_3, v_4, v_5, etc., are sensitive parameters for studying initial state fluctuations and to obtain η/S ratio, where η is shear viscosity over entropy density (S) [34, 35] of the fluid produced in a collision.

1.5.7 Fluctuations

Lattice calculations are associated with divergence of susceptibilities in the proximity of the QCD critical point and hence lead to fluctuations in various observables. The fluctuations of these observables act as one of the key probes of the deconfinement phase transition. Large fluctuations of energy density or temperature is expected if the phase transition is of the first-order. However, second-order phase transition leads to specific heat divergence and reduces the fluctuations drastically if the matter freezes out at the critical temperature. Fluctuations of the conserved quantities like electric charge, baryon number or strangeness are predicted to be significantly reduced in QGP scenario as they are generated in the early stage of the plasma, created in high-energy heavy-ion collisions with quark and gluon as degrees of freedom [36, 37]. The fluctuations generated at the QGP stage will increase as the system evolves in time [38, 39].

The fluctuations not only depend on the type and order of the phase transition but also on the speed by which collision zone goes through the transition, the degree of equilibration, the subsequent hadronization process, the amount of rescattering of hadrons during hadronization and freeze-out [40]. Fluctuations studied in heavy-ion collision experiments are : ratios of charged particles [41, 42], baryon number multiplicity [43], net charge [44], mean p_T [45, 46], etc.

1.5.8 Experimental results at low μ_B as an evidence of QGP formation

First results on the deconfinement phase transition in heavy-ion collisions was reported by the experiments performed at SPS, CERN. At the top SPS energy, $\sqrt{s_{NN}} = 17\ GeV$ for Pb+Pb collisions, the chemical potential, μ_B, is $\approx 250\ MeV$, and freeze-out temperature is about 170 MeV as exhibited in Fig. 1.7. It compares fairly well with the critical temperature predicted by the lattice QCD calculations [47]. The SPS experiments measured several important signatures of the phase tranisition. The following main observables were measured by these experiments : strangeness enhancement, charmonia suppression and initial energy densities, which compare reasonably well with the predicted values for the formation of QGP. One of the important experimental results at SPS energies was the observation of anomalous suppression

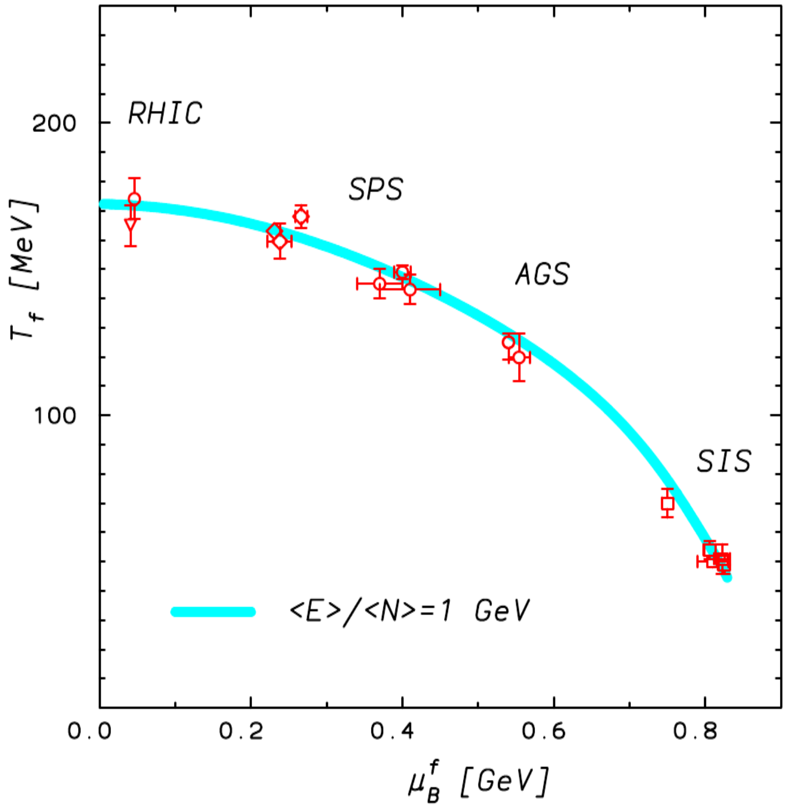

Fig. 1.7 Experimental parameters of the chemical freeze-out points for A+A collisions, derived from a statistical model analysis of the data ranging from SIS to RHIC energies. The curve corresponds to a phenomenological condition of a chemical freeze-out at fixed energy/hadron $\simeq$ 1 GeV in the hadronic gas model [48].

of J/Ψ by NA50 experiment in the central Pb+Pb collisions at $E_{Lab} = 158$ $AGeV$ [49]. The ratio of the cross sections for J/Ψ production and Drell-Yan process as a function of path length is plotted in Fig. 1.8. The main conclusion drawn from the figure is that the normal absorption of J/Ψ, the ratio ~ 1 in p+A collisions, while an anomalous suppression of J/Ψ is seen in central Pb+Pb collisions which corresponds to larger average path length. Recent results from NA60 experiment confirm this observation in In+In collisions at 158 $AGeV$ incident energy [51].

It is worth mentioning that the interpretation of the observed J/Ψ anomalous suppression as a signature of the QGP formation is not very well settled yet. Indeed, other conventional mechanisms based on J/Ψ absorption by comoving

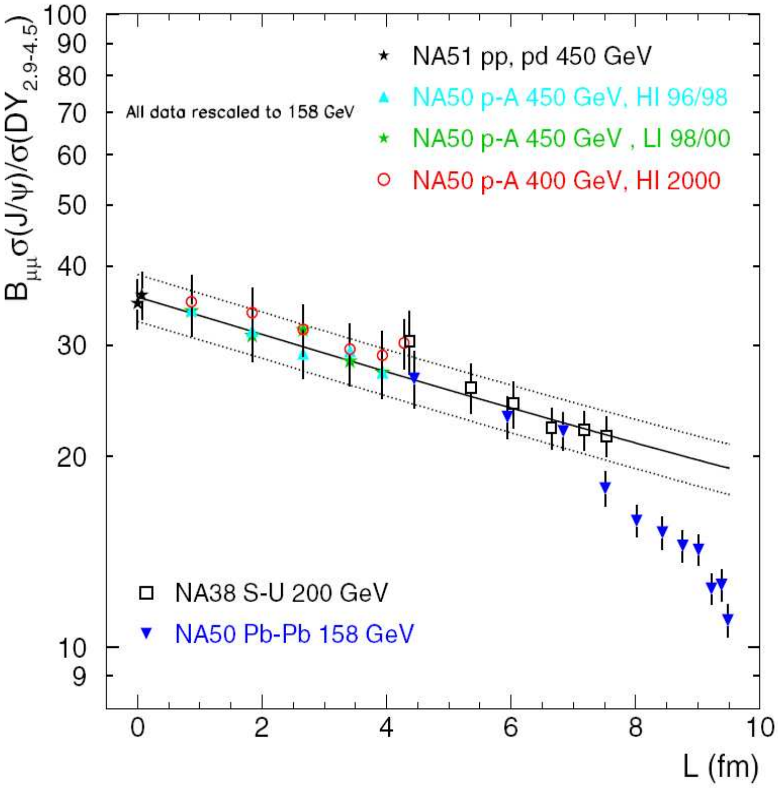

Fig. 1.8 The ratio of the cross sections for J/Ψ and the Drell-Yan process as a function of average path length in nuclear matter [50]. $B_{\mu\mu}$ is the branching ratio of the J/Ψ for dimuonic decay channel, $J/\Psi \rightarrow \mu^+ \mu^-$.

hadrons, term comovers are described as particles having rapidity variables close to the rapidity variables of J/Ψ, might also contribute significantly to the observed effect if the J/Ψ absorption cross sections are of the order of a few millibarns [52, 53].

In 2005, RHIC announced the discovery of deconfined state of matter referred to as strongly interacting QGP, sQGP [54–56]. This result is very important as it differs significantly from the theoretical predictions of QGP as an “ideal gas” and the deconfined matter at RHIC is believed to behave like a “perfect liquid”.

One of the key signatures attributed to the existence of QGP at RHIC energies is the jet quenching. This is illustrated in Fig. 1.9, which shows azimuthal angular correlations between a high-p_T leading hadron and other particles from the same event, measured in Au+Au, d+Au and p+p collisions at RHIC energies. These results indicate strong suppression of one of the jets in head-on Au+Au collisions, while a similar analysis for p+p and d+Au collisions did not show such effect. In order to understand the effect of jet quenching and the conclusions drawn, a brief explanation is given. Jets originate from the scattering of high energy parton pairs, which create showers of quarks and gluons along their trajectories. If a pair of jets is formed in the outer layer of the fireball, then one jet scatters through almost the entire medium while the other one remains in the fireball. The result is that one jet suffers much energy loss than the other, leading thus to a phenomenon called jet suppression. Hence, the jet suppression might reflect the slowing down, or quenching, of the partons as they propagate through the formed medium, quark-gluon plasma. The observation of larger elliptic flow, which is consistent with hydrodynamical

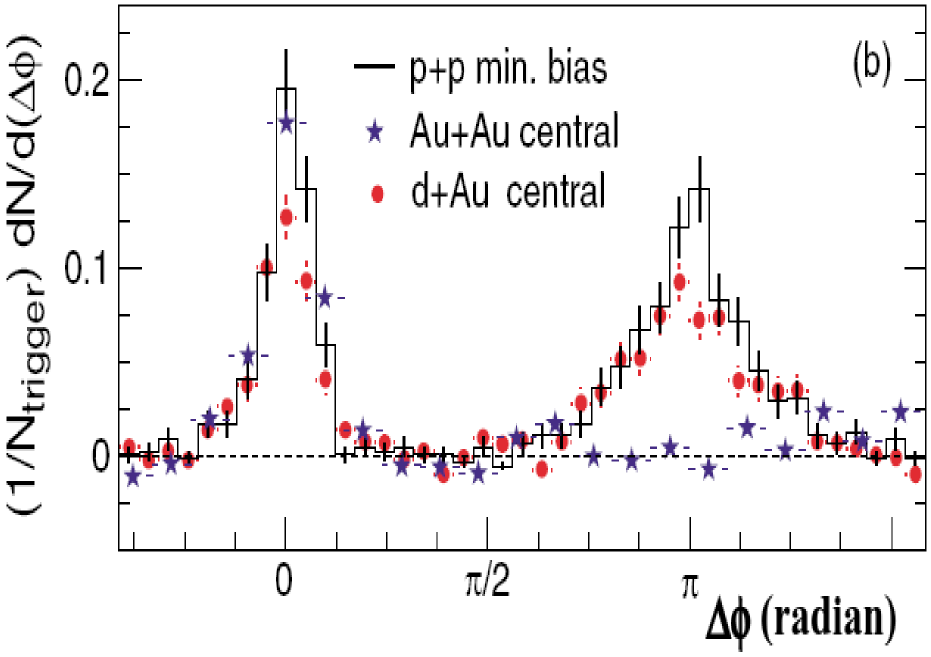

Fig. 1.9 Azimuthal angular correlations between a high-p_T *leading hadron and other particles from the same event, measured in central Au+Au collisions, central d+Au and p+p collisions at* $\sqrt{s_{NN}} = 200$ *GeV [57].* $N_{trigger}$ *is the number of high-*p_T *particles.*

calculations [58] and the existence of a universal scaling of the elliptic flow with the number of valence quarks [59, 60] demonstrate the exsitence of partonic degrees of freedom in the created medium in the collisions at RHIC energies.

1.5.9 Experimental results on high μ_B as an evidence of QGP formation

Transport model calculations perdict that net baryon densities $\sim$ 2 - 12 times the normal baryon density can be achieved in heavy-ion collisions at E_{Lab} = 2 - 40 $AGeV$. Till date, contrary to the high temperature regime, high net baryon density region of the phase transition has been scarcely investigated. NA49 experiment at SPS has measured Pb+Pb collisions in the energy range that corresponds to roughly $\sqrt{s_{NN}} \simeq$ 5 - 10 GeV. Results of NA49 Collaboration show that particle multiplicities globally increase with collision energy . Interesting structures such as “horn” or “kink” has been seen in particle ratios, kinetic properties and particle correlations [61]. These structures strongly indicate the existence of partonic phase attained in the collisions of heavy-ion nuclei at $\approx$ 30 $AGeV$ or $\sqrt{s_{NN}} = 7.6$ GeV as shown in Fig. 1.10. The figure exhibits a prominent peak at $\sqrt{s_{NN}} \simeq$ 7 - 8 GeV, which is absent in p+p collisions in which hot or dense medium is not created. These results cannot be explained by equilibrium hadron gas models [62, 63] and microscopic transport calculations [64]. NA49 Collaboration interprets these results as an evidence for the onset of deconfinement.

Fig. 1.11 illustrates saturation of the chemical freeze-out temperature at $T \sim 160$ MeV above $\sqrt{s_{NN}} \approx 8$ GeV [66] and decrease of baryon chemical potential μ_b. It is observed from the figure that temperature gets saturated at higher energies, whereas μ_b sharply decreases up to RHIC energies, which is one of the characteristics of phase transition. Once the phase transition boundary is reached, the additional energy goes into melting the hadrons and thus leading

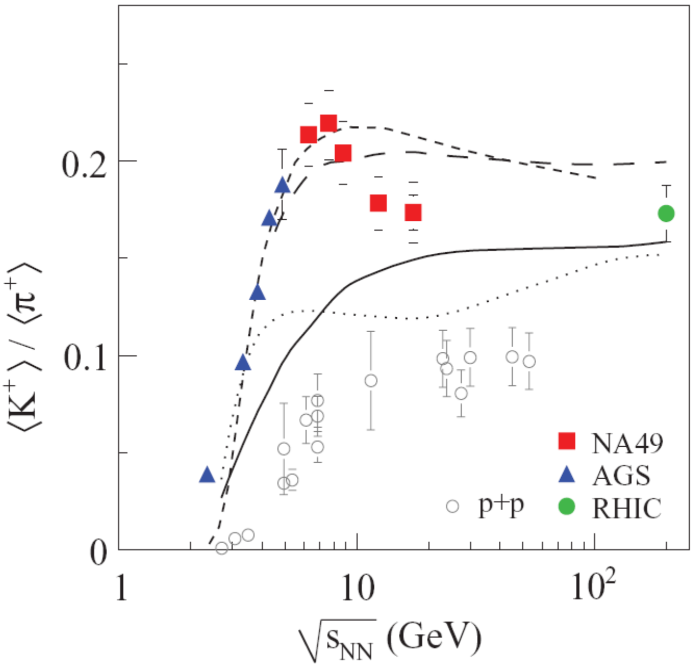

Fig. 1.10 Energy dependence of the K^+/π^+ *ratio which show a "horn" like structure at* $\sqrt{s_{NN}}$ *= 7.6 GeV [61].*

to the formation of QGP. In order to address certain fundamental issues, such as existence of critical end point, collision energy required for the onset of deconfinement, etc., several future experimental programs have been proposed, which include BES (Beam Energy Scan) at RHIC, NA61/SHIINE at SPS, MPD at NICA and CBM at FAIR. Details regarding these programs shall be presented in Chapter3. All these experiments will be able to investigate bulk observables in more details than what have been done so far. Study of rare probes such as dileptons and charm production will only become possible at FAIR, where measurements at very high interaction rates is a certainty.

1.6 Motivation & organisation of the Thesis

One of the prime aims of the relativistic heavy-ion collision experiments is to investigate the QCD phase diagram of strongly interacting matter and to identify signatures of QGP formation. The CBM experiment at FAIR is designed to explore the phase diagram of nuclear matter in the ranges of

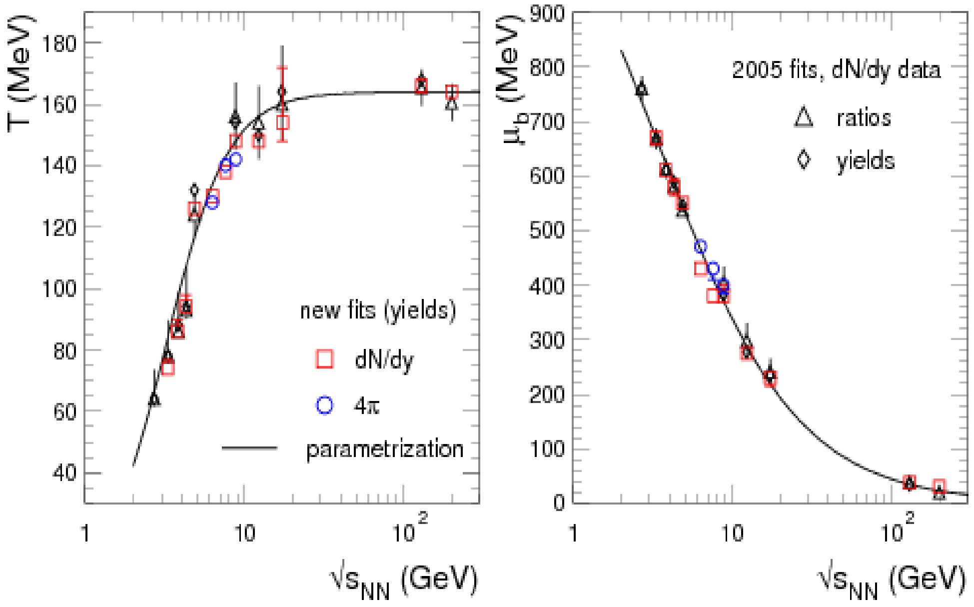

Fig. 1.11 Energy dependence of temperature and baryon chemical potential at chemical freeze-out. The curves are the parametrizations for T *and* μ_b *[65].*

moderate temperatures and extremely high net baryon densities. In-medium modifications of LMVM and J/Ψ suppressions are promising diagnostic probes as indicators to the occurrence of deconfinement phase transition in highly dense nuclear matter. Thus, the planned CBM experimental physics program includes measurement of LMVM and charmonia via their decays into dileptonic channels. As these particles have low production cross sections in the CBM energy range, E_{Lab} = 2 - 40 $AGeV$, their measurements are rather very difficult. This in turn requires accelerators with unprecedented heavy-ion beams of high intensities and detectors with extremely large detection rate-capabilities.

Indian and Russian groups involved in the CBM Collaboration jointly are responsible for designing and building muon detection system for the CBM experiment, which will be dedicated to measure entire dimuon spectrum. The main objective of the work is related to the optimization of the muon detection system for dimuon measurement in the FAIR energy regime.

The main work presented in the thesis may be divided into the following parts : (a) first part is devoted to the optimization of the muon detection system by performing simulation and investigating the feasibility of detection of LMVM by using optimized muon detector in Au+Au collisions at CBM energies and (b) the second part of the thesis is dedicated to the study of multi-strange hadron production in the FAIR energy range. This study is based on simulations carried out by using various event generators for the central Au+Au collisions. The thesis is oragnized in the following manner:

Chapter 1 gives an introduction to the high-energy heavy-ion physics. It begins with the presentation of general characteristics of quarks and interactions between them. A brief description of the phase diagram of strongly interacting matter is also presented. The details of experiments done in the past and ongoing heavy-ion experiments are given. Finally, details of the CBM experiments to be performed at FAIR are presented.

Chapter 2 starts with a brief introduction to the FAIR accelerator facility. The outline of the CBM experiment at FAIR along with the major physics goals and the corresponding observables of CBM experiment are briefly discussed.

Chapter 3 briefly gives a general introduction to the CBM experiment. The experimental challenges in measuring LMVM and charmonia constrain the requirement of detector systems of large acceptance and can handle high interaction rates. The detector can also measure bulk hadrons, multi-strange hyperons, hypernuclei with high accuracy and huge statistics, despite their low multiplitices. The proposed sub-detectors of this experiment are discussed in detail, which include Silicon tracking System, Micro-Vertex Detector, Time-of-Flight detector, Ring Imaging Cherenkov detector, Transition Radiation Detector, Muon Chamber, Electromagnetic Calorimeter and Projectile Spectator Detector.

Chapter 4 describes optimization of detector set-up used for muon identification. One of the important aspects of the CBM experiment is to measure muons created by the decays of LMVM (ω^0, ρ^0, ϕ^0, etc.) or charmonia (J/Ψ, Ψ'). Thus, MuCh is needed for their detection. The number, material and thickness of the absorber is optimized by simulating particles produced in Au+Au collisions at 25 $AGeV$. The simulation procedure for optimization of the MuCh parameters is also described in this chapter.

Chapter 5 desribes the feasibility studies of the optimized SIS100 set-up of MuCh for 8 $AGeV$ central Au+Au collisions. The MuCh system consists of 4 segmented absorber and 4 triplets of tracking chambers placed between two absorbers. The first few tracking chambers, where the particle rates are expected to reach $\sim 1MHz/cm^2$, is based on Gas Electron Multiplier (GEM) detection technique. One of the experimental challenges encountered in MuCh is the extraction of muon tracks from the environment of high multiplicity of charged particles. To account for a realistic signal generation, the readout planes of the modules are segmented into smaller 2-dimensional detection units called pads. The segmentation optimization is, thus, discussed in detail. The optimized pad dimensions based on efficiency, signal to background ratio, occupancy and hit density are also discussed in this chapter.

Chapter 6 deals with the study of multi-strange particle production at FAIR energies in terms of various transport models. The main motivation of this study is to search for the enhanced yields and particle ratios in FAIR energy range and beyond, up to 90 $AGeV$, which is one of the various signatures of deconfinement phase transition. The model results are also superposed with the available experimental data at AGS and SPS energies.

Chapter 7 gives summary and conclusions arrived at on the basis of the results of the present study and provides some invaluable insights in this area for future research programmes.

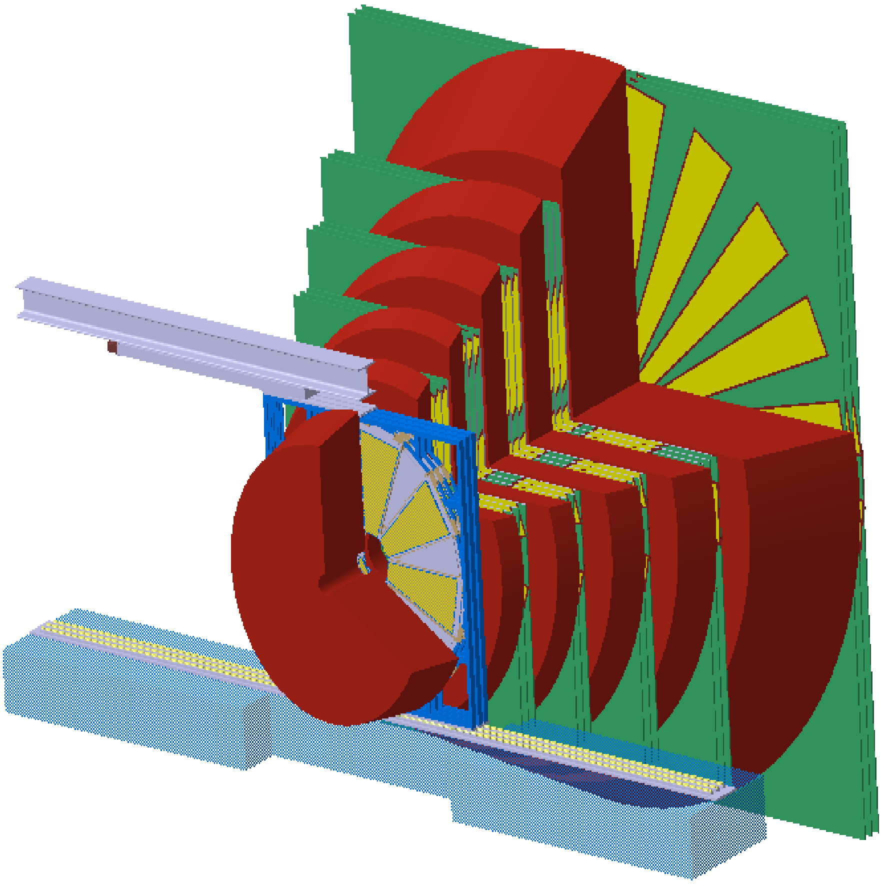

Accelerator Facilities and Research Programs at FAIR

Chapter 2

Accelerator Facilities and Research Programs at FAIR

The Facility of Antiproton and Ion Research (FAIR) is an accelerator facility which has been jointly developed by an international science community and GSI laboratory at Darmstadt, Germany. The main aim of FAIR is to provide beams of stable and unstable nuclei as well as antiprotons of wide ranges of intensities and energies having excellent beam qualities for various scientific programs [67]. Fig. 2.1 shows a sketch of future FAIR along with the existing GSI facilities. The FAIR shall utilize two synchrotrons, SIS100 and SIS300, having a circumference of 1.1 Km with rigidities of 100 and 300 Tm respectively. The existing GSI accelerators, UNILAC and SIS18, serve as injector for the new synchrotrons. SIS100 synchrotron is used to accelerate ions and protons at high repetition rates and either send them to targets for Radioactive Ion Beam (RIB) or Antiproton Beam production or SIS300 for further acceleration to higher energies. Additionally, FAIR comprises of Superconducting Fragment Separator (Super-FRS), storage ring for antiprotons (High-energy Storage Ring HESR), Collector Ring (CR) and New Experimental Storage Ring (NESR). The CR/Recycled Experimental Storage Ring (RESR) complex is used for cooling secondary beams and storage of antiproton beams. On the other hand, HESR and NESR are the experimental storage rings for antiprotons and ions respectively [68]. The FAIR facility is designed to provide beams of energies, at least 20 times higher than those attainable so far by GSI accelerator. It will

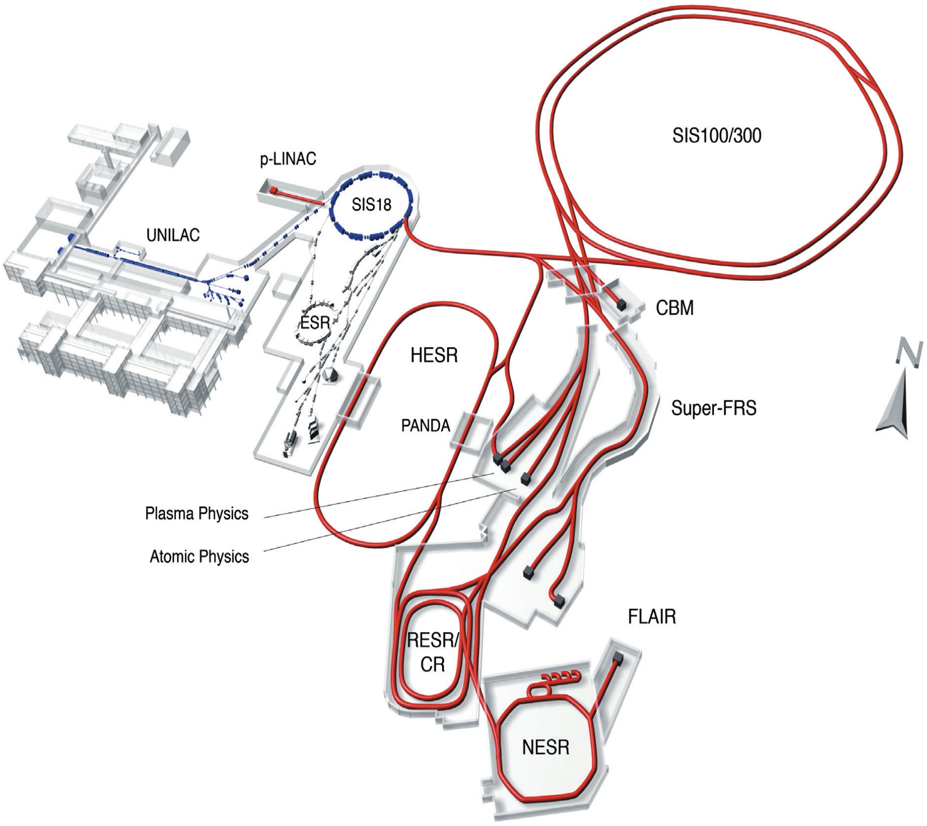

Fig. 2.1 Layout of the existing GSI facility (UNILAC, SIS18, ESR) on the left (blue) and the planned FAIR facility on the right (red): the superconducting synchrotrons SIS100 and SIS300.

also supply beams of rare isotopes and antiprotons with unparalleled qualities and intensities.

Due to the intrinsic cycle times of the accelerators and the storage-cooler rings, multidisciplinary research programs can run in parallel mode. These research programs are : (1) antiProton ANnihilation at DArmstadt (PANDA) detector for hadron physics experiments using cooled high-energy antiproton beams provided by HESR, (2) the NUclear STucture and Astrophysics and Reactions (NUSTAR) detectors used for experiments on the structure of unstable nuclei and nuclear astrophysics, (3) atomic, plasma physics and application (APPA) and (4) the Compressed Baryonic Matter (CBM) experiment for investigating nucleus-nucleus collisions in baryonic rich medium.

Beams emerging from SIS100 and SIS300 synchrotrons will be delivered to HADES and CBM. The available kinetic beam energy per nucleon depends essentially on bending power, B.r, of the dipole magnets :

$$E/A = \sqrt{(0.3 \times B \times r \times Z/A)^2 \ + \ m^2} - m \tag{2.1}$$

where Z and A represent respectively atomic and mass numbers of the ion and m is the mass of a nucleon. The beam energies acquired from the beam rigidities of SIS100 and SIS300 are tabulated in Table 2.1, having the minimum available ion beam energy of about 2 $AGeV$ [69].

Table 2.1 Ion species and their kinetic energies per nucleon (E/A in GeV) for beam rigidities of 100 Tm for SIS100 and 300 Tm for SIS300 [69].

Beam	Z	A	E/A **SIS100**	E/A **SIS300**
p	1	1	29	89
d	1	2	14	44
Ca	20	40	14	44
Ni	28	58	13.6	42
In	49	115	11.9	37
Au	79	197	11	35
U	92	238	10.7	34

2.1 Accelerator facilities at FAIR

The main part of the FAIR accelerator facility is a synchrotron complex comprising of two dedicated synchrotron accelerator rings SIS100 and SIS300, which will be installed in the same tunnel. Their magnetic lattices consist of new rapidly cycling superconducting magnet structures for reducing the cost.

2.1.1 SIS100 synchrotron

The synchrotron SIS100 is designed for a magnetic rigidity of B.r = 100 Tm. It consists of superferric magnets similar to magnets developed for NUCLOTRON synchrotron at JINR, Dubna [70]. The main objective of SIS100 is to achieve intense pulsed (5×10^{11} $ionsperpulse$) Uranium beams at 1 GeV/A and intense pulsed (4×10^{13} $ionsperpulse$) proton beam of 29 GeV. Table 2.2 shows the details of the expected final SIS100 beam intensities.

Table 2.2 Beam parameters of FAIR for SIS100 [71].

Ion species	**Beam Energy** $[GeV/A]$	**Intensity** $[s^{-1}]$
p	29	2×10^{13}
$\mathbf{U}^{28+}$	1.5	4×10^{11}
$\mathbf{U}^{92+}$	11	1×10^{10}

Since for synchrotron acceleration, the incoherent space charge limits scales by a factor of A/q^2 for ion species of mass number A and charge q, intermediate charged state ions are used for acceleration of high intensity beams, e.g, U^{28+} - ions up to 2.7 GeV/A and protons of up to 30 GeV. Both the heavy-ion and proton beams are compressed down to very short bunch length, which are required for the production, storage and efficient cooling of exotic nuclei and anti-protons [67, 72].

2.1.2 SIS300 synchrotron

The SIS300 (B.r = 300 Tm) is implemented with low-loss, cos(θ)-type magnets providing ramp rates of up to 1 T/s. SIS300 will work in two different modes : (1) stretcher mode and (2) high energy mode. In the stretcher mode SIS300 will continuously supply slow extracted beams of high intensity in the energy range from 1.5 GeV/A to the maximum energy of SIS100. It operates in intermediate charged states heavy-ion beams for achieving the highest possible number of particles per second. It is, therefore, planned to provide slowly extracted U^{28+} beams with an intensity of 10^{12} $ions/s$ at energies 0.4 - 1.5 GeV/A for the production of radioactive beams for experiments with fixed-targets behind the Super-FRS. These high intensity beams are extracted over a period of 10 - 100 seconds in quasi-continuous mode. On the other hand, in higher energy mode, SIS100 injects fully stripped heavy-ion beams to SIS300 [72, 73]. The main parameters of SIS300 beams are listed in Table 2.3

Table 2.3 Main beam parameters of FAIR for the full version SIS300 [74].

Ion species	Beam Energy (GeV/A)	Intensity (s^{-1})
p	90	3×10^{13}
U^{28+}	1.5	10^{12}
U^{92+}	up to 35	10^{10}
RIBs	up to 1.5 - 2	$< 10^{9}$
Stored and cooled antiprotons	1.5 - 15	10^{11}

The full version of the accelerator facility, including SIS300 will deliver beams of heavy-ions of up to 11 (SIS100) and 35 $AGeV$ (SIS300), light-ion beams of up to 14 (SIS100) and 45 $AGeV$ (SIS300) and proton beams of up to 29 (SIS100) and 89 GeV (SIS300), and these heavy-ion beams are ideal for the CBM core research program.

2.2 The CBM experiment

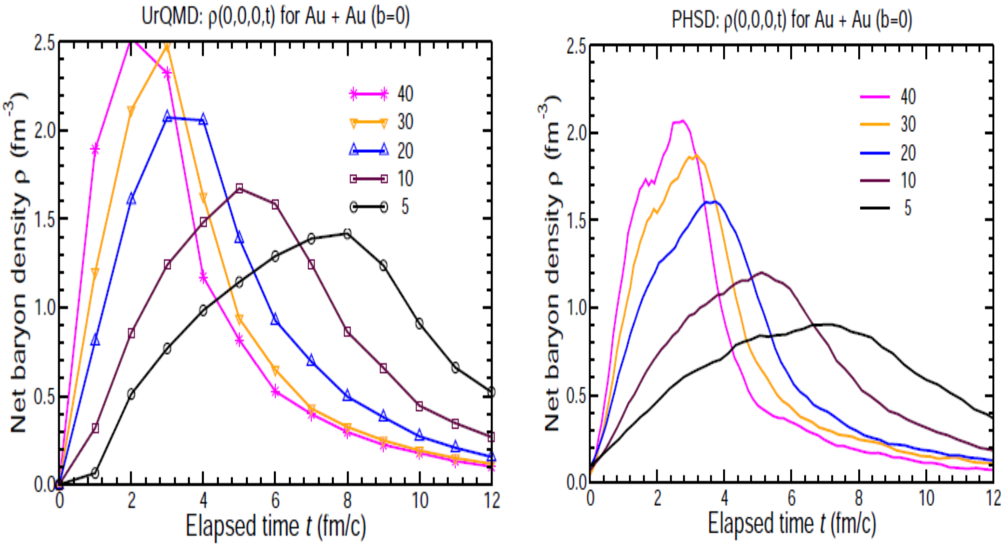

(a) (b)

Fig. 2.2 Time evolution of net baryon density for central Au+Au collisions at the centre of the collision zone at different beam energies for different transport models [75]. The calculations of the net baryon density were donne with : a) UrQMD [76] and b) PHSD models.

The high-intensity heavy-ion beams to be delivered by the accelerators at FAIR will provide a unique research opportunity in the field of hadron physics. The SIS100 and SIS300 accelerators will deliver primary beams of protons of up to 89 GeV and Uranium nuclei of up to 35 $AGeV$, nuclei with $Z/A = 0.5$ of up to 45 $AGeV$ and secondary beams (rare isotopes and antiprotons) with high intensity and unprecedented quality. These heavy-ion beams are suitable to explore the properties of dense baryonic matter, which exists in neutron stars and cores of collapsed supernova. According to the transport model calculations, in the above energy range in central Au+Au collisions, energy densities of up to 2.5 GeV/fm^3 and baryon densities of about 10 times (35 $AGeV$ (SIS300)) or up to 7 times (11 $AGeV$ (SIS100)) the normal nuclear matter density can be achieved in the centre of reaction zones. The calculated baryonic density using transport model is illustrated in Fig. 2.2. During such conditions, the colliding nuclei would overlaps and a transition to quarkyonic phase or even quark-gluon plasma is expected. A dedicated research program was, therefore, proposed to investigate properties of nuclear matter at high baryonic densities and moderate temperatures at FAIR known as the Compressed Baryonic Matter experiment.

2.3 Diagnostic probes sensitive to high-density fireball

Fig. 2.3 depicts three snapshots of the evolution of a heavy-ion collision at FAIR energies as predicted by UrQMD model [76] and illustrates the time evolution of various particle species. Particles made up of charm quarks are expected to be created in the very first stage of the reaction, hence, D mesons and J/Ψ are the key probes for the dense fireball and its degrees of freedom. LMVM are continuously created by $\pi^+\pi^-$ annihilation during the course of reactions, and they decay either into mesonic or dileptonic channels. As the produced lepton pairs are not affected by the final-state interactions, they, therefore,

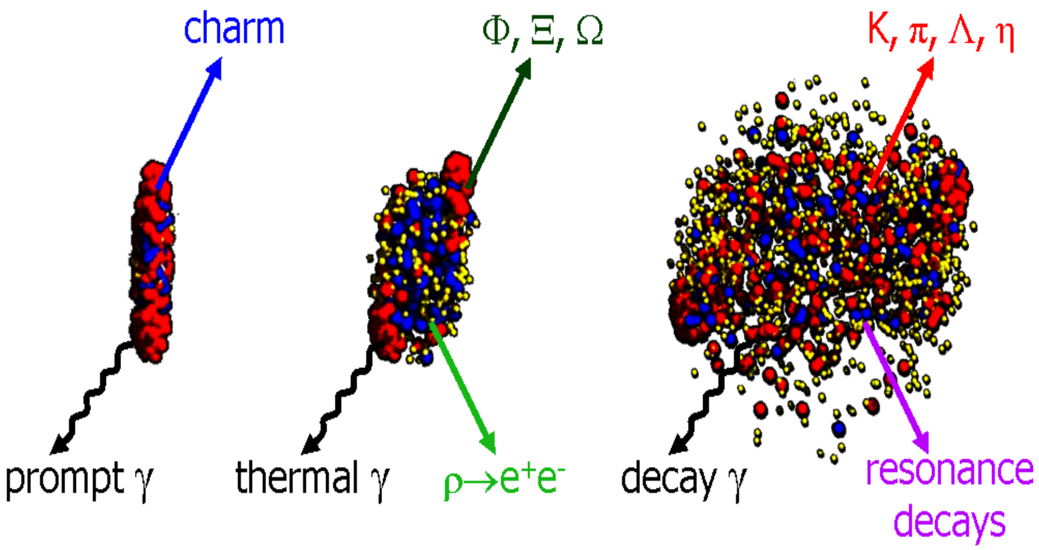

Fig. 2.3 A snapshot of various stages of a U+U collison at E_{Lab} *= 23 AGeV as calculated with UrQMD model [76]. The two Lorentz-contracted nuclei overlap at the initial stage (left), creation of high density phase (middle) and the freeze-out stage, where the final stage hadrons are produced (right). Different particles are created in different stages of the collision or emitted at different times from the collision region [77].*

carry information about the dense fireball. In particular, the short-lived ρ^0 meson is a promising diagnostic probe of the hot and dense nuclear matter. The multi-strange hyperons and ϕ^0 mesons with small hadronic cross sections, provide information on the dense phase of the collisions, especially via their collective flows. Finally, the bulk of the particles freezes out at densities below the saturation density. Till date, essentially these freeze-out particles have not been measured in heavy-ion collisions at beam energies between 2 - 40 *AGeV* in the fixed-target experiments. These signals coming from the high-density stage of the fireball, will be measured for the first time by the CBM experiment in this beam energy range. The CBM experiment, therefore, has a unique discovery potential at both SIS100 and SIS300 energies.

2.4 Physics goals of CBM experiment

Heavy-ion beams supplied by SIS100 and SIS300 will be used by CBM experiment to discuss the following important physics issues [69, 74] :

- Exploration of equation-of-state of matter at high baryonic densities;
- Search for deconfinement and/or chiral phase transition, including a critical point;
- Deconfinement phase transition and investigation of possible new phases such as quarkyonic matter or quark-gluon plasma at high baryonic densities;
- The production and study of multi-strange hypernuclei; and
- Search for di-baryons and strange meta-stable particles.

2.5 Diagnostic key observables in CBM experiment

In order to address all the above issues, the CBM experiment is designed to measure excitation functions of a wide range of particles covering a large region of the phase-space. The relevant physics observables are :

- **Strangeness :** Production of multi-strange hyperons at threshold beam energies proceeds via strangeness exchange reactions. The production of multi-strange hyperons is favored at higher densities, where the mean free path between consecutive collisions is small, hence, their yields depend on the density and compressibility of baryonic matter at these densities. Moreover, a detailed measurement of excitation function of the yields, their phase-space distributions and the collective flow of these hyperons in heavy-ion collisions at beam energies between 2 - 40 $AGeV$ (SIS100 and SIS300) will provide new information on the equation-of-state of nuclear matter over a wide range of baryon densities.

  A non-monotonic behavior of the inverse-slope parameters as a function of beam energy would signal a change in the nuclear matter properties at a certain net baryon density. The inverse-slope parameter of the transverse-mass distribution as a function of particle mass is related to the particle freeze-out time, and, hence, may help disentangle the early stages of collision.

- **Dileptons :** A precise measurement of the invariant mass spectrum of the dileptons up to 1 GeV will provide information on the in-medium properties of the LMVM spectral function as a promising signature of the chiral symmetry restoration in the hot and dense nuclear matter. The intermediate mass region of the invariant mass spectrum, 1 - 3 GeV/c^2, contains a substantial contribution from thermal dileptons from the early partonic phase. The inverse-slope parameters of their transverse-momentum spectra provides information about the origin of the lepton pairs. Measurement of dileptons emitted from the high-density phase of the collision requires determination of contributions from very early nucleon-nucleon collision, from the dilute corona, and from freeze-out.

  The precise and systematic measurement of the in-medium mass distribution of the short-lived ρ-meson is expected to provide information on the conditions and degrees of freedom inside the hot fireball produced in heavy-ion collisions.

  Thus, the in-medium invariant mass distribution of LMVM decaying into lepton pairs in the heavy-ion collisions at FAIR energies (SIS100 and SIS300), is a promising diagnostic indicator of the onset of chiral symmetry restoration.

- **Collective flow :** The strength of the elliptic flow, v_2, measured as a function of transverse-momentum for various particle species sheds light on the degrees of freedom, which prevails in the early stage of the collision.

  The multi-differential flow measurements of strange hadrons and antibaryons for a variety of collision systems and beam energies in the SIS100 and SIS300 energy range will provide information about the degrees of thermalisation, equation-of-state and in-medium properties of strange particles.

- **Fluctuations and correlations :** The presence of a phase coexistence region is expected to cause strong fluctuations from event-to-event in the charged particle numbers, baryon numbers, strangeness-to-pion ratio, average transverse momentum, etc. Similar effects are predicted to exist in the vicinity of the QCD critical point.

During the deconfinement phase transition, critical density fluctuations have been predicted. This density fluctuations cause non-statistical event-by-event fluctuations, like K/π shows a "horn-like" structure in the energy range of 30 - 40 $AGeV$ (Fig. 1.10) [61]. This horn like structure is expected to be a signature of the onset of deconfinement. Thus, study of event-by-event fluctuations in the hadro-chemical composition of the particle source offers a possibility to directly observe effects of a phase transition. A sudden anomalous change in the dynamical fluctations would be a signal for the existence of the critical point and is regarded an important observable at FAIR energies.

- **Hypernuclei :** Hypernuclei are the nuclei containing at least one hyperon

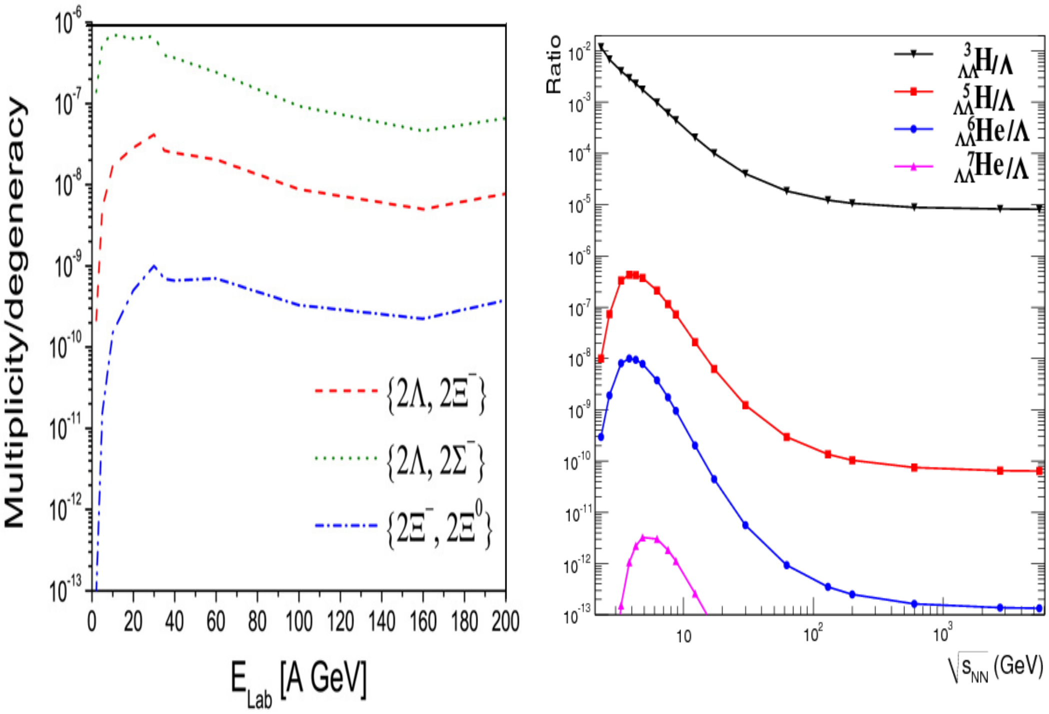

(a)

(b)

Fig. 2.4 (a) Excitation functions of the multiplicities of various MEMOs and hypernuclei in central Pb+Pb reactions from the UrQMd hybrid approach, (b) energy dependence of ratio of the yields of multi-strange Λ hypernuclei and Lambdas at mid-rapidity for central nucleus-nucleus collisions calculated with the statistical model.

in addition to nucleons, and offer a fascinating perspective to explore the third, strange dimension of the chart of nuclei. Fig. 2.4 (a) displays the excitation function of the yields of various Metastable Exotic Multi-hypernuclear Objects (MEMOs) in central Pb+Pb collisions from the hybrid approach by using SHASTA algorithm [78, 79] of UrQMD model, (b) shows a prediction within the thermal model [80] for the energy dependence of the production yields of multi-strange light hypernuclei [81].

It can be observed from Fig. 2.4 that the yields of meta-stable exotic multi-hypernuclear clusters increases with increasing baryon density and has a maximum in heavy-ion collisions at FAIR energies, up to $\sim 11\ AGeV$. Search for composite objects with multiple strangeness quantum number is, therefore, very promising at SIS100. These objects can be identified via their weak decays into a pair of lambda hyperons.The heavy-ion beams of high luminosity supplied by FAIR together with state-of-the-art detector technology at CBM, is the best place for the search of these observables; their studies might provide information on hyperon-nucleon and even hyperon-hyperon interactions.

- **Open and hidden charms :** Transport properties of mesons with charm quarks in dense medium can be studied via the yields, the elliptic flow and the momentum distributions of charmed particles. In a baryon-rich medium these observables are expected to differ in D and $\bar{D}$ mesons. The elliptic flow of charmonia and open charm is sensitive to initial pressure, which might be of partonic nature. The measurement of flow in heavy-ion collisions from 2 to 40 $AGeV$ is, therefore, a sensitive observable for the indication of occurrence of deconfined phase transition at high baryonic densities.

  A global m_T-scaling of all mesons, especially strange and charmed particles, indicates in-medium modifications, which may be related to effects of chiral symmetry restoration.

  The crossing of the phase boundary may be indicated by sudden changes of charm particle ratios such as yields of Ψ' and J/Ψ and the J/Ψ and D meson measured as a function of beam energy and is also an indicator of deconfinement phase transition.

The key feature of the CBM experimental program involves systematic and comprehensive measurements of excitation functions and system size dependences of all the above observables. In particular, the measurement of rare diagnostic probes such as dileptons and charmonia, which are not measured by other experiments in the FAIR energy regime. The measurement of these rare probes requires a beam of high intensities, a large duty cycle, excellent beam quality and running times of several months per year, which is possible at FAIR. Event-by-event fluctuations requires full azimuthal coverage of the produced particles in a wide acceptance of rapidity and transverse momentum and excellent centrality determination. Measurement of these observables by the CBM experiment is discussed in the next chapter.

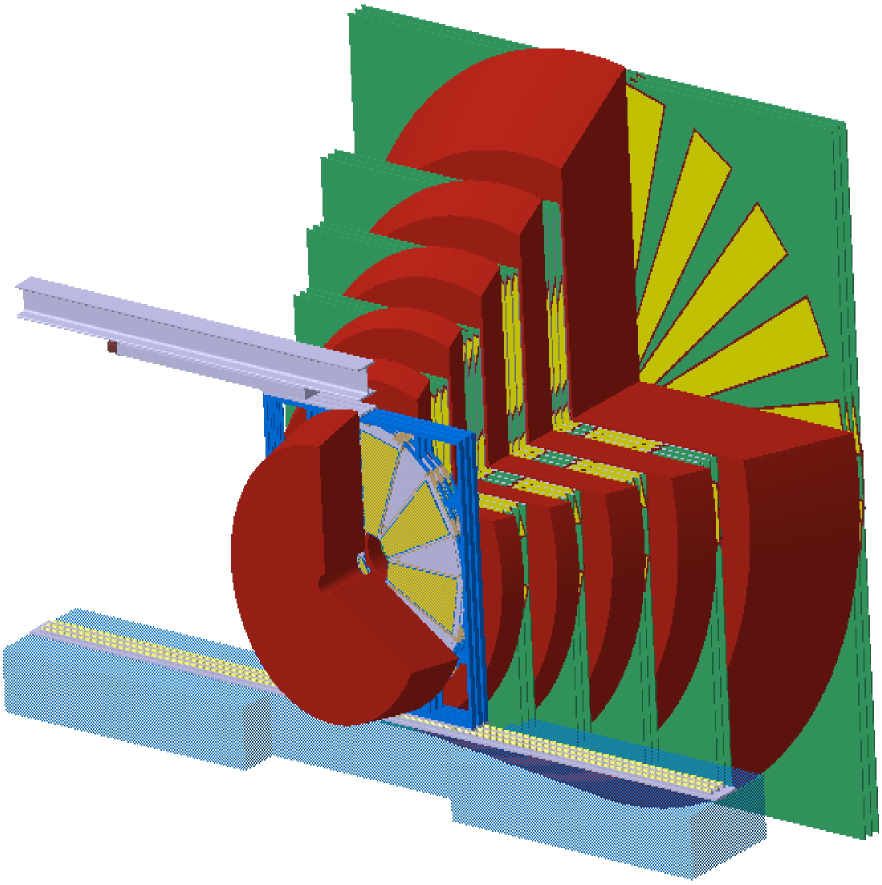

The Compressed Baryonic Matter Experiment

Chapter 3

The Compressed Baryonic Matter Experiment

One of the prime aims of Compressed Baryonic Matter experiment at FAIR, a fixed-target experiment, is to explore the QCD phase diagram in the region of moderate temperature and high baryonic density, complementary to the LHC and RHIC experiments. The main emphasis of the experiment is to focus on the investigation of phase transition from hadronic matter to partonic matter and the QCD critical point. The highest baryonic density at freeze-out can be achieved at relatively lower CERN-SPS and FAIR energies as displayed in Fig. 3.1. This figure shows the variation of chemical freeze-out temperature as a function of net baryon density. The statistical model calculations, as can be noticed from Fig. 3.1, reveal that the highest net baryonic density in heavy-ion collisions can be achieved by using the ion beams of energies lying in the range; 30 - 40 $AGeV$ or $\sqrt{s_{NN}}$ = 6 to 10 GeV [82]. Ongoing experiments like BES in STAR and PHENIX at RHIC, NA61/SHINE at CERN-SPS and proposed experiments like MPD at NICA and CBM at FAIR aim to investigate the QCD phase diagram in this energy regime. Due to the limitations of luminosity the experiments like STAR and PHENIX, NA61/SHINE and MPD, focus on the investigation of bulk observables. These observables are predominantly sensitive to the late and dilute phase of collisions when most of the particles freezes out. On the other hand, the research program of the CBM experiment at FAIR aims to measure diagnostic rare probes of the early and dense phase of the fireball evolution. The high luminosity beams of a wide range of SIS100 and SIS300 energies, supplied by the FAIR accelerator along with the fast detector

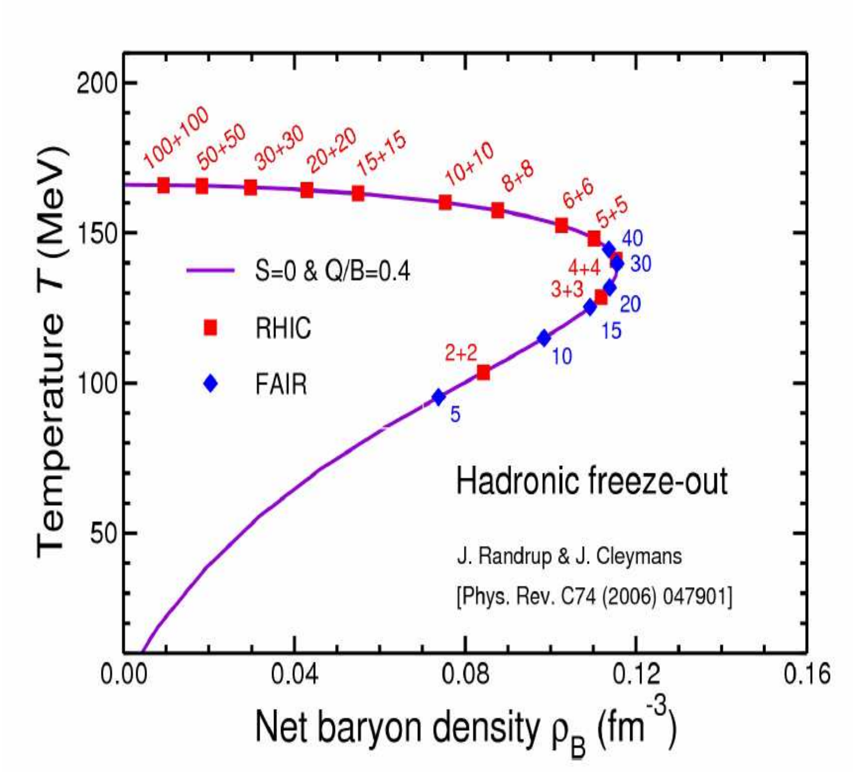

Fig. 3.1 The hadronic freeze-out curve as a function of temperature and net baryon density. The values are predicted by a thermal-statistical model with values of μ_B *and* T *extracted from the experimental data. The curve refers to Au + Au collisons, where red symbols represent total energy of each beam for RHIC experiment and blue symbols correspond to FAIR (kinetic energy for fixed-target experiment) [83]. The figure is taken from[84].*

set-up makes CBM experiment unique to explore the region of dense baryonic matter. Table 3.1 summarizes various futures and ongoing experimental programs to study the dense baryonic matter and details of various physical observables to be measured. The CBM scientific program has been designed to scan diverse observables, beam energies and colliding systems. The central goal of the experiment is to measure different observables, including low mass dilepton pairs, charmonia, open charm and also study collective flow of rare and bulk observables, correlations and fluctuations with unprecedented precision and statistics despite low multiplicities of the collisions. Fig. 3.2 depicts the values of multiplicities times branching ratio for various particles produced in the central Au+Au collisions at $E_{Lab} = 25\ AGeV$. The data points are calculated using either the HSD transport code [86] or thermal model based

Table 3.1 Energy ranges, reaction rates (limited by luminosity (LL) or by detector (LD)) and observables (like hadrons, correlations and fluctuations, measurement of dileptons, and charm) measured or to be measured at $\sqrt{s_{NN}}$ = 8 GeV for Au+Au or Pb+Pb used by current (STAR, PHENIX, NA61/SHINE) and future experiments (MPD, HADES and CBM at FAIR) on dense baryonic matter [85].

Experiment	$\sqrt{s_{NN}}$ (GeV)	Reaction rates (Hz)	Observables			
			hadrons	correlations fluctuations	dileptons	charm
PHENIX, STAR @RHIC	7-200	1-800 (LL)	✓	✓	✗$^{(1)}$	✗
NA61/ SHINE @SPS	6.4-17.4	80 (LD)	✓	✓	✗	✗
MPD @NICA	4-11	$\approx 10^3$ $^{(2)}$	✓	✓	✗	✗
CBM, HADES @FAIR	2.7-8.3	10^5-10^7 (LD)	✓	✓	✓	✓

(1) with the planned BES II at RHIC, after upgrading the accelerator, dileptons might become accessible also at lower RHIC energies.
(2) design luminosity of 10^{27} $cm^{-2}s^{-1}$ for HI

on the assumption of the values corresponding to temperature and baryon-chemical potential [64]. In order to produce huge statistics of the data for low yields, CBM experiment is designed to run exceptionally at high reaction rates of up to 10 MHz. These experimental constraints require fast and radiation hard detectors, free-streaming readout electronics, an ultra-fast online event-selection, and a high-speed data processing and acquisition (DAQ) system, which are able to perform high speed online tracking and selection of displaced vertices with the highest precision required for open charm measurements. The experimental studies at FAIR will be carried out depending on the availability of the accelerators. In the first FAIR construction stage, the beams of up to 11 $AGeV$ gold nuclei, 14 $AGeV$ calcium nuclei and 29 GeV protons will be delivered by the SIS100 accelerator. A reduced version of the CBM detector will be installed to measure multi-strange hyperons in heavy-ion collisions and charmed particles in proton induced reactions at SIS100 accelerator. The full

CBM set-up will be installed in parallel to the construction of the SIS300 accelerator which will provide beam of 89 GeV protons and gold nuclei of 35 $AGeV$, which will be able to measure the expected global observables.

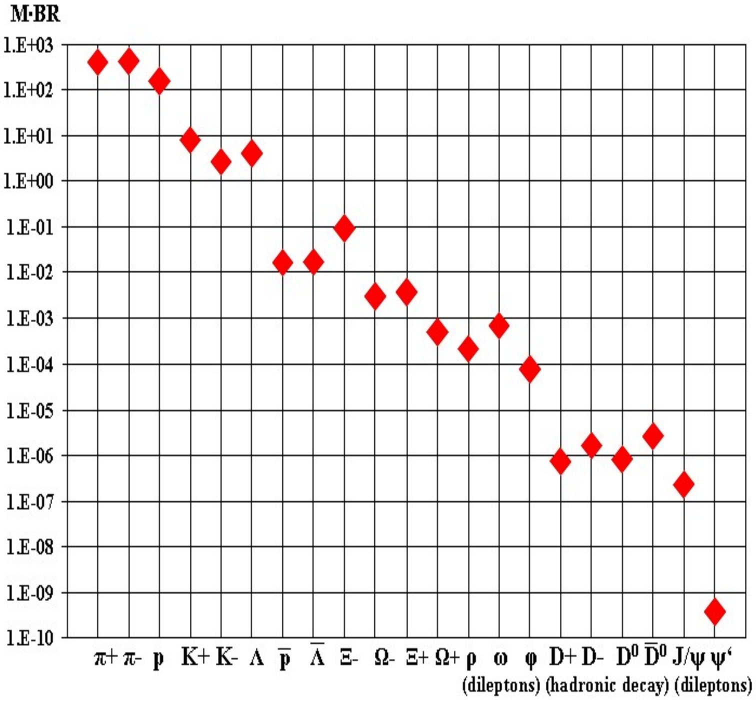

Fig. 3.2 Predicted values of particle multiplicities times branching ratio calculated by HSD model [86] and the statistical model [64] for central Au+Au collisions at 25 AGeV. LMVM, ρ^0, ω^0, ϕ^0 and J/Ψ, Ψ', are envisaged to decay into dilepton pairs, whereas D mesons undergo hadronic decay into kaons and pions.

3.1 CBM detector concept

The CBM experimental layout is shown in Fig 3.3, exhibiting both electron and muon detection systems. The detector set-up consists of Silicon Tracking and vertex detection System (STS) as its central part, stationed in a larger acceptance magnet dipole (±25° polar angle) along the beam direction. It is used for measuring trajectories of produced particles and their momenta. The Micro-Vertex Detector (MVD) measures secondary vertices of charmed hadrons with high accuracy hosted by the dipole magnet. The Ring Imaging Cherenkov (RICH) detector will identify electrons having momenta below 10

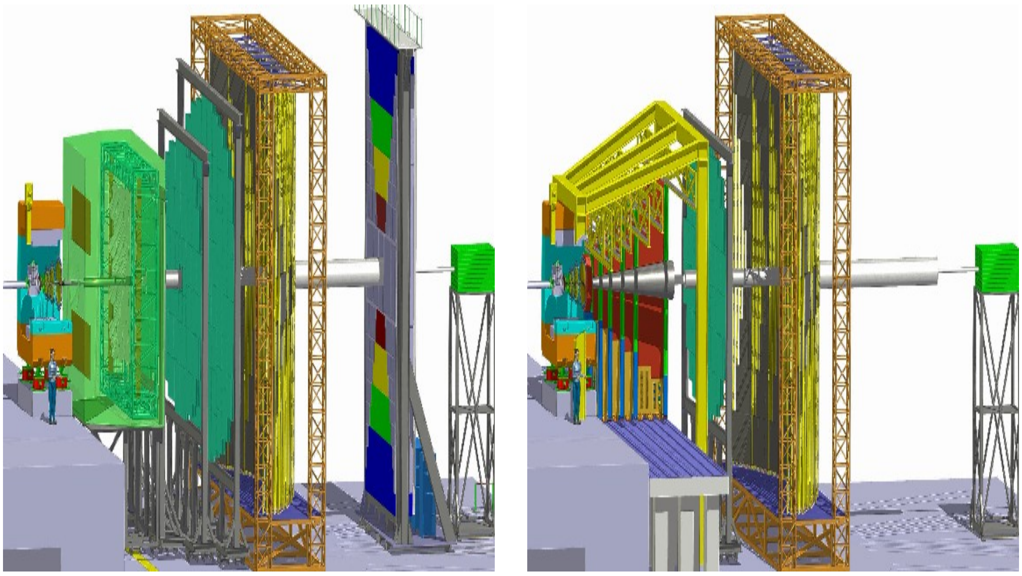
(a) (b)

Fig. 3.3 The CBM experimental set-up planned at FAIR comprises of large acceptance dipole magnet, Silicon Tracking System (STS) and Micro-Vertex Detector (MVD) for tracking and vertex determination, Ring Imaging Cherenkov detector (RICH) and Transition Radiation Detectors (TRD) for identifying electrons [Fig. (a)], Muon Chamber (MuCh) for muon identification [Fig. (b)], Resistive Plate Chambers (RPC) for time of flight measurements, Electromagnetic Calorimeter (ECAL) for photon identification, and Projectile Spectator Detector (PSD) for centrality and reaction plane determination [69].

GeV/c, coming from the decays of LMVM and Transition Radiation Detectors (TRD) will identify electrons having momenta above 1.5 GeV/c. For muon detection, Muon Chamber (MuCh) consisting of three detector triplet for SIS100 version, which will be upgraded to six detector triplets for SIS300 shall be used. Both RICH and MuCh are movable and will replace each other alternatively for muon and electron detection. The time-of-flight technique will be used for identifying hadrons which will be bestowed with wall of multi-gap Resistive Plate Chamber (RPC) positioned at 10 m distance behind the target. Measurement of direct or decay photons, from low mass vector mesons, will be performed by Electromagnetic CALorimeter (ECAL). The forward calorimeter called Projectile Spectator Detector (PSD) will be used for the determination of collision centrality and orientation of the reaction plane. The details of CBM detector components and corresponding observables are summarized in

Table 3.2.

Table 3.2 Observables and different sub-detectors : MVD, STS, RICH, MuCh, TRD, RPC, ECAL, and PSD. Detectors marked as (x) can be used to reduce background [69].

Observables	**MVD**	**STS**	**RICH**	**MuCh**	**TRD**	**RPC**	**ECAL**	**PSD**
π, K, p		x	(x)		(x)	x		x
Hyperons		x			(x)	(x)		x
Open Charm	x	x	(x)		(x)	(x)		x
Electrons	x	x	x		x	x		x
Muons		x		x		(x)		x
Photons							x	x
γ via $e^{\pm}$	x	x	x		x	x		x

3.1.1 Dipole Magnet

The magnet is of the H-type as shown in Fig 3.4. It will be superconducting in order to reduce the operational costs. It supplies a vertical magnetic field with a bending power of 1 Tm over a length of 1 m from the target. It is positioned immediately nearest to RICH or MuCh detector of the experimental set-up. The magnet gap has a height of 140 cm and a width of 250 cm for accommodating the STS with polar angle acceptance of $\pm25°$ and horizontal acceptance of $\pm30°$. The magnet has warm iron yoke/pole and cylindrical superconducting coils having 1749 turns in two different cryostats like a SAMURAI magnet at RIKEN [87, 88]. The coil wire similar to the wire used in CMS experiment has Nb-Ti filaments embedded in a copper matrix and solder in copper stabilizer, with a total Cu/Sc ratio of about 13 in the conductor. The operating current and the maximum magnetic field in the coil are 686 A and 3.25 T respectively. The coil case made of stainless steel contains 20 liters of liquid helium required for cooling one coil. The vertical force in the coils is about 250 tons. Six suspension links are used to suspend the cold mass from the room temperature vacuum vessel. Six cylindrical support rods compensate the vertical forces. The magnet can store energy up to 5 MJ. However, to avoid overheating (above T = 100 K) in case of a quench, the energy will be deposited to the external resistor [89].

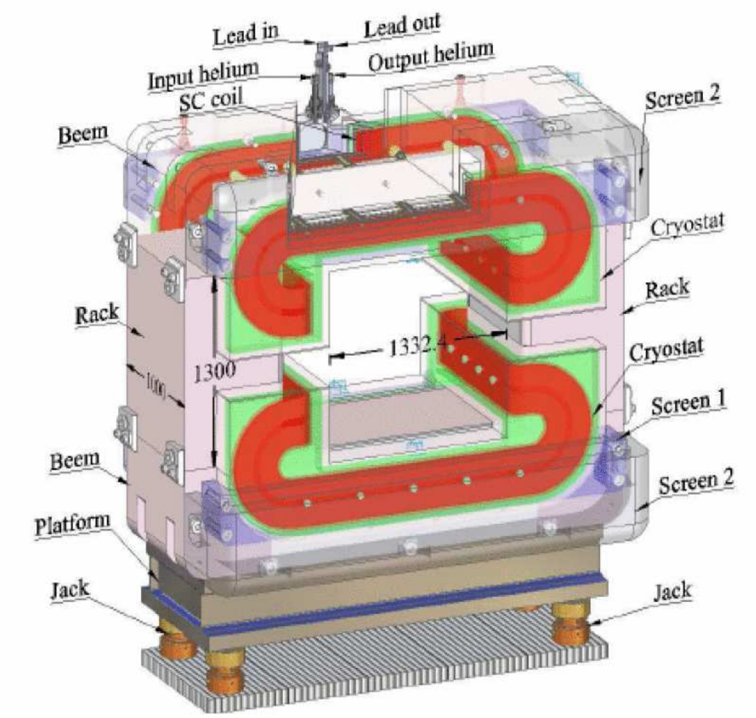

Fig. 3.4 Design of CBM Superconducting magnet and its coil are shown.

3.1.2 Micro-Vertex Detector (MVD)

Short-lived D^0 mesons having $c\tau = 123\ \mu m$ and $D^{\pm}$ mesons having $c\tau = 314\ \mu m$ are identified via their weak hadronic decays into pions and kaons, which require high precision measurements of secondary vertices. This task demands detectors with excellent position resolution and low material budget in order to reduce multiple scattering. These requirements are met by Monolithic Active Pixel Sensors (MAPS). The pixel sizes will be $25 \times 25\ \mu m^2$ and $40 \times 40\ \mu\text{m}^2$ having position resolution of $\sigma = 3.5$ - $6\ \mu m$ depending on the pixel size. The proposed total radiation length for the whole detector station along with the mechanical support will be a total thickness of 300 - 500 μm silicon equivalent. The MVD will comprise of first station (optional) at 5 cm followed by two layers at 10 and 15 cm downstream of the target in vacuum. This MVD detector will allow determination of secondary decay vertex of D mesons with a resolution of around 50 - 100 μm along the beam axis, depending on the thickness and distance from target of 1^{st} MAPS station. The detector has to tolerate a high radiation dose of 10^{13} n_{eq} which is equivalent to 10^{12} minimum bias Au+Au collisions at 25 $AGeV$. The beam intensity is about 10^{9} $ions/s$ and assuming an interaction rate of 100 kHz, a SIS300 detector can be operated for 4 months before replacement of the inner part of the first MVD layer. Hence, MVD will be installed for dedicated measurements of open charm, electrons and improved hyperon identification [69].

3.1.3 Silicon Tracking System (STS)

The major aim of STS is to perform track reconstruction and momentum determination of charged particles for multiplicities around 600 per event within the detector acceptance. The STS consists of 8 tracking layers of silicon detectors placed within a distance of 30 and 100 cm downstream of the target. The STS will be installed in the dipole magnet of bending power 1 Tm. The detector has been designed to achieve momentum resolution $\Delta p/p = 1\%$ by using ultra-low material budget and with restriction of total thickness 400 - 800 μm silicon equivalent (include front-end electronics, cooling concepts and mechanical support structures) to reduce multiple scattering. The idea of the STS tracking is based on double-sided silicon micro-strip sensors with a stereo angle of 15°, a strip pitch of 60 μm, strip length of 20 - 60 mm, and a thickness of 250 - 300 μm, mounted on light-weight ladder-like support. The modular structure of stations with the above mentioned details are displayed in Fig 3.5. The micro-cables will be made up of sandwiched polyimide-Aluminum layers of thickness up to 10 μm. Typical hit resolution attained will be up to 25 μm with required time resolution of around 10 ns with a collision rate of 10 MHz. The readout electronics required by the detector will be placed within the magnet and the periphery of the detector set-up with realistic set-up of total thickness, including the support structure, might be up to 800 μm silicon equivalent [69, 90].

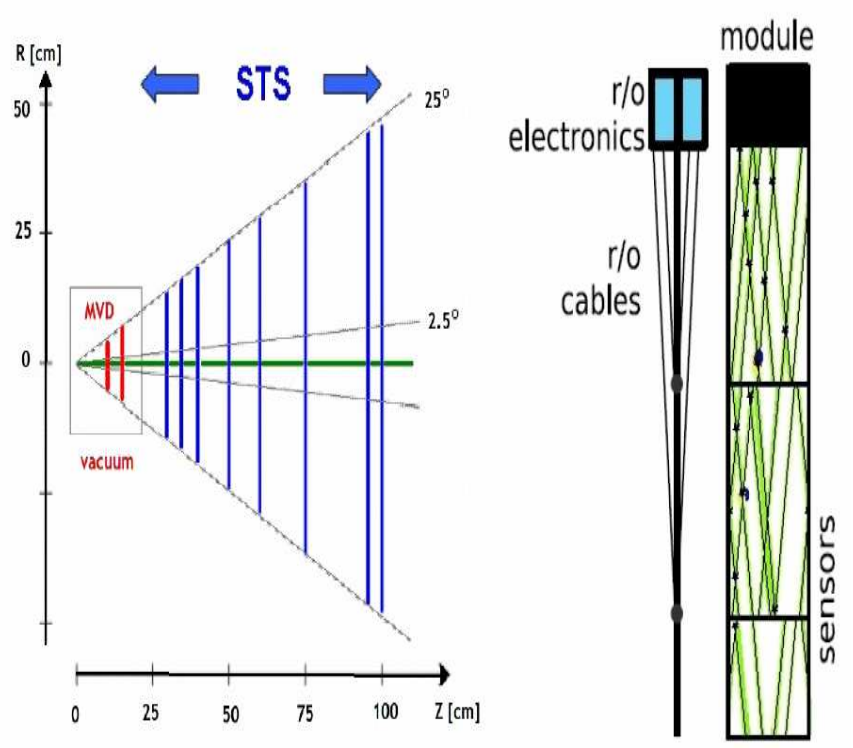

Fig. 3.5 Left : Layout of modular structure of STS along with MVD stations, with indication of station locations and their polar angle coverage. Right : Side and front views of one STS module with the readout electronics [91].

3.1.4 Ring Imaging CHerenkov Detector (RICH)

The RICH detector is proposed for efficient and clean identification of electrons within momentum range $\leq 10\ GeV/c$ in wide detector acceptance and pion suppression of the order of 500 - 1000, which can be further increased up to 10^4 by including TRD and RPC information. To satisfy these requirements the detector design concept comprises of $\approx 2\ m$ long gas radiator filled with CO_2 ($\gamma_{th} = 33.3$, $p_{th,\pi} = 4.56\ GeV/c$), a glass mirror and a Photon Multiplier Tube (PMT) array as photon detectors, located behind the dipole magnet approximately 1.6 m downstream of the target. The mirror plane is bifurcated horizontally into arrays of two spherical mirrors with dimensions up to 4 m × 1.5 m each, 72 mirror tiles of radius of curvature 3 m and thickness of 6 mm and reflective coating of Al+MgF_2. Rings of Cherenkov radiations are projected on the two photon detector planes of dimensions 2 m × 0.6 m each, located behind the CBM dipole magnet with magnet yokes shielding in order to reduce background to cross the detector plane directly. The set-up plan is based on the MAPMTs (e.g., *H8500* from Hamamatsu) for providing high granularity, high geometrical acceptance, high detection efficiency and reliable functioning. The detector components work well in limit of self-absorption by CO_2 radiator for $\lambda \leq 180\ nm$. The sensitivity of the MAPMTs can further be enhanced by applying a wavelength-shifting film coating to PMT window [92]. A detailed description about the detector can be found in [93].

3.1.5 Muon Chamber System (MuCh)

One of the experimental challenges of the CBM experiment is to identify LMVM (e.g., ϕ^0, ρ^0, ω^0) in the environment of high particle density at FAIR energies. The conceptual design of MuCh is to perform tracking of charged particles through a complete set-up (STS + MuCh), which requires highly granular and fast tracking detector set-up to perform momentum dependent muon identification. This concept is achieved by segmentation of hadron absorber into several layers and inserting triplets of tracking detector planes in these gaps. The MuCh detection station is placed downstream of STS, which determines the particle momenta. Compact absorber/detector system has been designed to reduce meson decays into muons. Fig. 3.6 shows the sketch of current MuCh detector system. It comprises of alternating 6 absorbers (60 cm carbon and iron plates of 20, 20 , 30 , 35 and 100 *cm* thicknesses) and 18 gaseous tracking chambers located in triplets behind each absorber. The identification of muons depends on the momentum which varies with the mass of the LMVM and charmonia and beam energy.

The challenge faced by MuCH and for track reconstruction algorithms is high particle density, up to 0.35 $hits/cm^2$ per central event at the first station, which corresponds to a hit rate of 3 MHz/cm^2. Highly granulated gaseous detectors based on GEM technology are, therefore, used. The realistic detector set-up also comprises of straw tube and one TRD station. The total area of the muon detection system is 70 m^2, which is further divided into half a million channels. The prototype of GEM detector has been fabricated and tested. It has been operated successfully at rates of up to 1.4 MHz/cm^2. Due to low particle multiplicities at the last station, trigger has been implemented on muon pairs originating from decays of LMVM and charmonia. The concept of trigger is based on the measurement of short track segments in the last tracking triplet station and extrapolating these tracks in target direction and selected by vertex quality. This trigger can reduce the event rate by a factor of 600 for J/Ψ measurements in minimum bias Au+Au collisions. For J/Ψ measurements at SIS100 energy a MUCH start version with 3 chamber triplets is found to be sufficient [69, 94].

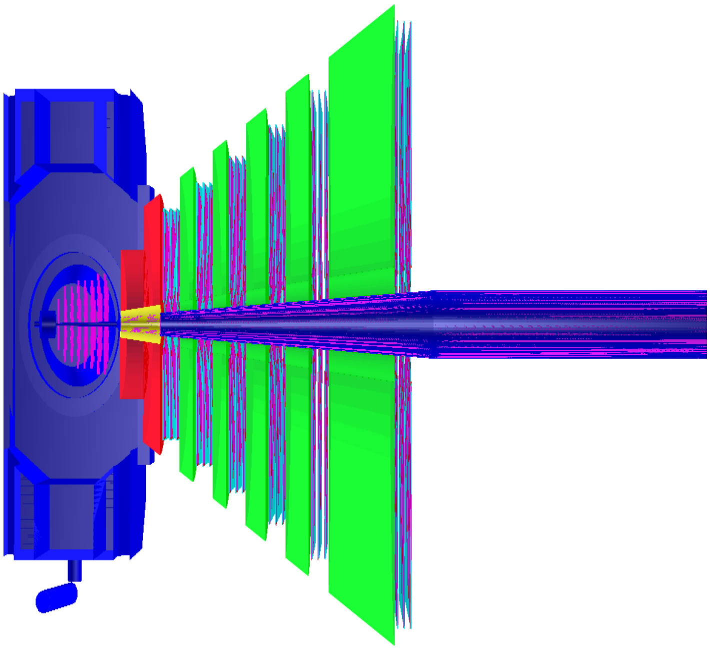

Fig. 3.6 The CBM Muon Chamber at SIS300 consists of 6 alternating absorbers and triplets of tracking chambers. First absorber is made up of carbon and the rest of the absorbers are made up of Iron.

3.1.6 Transition Radiation Detector (TRD)

The TRD detector is based on the principle of emission of electromagnetic radiation (known as Transition radiation), which is emitted when relativistic charged particles traverse at the interface of two media of different dielectric constants. Since the total energy lost by a charged particle while undergoing transition depends on its Lorentz factor $\gamma = E/mc^2$. Hence, TRD is used for discriminating electrons and hadrons (e.g., pions). In the CBM experiment TRD is used for the identification of electrons and positrons with $p > 1.5\ GeV/c$ ($\gamma > 1000$) and tracking of the charged particles. In conjunction with RICH and ECAL, it provides an adequate capability of electron identification for measuring charmonia and LMVM. Therefore, pion suppression factor obtained with 9 TRD layers is estimated to be well above 100 at an electron efficiency of 90%. The current TRD set-up, as displayed in Fig 3.7, consists of three TRD stations each having 3 - 4 detectors with a position resolution of $\sigma =$ 300 - 500 μm across and 3 - 30 mm along the pad. The detector stations are positioned approximately at 5, 7.2, and 9.5 cm downstream of the target, and the total active area of detector will be up to 600 m^2. The prerequisites for TRD are electron identification performance, highly granular and fast gaseous detectors, specifically for the inner part of the detector planes covering the forward emission angles. For the inner detector plane close to about 5 m from target and at small forward angle, the expected particles rate will be of the order of 100 kHz/cm^2 for 10 MHz minimum bias Au+Au collisions at 25 $AGeV$. For the case of central collisions, the particle densities up to 0.05 cm^{-2}

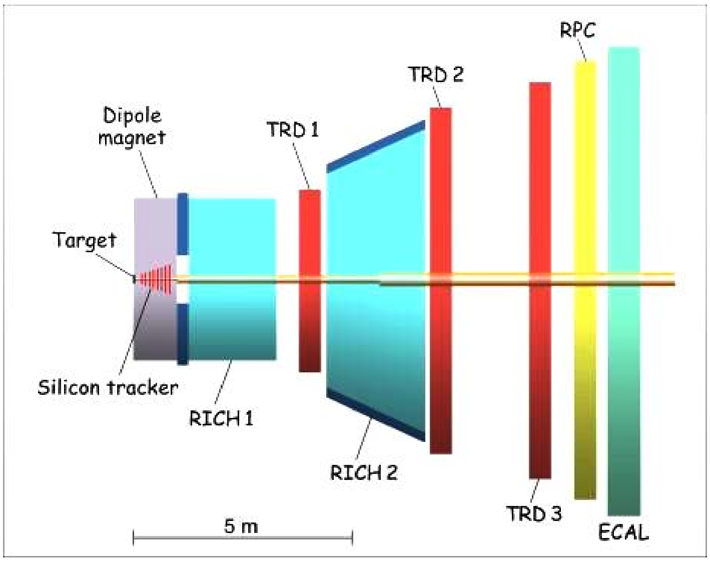

Fig. 3.7 Planned TRD set-up.

can be achieved. The minimum size of the cell is of the order of 1 cm^2 for maintaining an occupancy below 10%. The second TR layer is rotated by 90° for each station [69]. MWPC (Multi-Wire Proportional Chamber) technology and GEM (Gas Electron Multiplier) are utilized for the fabrication of TRD gas detectors, which is tested with particle rates of around 400 kHz/cm^2 without failure of their performances. In order to perform measurements at SIS100, the CBM set-up will use only one station with 2 - 4 detector layers as an intermediate tracker in between the STS and the TOF wall.

3.1.7 Timing Multi-gap Resistive Plate Chambers (MRPC) or Time-Of-Flight wall (TOF)

Hadrons are identified by using an arrangement of Resistive Plate Chambers (RPC) via Time-of-Flight (TOF) measurements. The mass of particle is determined by measuring its momentum p, its time-of-flight and particle track length using

$$m = \frac{p}{\gamma\beta c} = \frac{p\sqrt{1-p^2}}{\beta c} \tag{3.1}$$

where $\beta = \frac{L}{c\Delta t}$; L is the flight length of the particle and Δt is the time difference between the start and stop signal of the TOF detector. The start signal for the TOF measurement is provided by diamond pixel (or micro strip) detector and it can directly count beam particles at intensities of around 10^9 $ions/s$. The TOF wall comprises of $\approx$ 60,000 independent cells which provide a time resolution of $\sigma_{TOF} \leq 80$ ps and has an active area of about 150 m^2. The TOF wall is located at distance of 6 m downstream of the target for carrying out measurements at SIS100 and at 10 m for SIS300. The requirements of TOF detector can be fulfilled by the high resolution and high rate timing RPCs with a acceptance of 25 - 30°. The hit rates in the inner most part of the detector is 25 kHz/cm^2 and 10 kHz/cm^2 for the outer area. The pad area in the this region is about 5 cm^2 and the corresponding occupancy is up to 5% at SIS300. With the proposed pad readout a position resolution of 6 mm is expected across the pads, whereas the resolution along the pads exhibits that the dependence on the pad length and pad lengths increase with distance along the beam pipe. Prototype of the first MRPCs with low resistivity glass electrode has been built and tested. A $\Delta t = 120\ ps$ can be achieved at hits rate of 18 kHz/cm^2 [95] with an efficiency of 95%. Fig. 3.8 exhibits the separation ability of TOF detector for kaons, pions and protons obtained by realistic simulation [96]. The separation of pions and kaons can be achieved up to p_{Lab} = 3.5 GeV/c and proton can be identified at p_{Lab} = 7 GeV/c with overall detector efficiency of 80 - 90%.

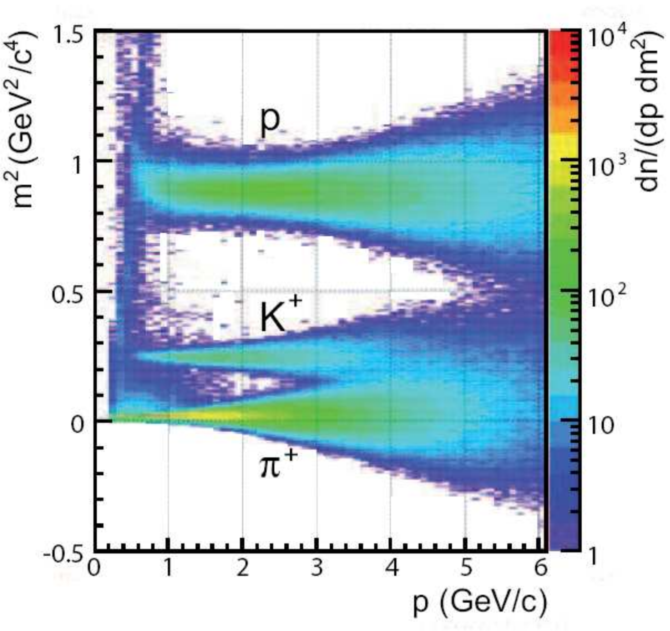

Fig. 3.8 Squared mass as a function of momentum reconstruction of hadrons by TOF in central Au + Au collisions at 25 AGeV beam energy.

3.1.8 Electromagnetic Calorimeter (ECAL)

Direct photons and decay photons from neutral mesons (π^0 and η) will be measured by 'shashlik' ECAL. The planned ECAL will comprise of modules of 140 layers of 1 mm lead and 1 mm scintillator. The envisaged cell sizes are 3 × 3, 6 × 6 and 12 × 12 cm^2. The detector modules can be arranged either as a wall or in a tower geometry, located at variable distance from the target [69].

3.1.9 Projectile Spectator Detector (PSD)

The collision centrality and the orientation of the reaction plane will be determined by employing PSD, which is a full compensating modular(12 x 9 individual modules) lead-scintillator calorimeter. In order to study event-by-event observables and collective flow, accurate measurements of these parameters are required. The reaction plane is determined by a technique which does not include participating particles in the collisions. However, the detector is planned to measure the number of spectator nucleons of the projectile nucleus in A+A collisions. High quality and uniform energy resolution can be achieved by PSD. The detector set-up consists of 44 individual modules, each having 60 lead/scintillator layers with a surface area of 20 × 20 cm^2. The photons coming from scintillators are readout via wavelength shifting (WLS) fibers by Multi-Avalanche Photo-Diodes (MAPD) with an active area of 3 × 3 mm^2 having a pixel density of $10^4/mm^2$ [69].

3.1.10 Online event selection & Data AcQuisition (DAQ)

For the measurement of rare probes having small production cross sections with high statistical precision, high reaction rates are required. In order to cope with the event rates of 10 MHz, corresponding to a beam intensity of 10^9 $ions/s$ and 1% interaction target, an efficient online event selection and Data Acquisition (DAQ) are required. Assuming a storage rate of 1 $GByte/s$ and an event data volume of 10 $kBytes$ corresponding to the minimum bias Au+Au collisions, an event rate of 100 kHz can be processed by the data acquisition. This explains the requirement of online event selection algorithms for the purpose of extracting signal events from the background events. The selection of events will be done by a fast online event reconstruction running on a high-performance computer farm equipped with many-core CPUs and graphic cards (GSI GreenIT cube). Various many-core architectures developed by Intel, IBM, NVIDIA and AMD are under investigation to make use of parallel programming on the heterogeneous CPU/GPU systems. This technique of parallel programming is used in track reconstruction, which is based on track finding and fitting algorithms and implements the Cellular Automaton and Kalman-Filter methods.

For the measurement of open charm, triggering will be based on an online search for secondary vertices. This will require high speed tracking and event reconstruction in the STS and MVD. In order to achieve highest suppression factor for J/Ψ measurements, trigger will require highly energetic pair of electrons or muons in the TRD or MuCh. No online selection is possible for low-mass electron pairs due to large number of δ-electrons being produced by STS and measured by RICH. For the case of low-mass muon pairs, some background rejection at trigger level seems to be feasible [69].

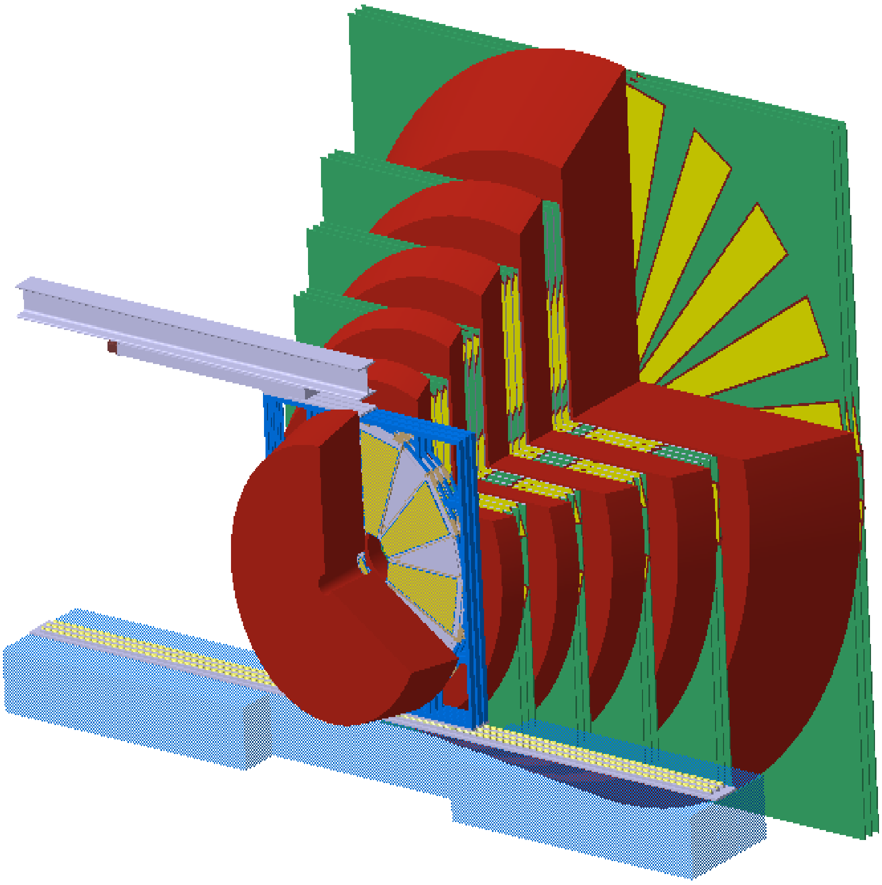

The Muon Detection System of CBM Experiment

Chapter 4

The Muon Detection System of CBM Experiment

The main physics objectives of CBM experiment at FAIR are to study the occurrence of the novel phase transition from hadronic to quarkyonic matter or QGP, identification of QCD critical point, study of yields of metastable or strangelet particles and onset of chiral symmetry restoration by exploiting heavy-ion beams in the energy range of 2 - 40 $AGeV$ (SIS100 and SIS300). The details regarding interesting and new physics from the CBM experiment are presented in Chapter2. The key observables proposed for these studies include measurement of LMVM and charmonia, which are detected via their decays into dileptonic channels. It may be noted that this chapter begins with a brief introduction to dimuon measurements, conceptual design of the muon chambers and details of the simulation analyses.

4.1 Dimuon measurement by CBM experiment

The most important sources of production of lepton pairs, e^+e^- and $\mu^+\mu^-$, are :

- LMVM, specifically ρ^0 with a short lifetime, is envisaged to decay inside the fireball, change its properties in the hot and dense medium. Such in-medium modifications are the indicators of partial chiral symmetry restoration.
- Thermal electromagnetic radiation decays into dileptons, reflect the temperature of the fireball. Thermal lepton pairs are emitted all over during

the collisions and hence, provide integrated information about temperature evolution.

- Charmonia dissociation due to color screening in the deconfined medium is predicted to be a signature of the Quark-Gluon Plasma formation [97].

As the dileptons produced can interact with the particles inside the fireball electromagnetically, hence they can leave the reaction volume almost unscathed. Dileptons are, therefore, considered a very sensitive diagnostic probe for extracting information about the reaction zone. Recent results on dileptons by the DLS [98], HADES [99], CERES [100] and NA60 collaborations [52] have provided information about some important observables in the nuclear physics domain. However, it may be noted that no experimental information about dilepton production in heavy-ion collisions is available in the FAIR energy range. The CBM Collaboration, therefore, plans to systematically measure both dielectrons, e^+e^-, and dimuons, $\mu^+\mu^-$, pairs in p+p, p+A and A+A collisions over a wide beam energy range and various colliding systems. A complementary high-precision data on e^+e^- and $\mu^+\mu^-$ pairs would provide complete information about dilepton radiation off dense baryonic matter. Thus, the CBM experiment has an immense discovery potential at both SIS100 and SIS300 energies.

The experimental challenge in the measurement of dileptons is to suppress the huge combinatorial background of the secondary leptons pairs. In the case of muon measurements, muonic background contains large number of muons arising from the weak decays of pions and kaons, mismatching the hadrons upstream and muons downstream the absorber and by the hadrons hitting through the absorber.

4.2 Conceptual design of muon detection system of the CBM

The most serious experimental challenge of measuring muons in heavy-ion collisions in the FAIR energy regime is identification of low momenta muons in the environment of high particle density. The novel feature of muon detection system of the CBM [101] experiment, in comparison to the existing muon detectors in other HEP experiments, is that the total absorber in the CBM is sliced into thinner segments and tracking chamber triplets are installed in between the absorbers. This system helps capture muon candidates over a wide range of momenta based on the number of absorber segments traversed by them. Hence, there is vast improvement in the detection efficiency of low momenta muons produced via decay of LMVM, which is essential for the reconstruction of LMVM in the Muon Chambers (MuCh). The design of MuCh system have the parameters like the number, thickness and material of the absorber and the number and granularity of tracking chambers, optimized by simulating the response of Au+Au collisions at 25 $AGeV$ beam energy in the lab frame in the fixed-target mode with input particles generated by the UrQMD [76] and PLUTO [102] event generators. The incident particles are then transported through the detector set-up by exploiting the GEometry ANd Tracking (GEANT)3 transport engine [103].

4.2.1 Absorber optimization

Variation of absorption of various particles as a function of absorber thickness is exhibited in Fig. 4.1. It can be seen from the figure that the muons from J/Ψ traverse a distance of $\sim 2.5\ m$ without any substantial suppression, whereas low momenta muons from ω^0 get suppressed by a factor of 10 beyond an iron absorber of 1.5 m thickness. No further signal to background ratio can be improved by including iron absorber beyond 1.5 m. Thus, it can be concluded that the optimized iron absorber thickness for efficient detection of LMVM is

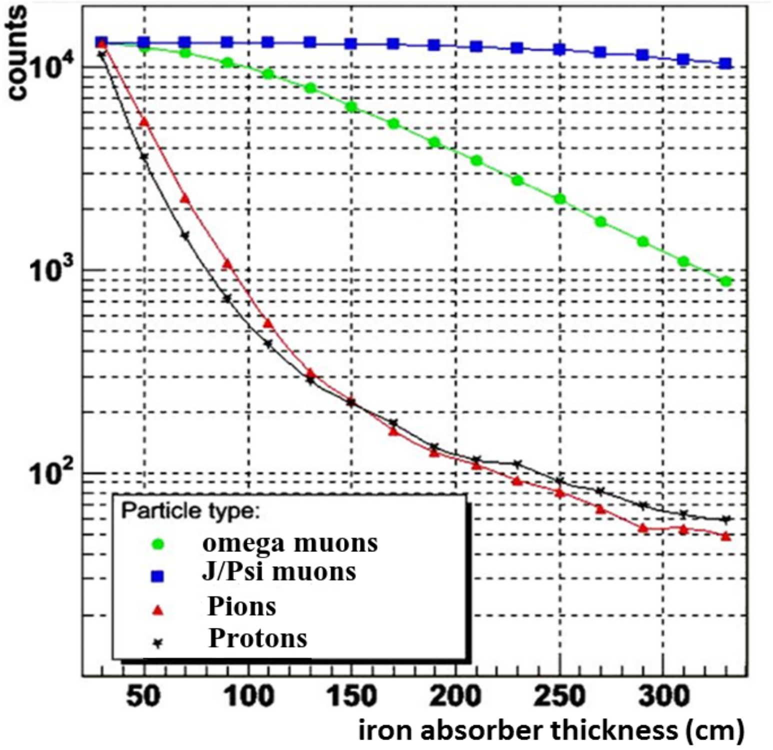

Fig. 4.1 Variation of particle yields with the traversed length in iron absorber. The normalized momenta are taken from the simulation of central Au+Au collisions at 25 AGeV [94].

1.5 m and with an additional iron absorber of thickness 1 m for measuring J/Ψ. The total thickness of MuCh for LMVM detection is 1.25 m of iron, which corresponds to $7.5\lambda_I$, where λ_I is the interaction length. For J/Ψ mesons the total absorber thickness is set to 2.25 m of iron, which is equivalent to $13.5\lambda_I$.

For the selection of absorber material and the optimized thickness of the first absorber layer, one has to make a compromise between hadron absorption and multiple scattering. Since most of the particles fall on the first detector station and have high hit rates. The chosen thickness of the first absorber must, therefore, reduce hadron multiplicity such that the hit rate lie within the limits of tracking chambers for efficient detection. On the other hand, a thick absorber leads to enhanced multiple scattering, thereby increasing mismatching between MuCh track and STS track segments. This increases the reconstructed background. The absorbing material should have small

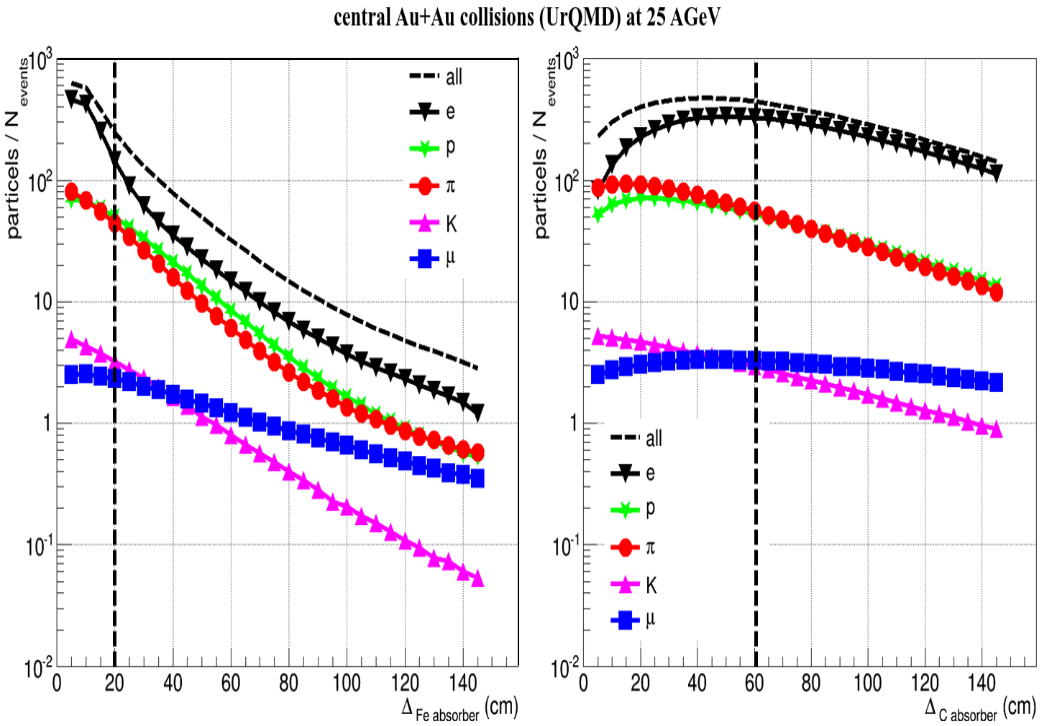

Fig. 4.2 Variations of yields of both primary and secondary particles produced in central Au+Au collisions at 25 AGeV as a function of the thickness of an iron absorber (left) and a carbon absorber (right) [94].

interaction length ($\lambda_I \propto A^{1/3}$) so that hadrons may be absorbed and must have large radiation length ($X_0 \propto A/Z^2$) for reducing multiple scattering. For this optimization, simulation studies have been done with two types of materials, iron and carbon.

Fig. 4.2 shows variation of particle multiplicity as a function of absorber thickness for the central Au+Au collisions at 25 AGeV beam energy. The simulation studies show that for both absorber materials, the particle multiplicity is dominated by the yield of secondary electrons that rises initially and then gradually drops with increasing absorber thickness. The vertical dotted lines display the first absorber thickness for both types of materials of comparable interaction lengths. It can be seen from Fig. 4.2 that absorption for the case of iron is stronger in comparison to carbon, favouring selection of iron as subsequent absorber material. As the first absorber will be placed inside a high magnetic field of CBM dipole magnet and due to mechanical integration, carbon is found to be the favourite choice. Due to large radiation length (for C, $X_0 = 22.1$ *cm* and for Fe, $X_0 = 1.92$ *cm*), amount of multiple scattering suffered by particles traversing through carbon is much less than that for iron. It, therefore, helps improve the matching efficiency and reduce the number of fake background tracks as seen in the left panel of Fig. 4.3; this figure shows the ratio of reconstructed to accepted tracks as function of absorber thickness. This study clearly indicates sharp increase of reconstructed background with increasing thickness. From the right panel of Fig. 4.3 it can be seen that for absorber thickness from 10 to 40 *cm*, the background increases by a factor of 10. Thus, iron absorber thickness of 20 - 30 *cm* or equivalently carbon absorber of thickness 60 *cm* seems to be the optimum choice [104]. The first absorber is divided into two pieces. The 40 *cm* thick first piece is mounted inside the dipole magnet, whereas the rest (20 *cm*) is placed outside the magnet. In order to avoid residual magnetic field, all the iron absorbers are made up of stainless steel instead of soft iron, which is non-magnetic in nature. An additional lead shielding is used around the beam pipe to reduce the background of secondary electrons produced in the beam pipe. The lateral

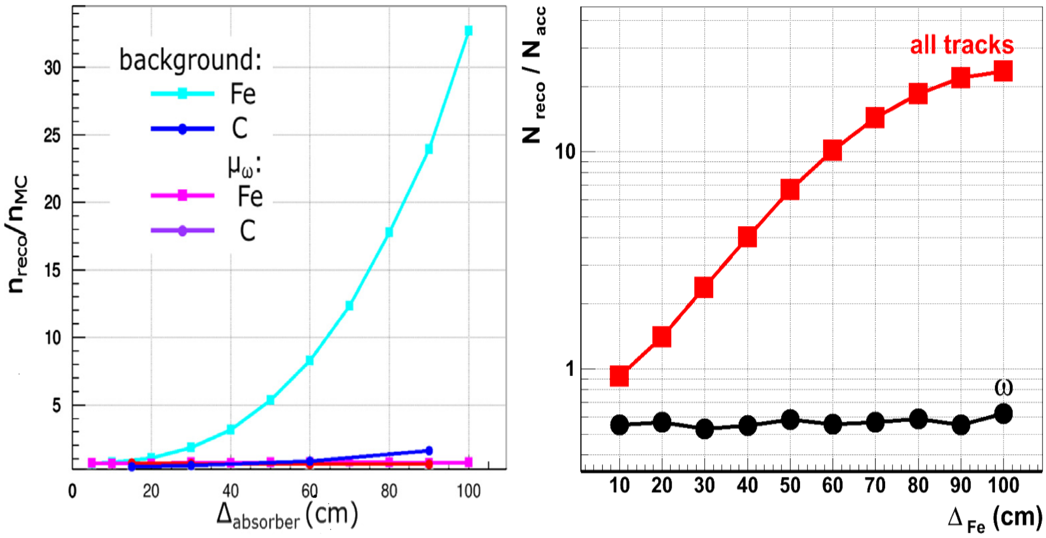

Fig. 4.3 Ratio of the numbers of reconstructed and accepted tracks as a function of thickness of the first absorber. The simulation has been done for Au+Au collisions at 25 AGeV for iron absorber [104].

sizes of the absorbers are sufficient to completely shield the detectors from the primary particles emitted from the target.

4.2.2 Tracking chambers of Muon Detection System

The muon detection system comprises of sliced absorbers and triplet of tracking chambers (angular acceptance of $\sim$ 5 - 25 °) placed in the air gap between the two absorbers of 30 *cm* thickness each. This air gap is also required for accommodating the complete detector, including cooling arrangements and other mechanical structure. Each tracking chamber consists of a detector built on specific detector technology. The following are the experimental and technical challenges for the fabrication and building of large area detector with high position resolution and high detector efficiency:

- Depending on the location of the detector layers, particle density of 1 - 10^{-4} cm^{-2} is confronted by the detector layers. They determine the profile and segmentation scheme of the detectors.
- Detector layer has to handle an interaction rates of up to 10 MHz. The interaction rate along with particle density measure the particle hit rate. The maximum hit rate faced by the first detector layer is 3 MHz/cm^2 (particle density × hit rate).
- The size of detector layer increases with increasing distance from the target, which requires fabrication of detectors of larger areas.
- As the first detector layer is envisaged to encounter 10^7 $neutrons\ cm^{-2}sec^{-1}$, hence it should be resistant to neutron flux over both long and short duration and should withstand the energy deposited by the slowly moving ionizing particles.
- Optimum cost of the detector is required.

On the basis of the above constraints and the radiation environment faced by different detector layers, different detector technology will be employed.

Table 4.1 Various micro-pattern gas detectors for MuCh [94]

Parameters	**MWPC**	**GEM**	**Micromegas**
Rate handling (Hz/mm^2)	10^4	$> 5 \times 10^5$	10^6
Gain stability	Drops at 10^4 Hz/mm^2	Stable over 5×10^5 Hz/mm^2	Stable over 10^6 Hz/mm^2
2D Readout	Yes	Yes	Yes
Position resolution (μm)	> 200	50	Good <80
Time resolution (ns)	~100	< 100	< 100
Magnetic Field effect	High	Low	Low
Cost	Expensive, fragile	Expensive, robust	Cheap, robust

The details of the gas detector technologies are tabulated in Table 4.1. From Table 4.1 it seems that GEM or Micromegas are the most suitable gaseous detector options for the first two stations, whereas MWPC can be used for the last stations. On the basis of the values given in the above table, the baseline technology options for MuCh detector stations are summarized in Table 4.2.

Table 4.2 Various technology options for MuCh detector stations. G+M corresponds to combination of GEM and Micromegas [94].

Configuration	1^{st} station	2^{nd} station	3^{rd} station	4^{th} station	5^{th} station	6^{th} station
SIS300	GEM	GEM	Straw or G+M	Straw or G+M	Straw or G+M	TRD
SIS100-A	GEM	GEM	$----$	$----$	$----$	TRD
SIS100-B	GEM	GEM	$----$	Straw or G+M	Straw or G+M	TRD

Details about these detectors and the R & D studies regarding fabrication of the GEM detector and beam time testing can be found in TDR of the MUCH [94].

4.2.3 Geometry of MuCh

The layout of optimized geometry for muon detection in heavy-ion collisions at SIS100 and SIS300 energies are shown in Fig. 4.4. Table 4.3 gives the details of various parameters about the MuCh Geometry. In the present simulation GEM is used as a detector in each layer. Modular structure has been implemented

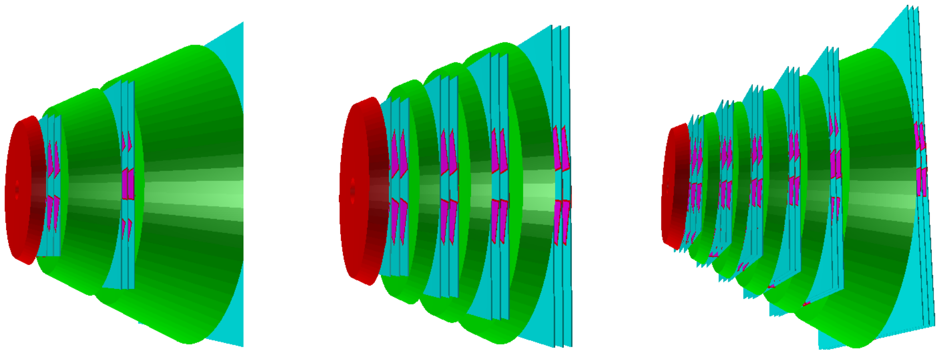

Fig. 4.4 Different geometric configuration for muon detection system. Left and middle correspond to SIS100 energies and (right) for SIS300 energies. Each detection system has carbon as the first absorber and rest is made of iron.

Table 4.3 Specifications of the various parameters for the MUCH geometries with absorber numbers 3, 4 and 6.

Specifications	**SIS100-A**	**SIS100-B**	**SIS300**
Energy ($AGeV$)	up to 8	up to 11	up to 40
No. of absorbers	3	4	6
No. of detector layers	$3 \times 3 = 9$	$4 \times 3 = 12$	$6 \times 3 = 18$
total absorber thickness (cm)	265 (60+70 +135)	265 (60+20 +20+30)	265 (40+20+20 +20+30 +35+100)
Distance between the layers (cm)	10	10	10
Distance between absorber and layer (cm)	5	5	5
Minimum no. of layers crossed by LMVM	2	3	5

for including a realistic scenario. The total active area of each layer has been divided into trapezoidal sector-shaped module. Each module is aligned on a supportive structure with thickness of 2 *cm*. The detector modules are attached with the front and back sides of support structure and filled with $Ar+CO_2$ (70% + 30%) gas mixture as an active medium with gas thickness of 3 *mm*. Cables, gas tubes, PCBs and front-end electronics are not included in the simulation. An overlap of 2 *cm* in azimuth of sensitive volume is kept along radial direction in order to avoid dead zones. The number of sectors in a particular detector plane depends on the radii of the stations and is given as

$$N_{sec} = \frac{2\pi R_{out}}{40} \tag{4.1}$$

where, R_{out} is the outer radius in *cm* and 40 *cm* is the maximum width of the trapezoidal GEM foils respectively. Fig. 4.5 shows the layout of one layer of the first station with trapezoidal sectors. In order to accommodate the electronics, cooling systems, etc., half of the total set of sectors are arranged in the front face and the rest half in the back face and its number is a tunable parameter. Actual detector set-up will include Straw tubes and TRD as indicated in

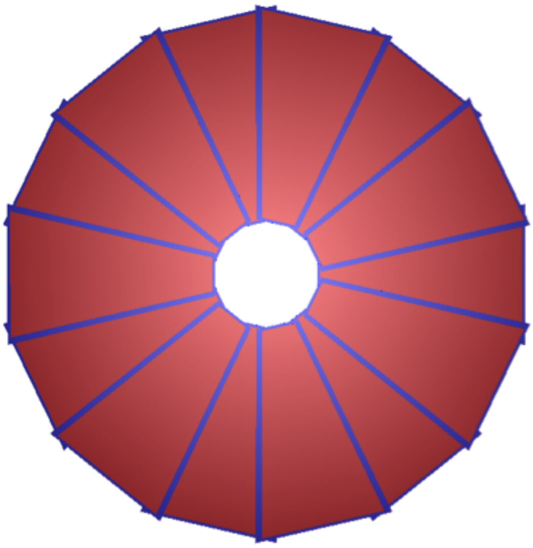

Fig. 4.5 Schematic view of the layout of the muon chambers with trapezoidal overlapping sectors.

Table 4.2 with the same realistic segmentation scheme and gas detector will be implemented.

4.3 Simulation framework and simulation procedure for MuCh

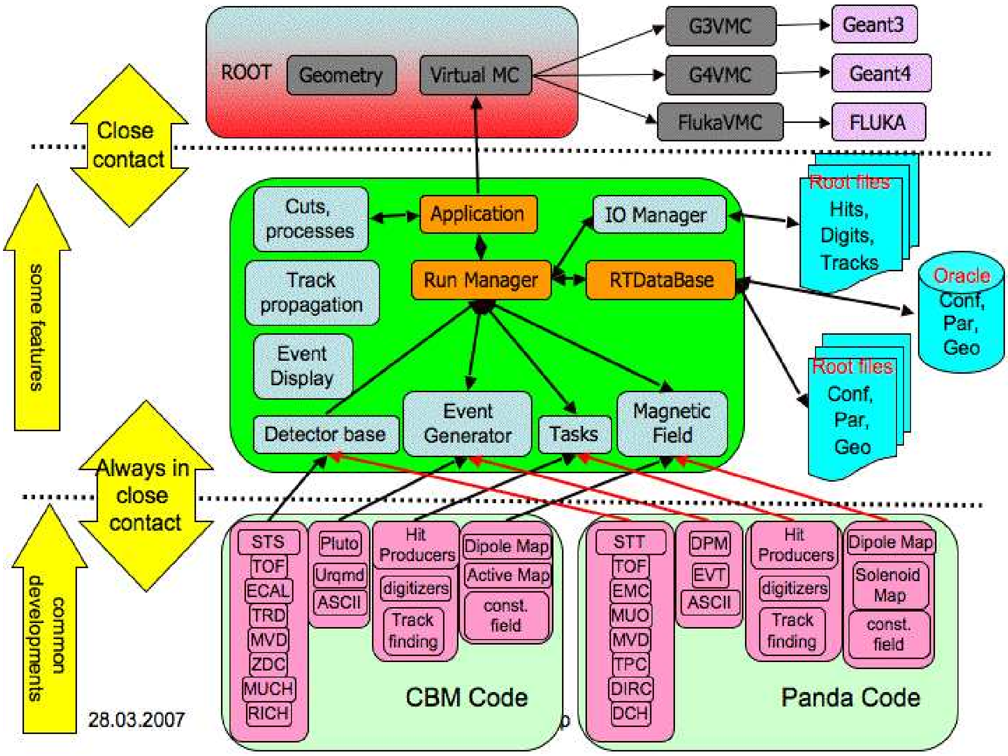

Fig. 4.6 The sketch of FairRoot simulation framework for CBM.

Simulation studies are carried out using the CBMRoot framework, which is a part of FairRoot framework. The CBMRoot is based on “Root C++ object-oriented programming” and its libraries are developed at CERN [105]. This framework supports various event generators and transport engines such as GEANT3, GEANT4 [106] or FLUKA [107] and has been developed for a feasibility study and optimization of detectors. As an event generator it uses UrQMD, PLUTO and HSD. The layout of FairRoot framework is displayed in Fig. 4.6. The flow chart in Fig. 4.7 visualizes simulation and reconstruction hierarchy and the internal data processing within CBMRoot. The simulation chain are summarized in the following fundamental blocks : a) event generation, b) geometry implementation and transport, (c) segmentation and digitization, (d) hit formation, (e) track propagation in MUCH chambers and (f) selection of tracks as muon candidates. The final identification of muon tracks is an essential part of the dimuon analysis.

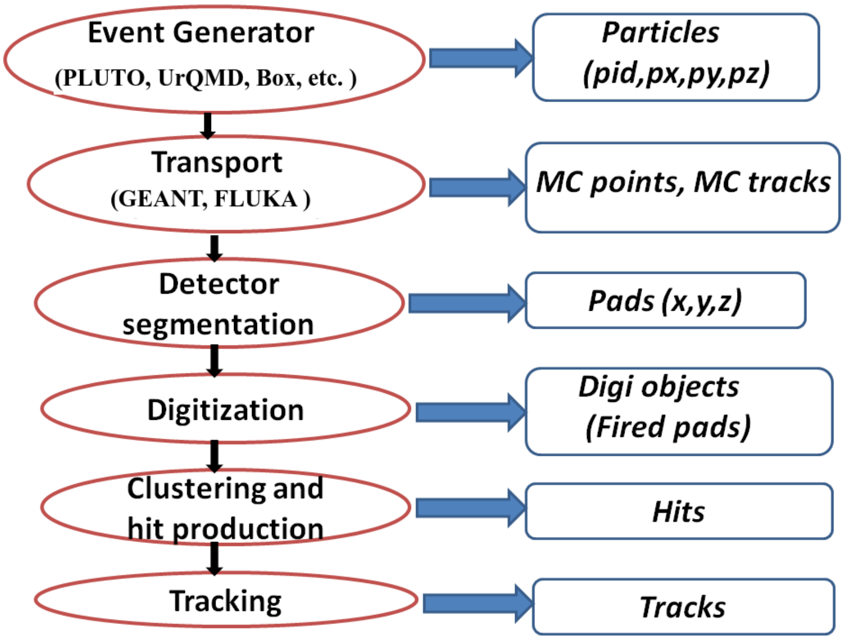

Fig. 4.7 Schematic layout of the simulation chain in MuCh [94].

4.3.1 Event generation

The first step in simulation is generation of particles projected on the detector. These particles are generated by exploiting following standard event generators

- *UrQMD* [76] is a microscopic many-body model designed to simulate ultra-relativistic p+p, p+A and A+A collisions in the energy range from SIS to RHIC energies. The model is based on covariant propagation of color strings, constituent quarks and diquarks accompanied by mesonic and baryonic degrees of freedom. Particle production is visualized to take place via fragmentation of color strings of the colliding nuclei. Towards higher energies, sub-hadronic degrees of freedom become important, which can be incorporated in UrQMD via the introduction of formation time for hadrons produced in the fragmentation of strings and by hard scattering via PYTHIA model. No phase transition from hadronic to quark-gluon state is incorporated. This model is used for generation of background. As no rare probes, such as LMVM or charmonia are included in this model, another model is used for signal particle generation.

- LMVM decays to dimuons can be generated by *PLUTO* [102] generator and the produced signal particles are embedded into the background. PLUTO generates the signal mesons by following thermal sources with thermal m_T and Gaussian rapidity distribution in the centre-of-mass frame of the collisions. The m_T distributions are generated by

$$\frac{dN}{m_T dm_T} \propto e^{-(m_T/T)} \tag{4.2}$$

where $m_T = \sqrt{p_T^2 + m_0}$ and T is the inverse slope parameter. The rapidity distributions are generated for signal particles in the centre-of-mass frame by using a Gaussian function with a zero mean (μ_y) and rapidity width σ_y as

$$\frac{dN}{dy} = e^{-y^2/2\sigma_y^2} \tag{4.3}$$

where y denotes rapidity of input signal in the centre-of-mass frame. The value of rapidity width σ_y is fixed at a particular beam energy and decreases with increasing $\sqrt{s}$. The value of σ_y as function of $\sqrt{s}$ can be calculated as

$$\sigma_y^{sig} = \sigma_y^{\pi} \times \frac{y_{max}^{sig}}{y_{max}^{pi}} \tag{4.4}$$

where

$$\sigma_y^{\pi} = \sqrt{\log(\sqrt{s}/2m_N)} \tag{4.5}$$

and m_N is the rest mass of a nucleon. The maximum value of rapidity for a particular signal particle of rest mass m_0 is

$$y_{max} = \log(\sqrt{s}/m_0) \tag{4.6}$$

The required input parameters for generation of particles by PLUTO generator in energy range of SIS100 and SIS300 are listed in Table 4.4

Table 4.4 Input parameters, T and rapidity width σ_y, for PLUTO generator for generation of LMVM and charmonia at 10 and 25 AGeV energies.

Particle	**Energy** ($AGeV$)			
	10	**25**	**10**	**25**
	T (MeV)		**rapidity width** $\sigma_{\mathbf{y}}$	
ω	115	140	0.47	0.64
ρ	115	140	0.48	0.64
η	115	140	0.57	0.74
ϕ	115	140	0.40	0.56
J/Ψ	170	170	0.10	0.23

The LMVM or charmonia (e.g., J/Ψ) decaying into muon pairs are considered in their rest frame, according to the rules of kinematics (energy and momentum conservation). Then the Lorentz transformation of produced muons momenta and space coordinates from the center-of-mass to the laboratory frame is performed.

- Another important parameter required for the calculation of signal to background ratio of LMVM and charmonia is the mean multiplicity of particle production in different energy range for the central Au+Au collisions. Information about multiplicity is not available from UrQMD or PLUTO. The multiplicity values for various signal particles can be obtained from *HSD* [108] transport code. The estimated mean multiplicities of various particles over a wide energy range in central Au+Au collisions are given in Table 4.5. The multiplicity values for minimum bias collisions can be obtained by scaling the corresponding values in central collisions by a factor 0.25 [94].

Finally, the event generator models provide information about the number of produced particles, particle identification (PID) code and four-momenta (E, p_x, p_y, p_z) of produced particles.

Table 4.5 Calculated mean multiplicities [108] of LMVM and J/Ψ for Au+Au collisions ($b = 0.5\ fm$) at different beam energies using HSD model, where b represents impact parameter.

Particle	**Energy** ($AGeV$)					
	10	**15**	**20**	**25**	**30**	**35**
η	16	23	29	33	37	40
ρ^0	9	15	19	23	25	26
ω^0	19	27	34	38	42	46
ϕ	0.12	0.50	0.83	1.28	1.24	1.50
J/Ψ	1.74×10^{-7}	2.44×10^{-6}	8.37×10^{-6}	1.92×10^{-5}	3.45×10^{-5}	5.49×10^{-5}

4.3.2 Geometry implementation and transportation

The aim of MuCh is to study propagation of tracks inside the segmented absorbers. Conical absorbers of varying sizes are, therefore, placed around the conical beam pipe for studying geometry. These conical absorbers are for accepting the forward focused particles. For effective tracking, the tracking stations consists of 3 layers of tracking chambers. Each tracking layer consists of a thin support structure and an equal number of square modules placed on the two faces of the support structure. For reducing the dead-space, modules on the two faces are placed in such a way that a border of the module on one side overlaps with an active zone of the module on the opposite side. The number of stations, their shapes, sizes and the number of modules are varied for optimization of efficiency and signal to background ratio (S/B) for detecting low-mass vector mesons and charmonia. The particles produced by the event generators are transported through the detector by GEANT3. During their passage, the particles interact with the detector gas and deposit energy inside the detector modules. The information about the energy deposition is provided by GEANT3. Their locations along with the energy deposited are called *MuCh points*. These MuCh points are stored in the *CbmMuchPoint* container along with the information about the coordinates of entrance and exit points and other information on the MC-level, like a unique track ID, active volume ID, momenta at the entrance and exit points, the time-of-flight and total track length.

4.3.3 Detector segmentation

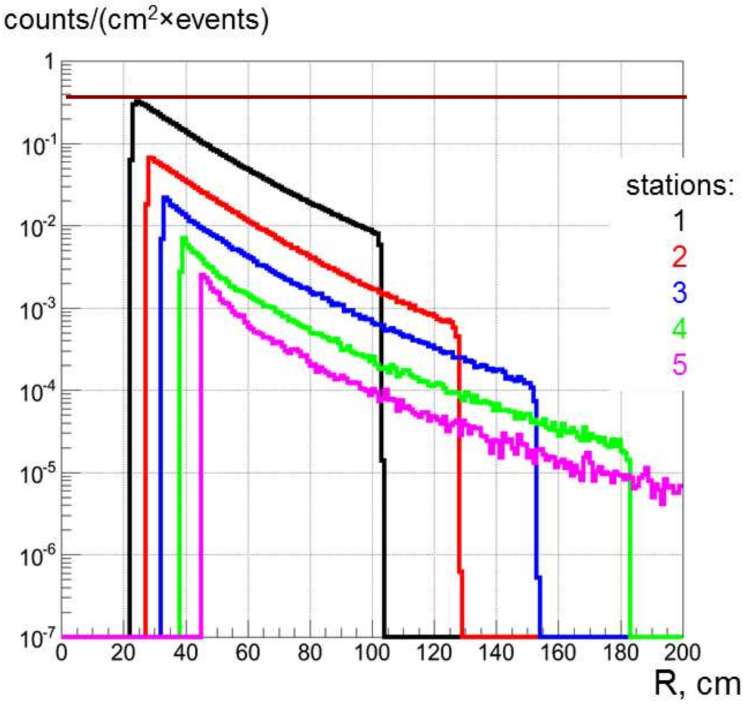

Fig. 4.8 Hit densities in the tracking chambers of stations 1 - 5 for central Au+Au collisions at 25 AGeV as calculated with the UrQMD event generator and GEANT3 transport code. Hit densities are averaged over the three layers for each gaseous chamber.

The muon detection system will be under the situations of high hit density up to 4 MHz/mm^2 and event rates $\sim$ 10 MHz. The hit densities for different stations are shown in Fig. 4.8. From the figure the maximum hit density obtained at the first station is 0.3 $cm^{-2}event^{-1}$ and hit density decreases with radial distance from the beam pipe as $\propto 1/r$. Thus, in order to account for the realistic and optimized detector geometry and variation in hit density with distance, muon detector readout planes are segmented into different annular regions with *pads* of appropriate shapes and sizes required to attain a pad occupancy of $\sim 5\%$. Another constraint for the optimization of pad size is the spatial resolution. The sector geometry divided into pads of radially increasing size is exhibited in Fig. 4.9. The dimensions of the pads are determined by the angular separation on transverse plane and its angular dimension is approximately equal to the azimuthal dimension at a given radius satisfying the condition, $\Delta r \sim r\Delta\phi$. The entire region is divided into pads of uniform or varying angular regions as exhibited in the figure. The details of segmentation study is discussed in the next chapter. As a realistic muon detection system will also contain Straw Tube and TRD, the same segmentation algorithm will be used. The segmentation of detector module into a number of pads will provide information about the required number of readout channels. In the case of Straw Tube and TRD, the number of pads will be reduced. Information about the pad coordinates, minimum and maximum pad sizes, numbers of channels and pads, and the inner and outer radii for each station averaged over three layers is supplied by *CbmMuchSegmentSector* class.

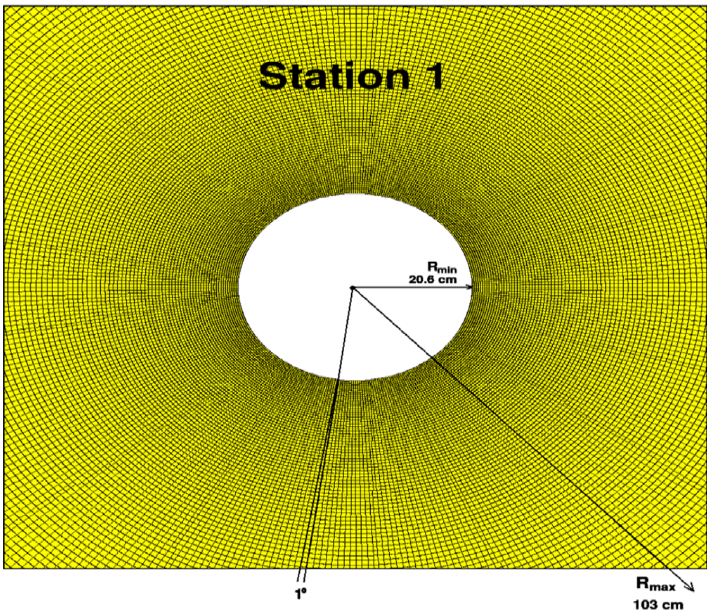

Fig. 4.9 Schematic view of segmentation of the readout plane of a layer of the first station of MuCh. The entire area has been divided into pads of 1° angular region with 360 lines.

4.3.4 Digitization

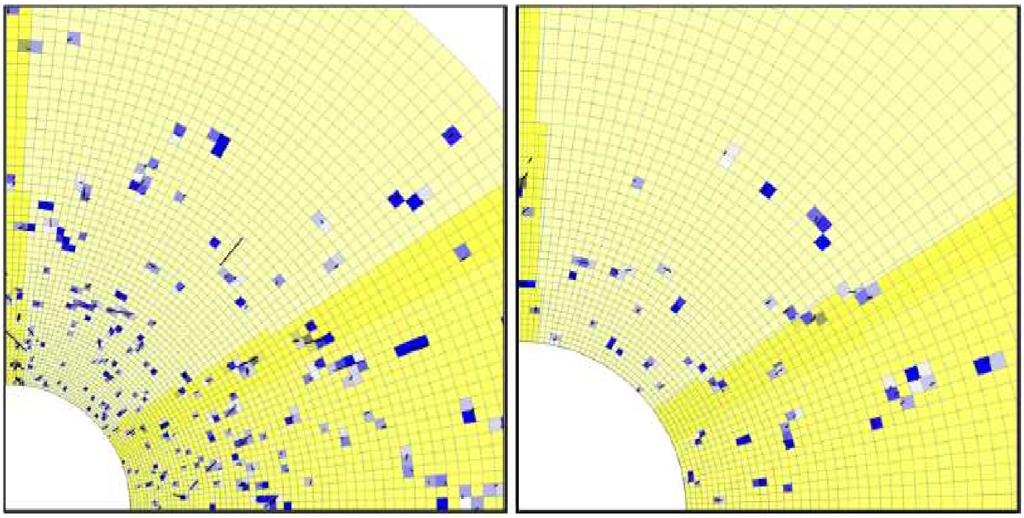

Fig. 4.10 Illustration of digitization scheme for the first two stations.

The procedure of distributing MuCh points to pads is termed as *Digitization*. Digitization involves a detailed procedure of implementing GEM detector response to the deposited energy inside the tracking chambers as shown in Fig. 4.10. The digitization is based on a simple assumption that a GEM active gas volume can be split into drift and avalanche regions as displayed in Fig. 4.11. No triple-GEM structure is implemented in the simulation. The task of MuCh digitization is performed by *CbmMuchDigitize* class, which takes MuCh points array as input and produce an array of type *CbmMuchDigi* as output. The digitization algorithm for producing digi output are :

(a) simple digitization scheme and

(b) advance digitization scheme.

In the simple digitization scheme every pad located under the centre of a track is fired and are added together to form digits. This simple digitization scheme is implemented. The algorithm of simple digitization is implemented in class *CbmMuchDigitizeGem* by switching on the condition as described below :

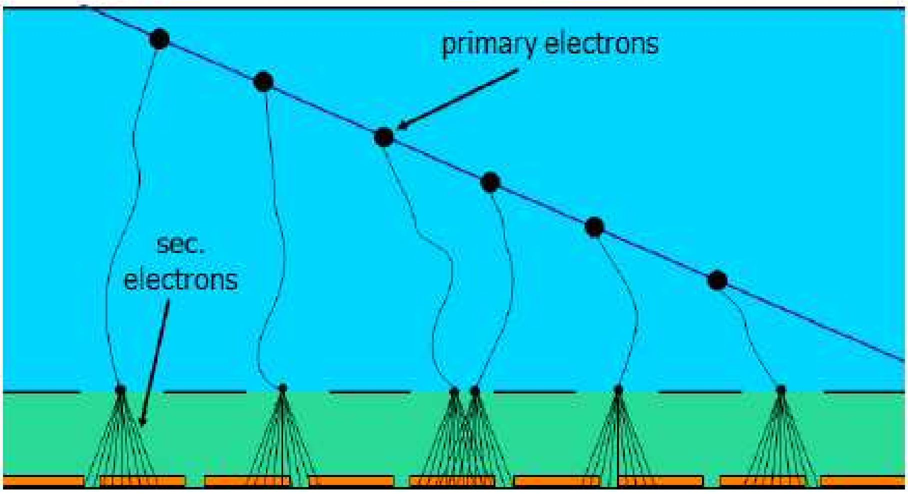

Fig. 4.11 Schematic representation of signal generation in GEM detector.

```
CbmMuchDigitizeGem * digitize = new CbmMuchDigitizeGem(muchDigiFile.Data());
if (muchHitProducerType = "simple")
digitize → SetAlgorithm(0);
else if (muchHitProducerType = "advanced")
digitize → SetAlgorithm(1);
```

In the advanced digitization scheme, a single track can fire several pads on proper inclination. Fig. 4.12 illustrates the two implemented digitization algorithm. The digitization algorithm can be divided into the following steps:

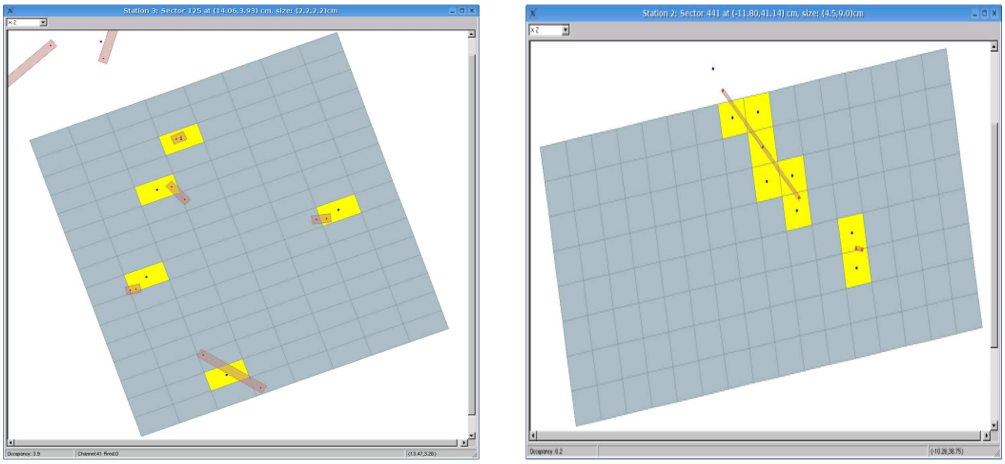

Fig. 4.12 Illustration of different digitization schemes implemented to produce Digits. [left panel] displays a simple digitization scheme while [right panel] displays the advanced digitization scheme.

- Determination of the number of primary electrons emitted in the drift volume for each MC point is based on the Landau distribution for Ar(70%)+CO_2(30%) gas mixture, track length in the drift volume, and particle type and energy. Information about expectation value and variance for the Landau distribution are determined with HEED [109] package. Produced primary electrons are distributed randomly according to the Poisson law along the direction of the incident track.

- These primary electrons then interact with gaseous medium and avalanche of secondary electrons are produced in the avalanche region shown in Fig. 4.11; the number of emitted secondary electrons are then determined. Exponential gas gain distribution with a mean gas gain of 10^4 is used. The transversal diffusion of avalanche measures the spot size, which is constant.

- The intersection of secondary electron spots with pad structure and the charge arrived at each pad are determined. The default value of the spot radius is set to 600 μm as calculated for the triple-GEM detectors using the information from the beam tests. The arrival time of charge is calculated from the MC point time plus the primary electron drift time $t = d/v$, where d is distance covered by the primary electrons towards avalanche region and v is the drift velocity with default value of $v = 100\ \mu m/ns$.

- The time-dependent summation of charges from all MC points taken from pad-by-pad is performed and the charge-vs-time distribution is converted into timing response of the envisaged MuCh readout electronics. The timing response of the δ-function like charge is simulated by the linear peaking period of 20 ns and the falling edge is described by exponential function with 40 ns slope. Response to several δ-functions like charge signals is described as a convolution in time of responses from several δ-functions. Random noise of the readout electronics of the order of $2e^-$ is also added at this step.

- The threshold charge to readout response is applied and the time stamp (a moment when the response exceeds the threshold value) is determined. The charge information is converted into ADC channels with one of the three methods : amplitude with the flash discriminator, Wilkinson integration or time-over-threshold approach.

- This information regarding the time stamp and ADC is then decoded into 32-bit word and is stored in the array of CbmMuchDigi objects together with the 32-bit channel Id for subsequent processing.

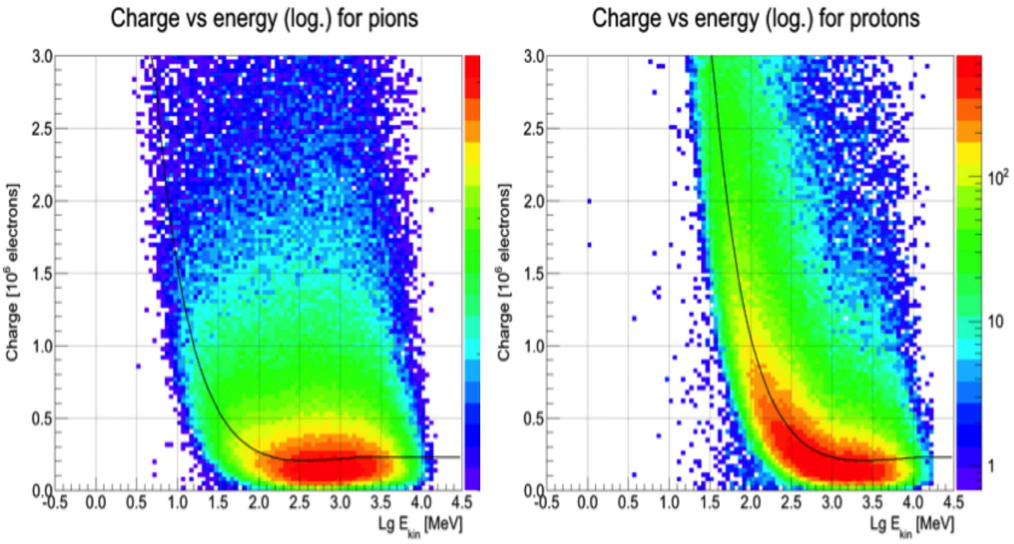

Fig. 4.13 Deposited charge versus particle energy for pions and protons in Au+Au collisions at 25 AGeV inside the active volume of the detector with drift gap of 3 mm. (a) for pions and (b) for protons. The black curves result from a Bethe-Bloch fit to the mean values.

Fig. 4.10 illustrates the results obtained with the digitization algorithm showing the reconstructed charge on pads corresponding to projections of MC track. Apart from visual control of the fired pad to corresponding MC track, the quality assurance algorithm has been implemented in the class *CbmMuchHitFinderQa*. One of the quality condition is the full charge distribution of track as function of energy and particle type as shown in Fig. 4.13. This distribution agrees well with the Bethe-Bloch dependence of the most-probable value of mean gas gain, described by black curve. The electrons interact with the gas medium and lose energy by Bethe-Bloch mechanism as displayed in the figure. The charge deposited by the minimum ionizing particles is shown in Fig. 4.14, which follows Landau distribution.

The parameters of the detector are tunable and the values depend on the implemented micro-pattern detector technology. The value for spot radius is chosen such that the existing experimental data can be reproduced from them. The avalanche spot for the primary electrons is projected on the pad plane and the sum of charges at each pad is calculated. Other tunable parameters are : (i) total number of ADC channels, (ii) the maximum charge deposited on the pads and (iii) the threshold charge. The maximum charge defines the dynamic range of the readout ASIC. If the deposited energy for a particular channel exceeds the dynamic range, the channel gets saturated. The threshold charge is set above the expected noise level. In the present study, these parameters are set to have the following values : (i) number of ADC channels = 256, (ii) $Q_{max} = 80\ fc$, (iii) $Q_{th} = 1.0\ fc$ and (iv) GEM spot radius = 600 μm. Inside the Ar+CO_2 gas mixture filled gas volume the Minimum Ionizing Particles like muons can produce 100 - 120 primary $electrons/cm$. For 3 mm drift gap the number of primary electrons produced would, therefore, be $\approx$ 30 - 40, with 3×10^4 total number of electrons produced for average gas gain of 10^4 and

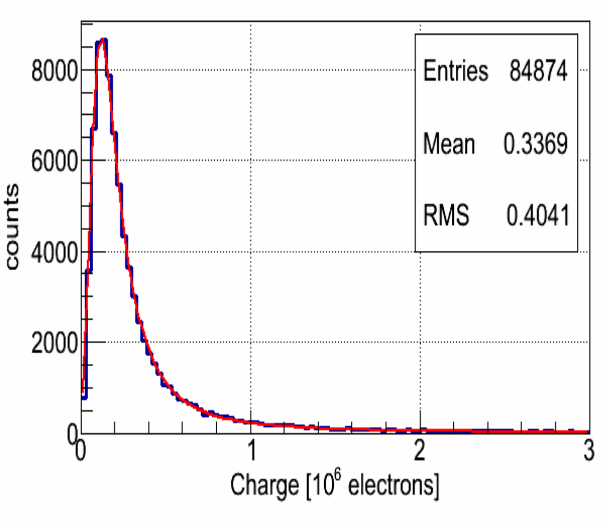

Fig. 4.14 Charge deposition by a minimum ionization particle (MIP) in the gas volume of the detector. The mean gas gain 10^4 is used in the simulation. 33 primary electrons are created by MIP along the track direction with drift gap of 3 mm.

is equivalent to 45 fc of deposited charge. Hence, the $Q_{th} = 1\ fc$ would not significantly affect the signal.

4.3.5 Clustering and hit formation

The *digits* obtained after digitization are clubbed together to form clusters. These clusters are then deconvoluted into *hits*. Three types of clustering algorithm are implemented in the class *CbmMuchFindHitsGem*, which incorporates array of digits as input and produces array of hits as output. Three algorithm are implemented for clustering, cluster deconvolution and hit finding

- **One hit per pad** is a trivial algorithm in which a hit is created for each fired pad. The positions of the hits correspond to pad centres, while the hit uncertainties are taken as pad's dimensions divided by $\sqrt{12}$. One of the prime advantages of this algorithm is the simplicity of implementation and low CPU consumption, while the main disadvantage is that a larger number of hits are created far away from real track positions. This leads to huge combinatorial background and inefficiency at the level of track finding.

- **One hit per cluster** is, also called simple hit finder algorithm. The coordinates of the hits are measured by taking average of the centre-of-gravity with weights equal to the charges induced on the pads. Advantage of this algorithm is that it is simple and faster and also provides better track position than in the previous case. However, for larger clusters, this algorithm causes mismatch between reconstructed hit positions and real track coordinates.

- **Search for local maxima** in the charge distribution is done cluster-by-cluster, also called advance hit finder algorithm. The hit coordinates are assigned to centers of pads, which correspond to local maxima. If the cluster has less than 2 hits per pads, method of one hit per cluster algorithm is implemented for determination of hit coordinates for small clusters with a better accuracy. The main advantage of this method is that it provides better results in larger clusters and allows to find several single track hits that contribute to one cluster. Nevertheless, for large clusters local maxima may originate from random fluctuations of charge on pads which lead to fake hits. Disadvantage is that some tracks still remain unresolved by this algorithm.

The pictorial form of these algorithms is shown in Fig. 4.15, which illustrates that track positions are reconstructed properly in majority of cases. By default, the "search for local maxima or advance hit finder" algorithm is used in the MuCh simulations. The developed algorithms for the cluster and hit findings can be used not only for simulation purposes, but also for the reconstruction of the real data.

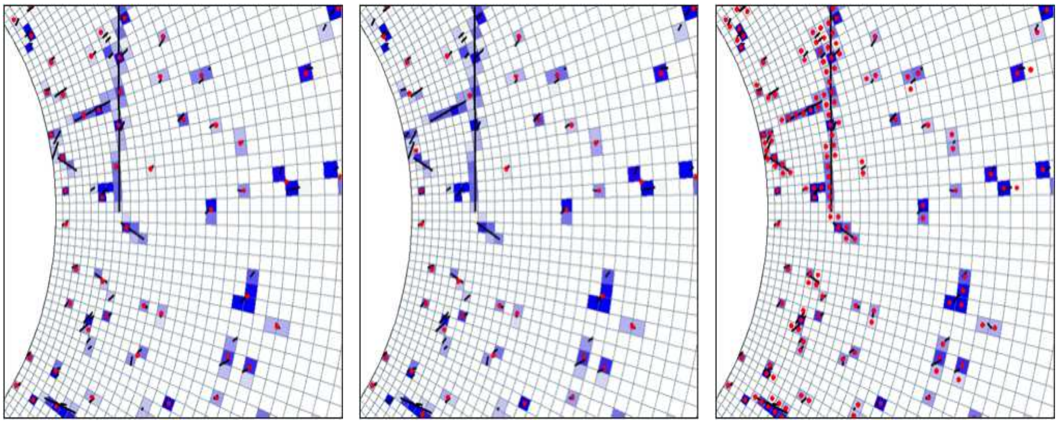

Fig. 4.15 Illustration of hit-finder algorithm in a central Au+Au collision at 25 AGeV.

4.3.6 Track reconstruction

One of the technical challenges of track identification in the CBM-MuCh detector is due to large multiplicities in relativistic heavy-ion collisions. Up to 1000 charged particles per events are envisaged to be produced in a central Au+Au collisions at FAIR energies. This high charged particle multiplicity leads to high track and hit densities in the MuCh detector, in particular at the first station of MuCh as displayed in Fig. 4.16. The track reconstruction algorithm includes tracks from MuCh and extend up to STS. The STS track reconstruction is based on the *cellular automaton* method [110] and STS track

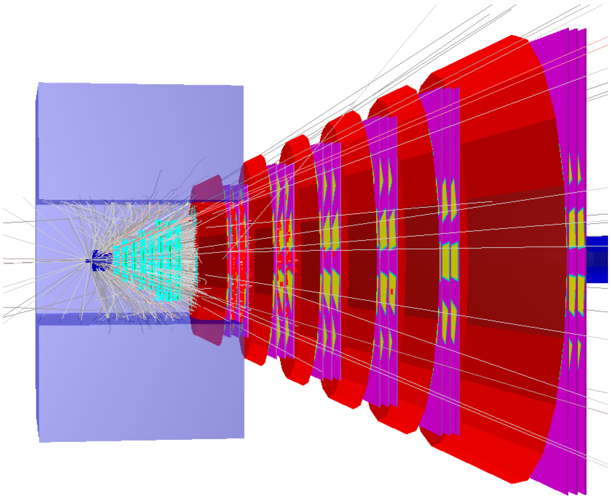

Fig. 4.16 Visualization of tracking for one simulated central Au+Au collision at 25 AGeV.

parameters are taken as the origin for successive track prolongation. The track following is based on the standard *Kalman Filter* technique [111] and is used for the determination of track parameters [112] and trajectory identification. The track reconstruction includes track propagation, track finding, track fitting and finally selection of the true track.

4.3.6.1 Track propagation

The track propagation algorithms estimates the trajectory and its errors in a covariance matrix. This method exploits three physics processes, which mainly influence the trajectory and these are energy loss, multiple scattering and effect of magnetic field. The effect of material on the track momentum is taken into account by measuring the expected energy loss due to ionization, Bethe-Bloch formula and bremsstrahlung, Bethe-Heitler formula [113]. Addition to noise in the track propagation includes their effect on error, that is the covariance matrix due to multiple scattering. A Gaussian approximation employing Highland formula [113] is used for calculating the average scattering angle. The reconstructed trajectory is propagated according to the equation of motion of the charged particle in a magnetic field. In the presence of magnetic field these equations of motion for a charged particle is solved by 4^{th} Runge-Kutta method [114]. Moreover, passage of a charged particle through field-free region exploits straight line for propagation and the transport matrix calculation. The transport matrix is calculated by integration of derivatives along the so-called zero trajectory [115]. A detailed description of the developed track propagation can be found in [116].

4.3.6.2 Track finding and track fitting

In the track finding algorithm hits are attached to the propagated track at each detector station using two different methods, *nearest-neighbour* (nn) and *branching* method. In the 'nn' method, just the nearest hit is attached to the track. However, in the branching method, all the hits within a certain environment are included. In the 'nn' method, only one track is further propagated, whereas the branching method allows several track branches to be followed, one for each attached hit. Common techniques to these methods are the above described track following, the Kalman-Filter and the calculation of the validation region for hits.

Assignment of new hits is done step by step at each detector station. After the track propagation to the next station possible hits are attached and track parameters are updated by Kalman-Filter. For the attachment of hits, a validation gate is calculated in order to allow for a high degree of confidence in the hit-to-track assignment. The validation gate is defined based on the residual vector r (distance between the fitted track and the hit) and the residual covariance matrix R. According to Kalman-based tracking filters, a validation gate can be expressed as $\mathrm{v} = rR^{-1}r^T < \mathrm{d}$. The cut value of 'd' is chosen such that a defined probability of rejecting the correct hit is achieved. Here this probability is chosen to be 0.001. Value of 'd' can be taken from χ^2 tables on the dependence on the number of effective degrees of freedom. Here the effective degree of freedom is 1 for a Straw Tube detector hits and 2 for hits from pads in a GEM detector. The algorithm takes into account missing hits due to detector inefficiencies, dead zones in the detector, inefficiency of hit finder algorithm, etc.

Two methods which can be chosen for hit assignment to tracks differ in the way how a situation is dealt with in which several hits lie within the validation gate. In case of the branching method, a new track branch is created for each hit lying within the validation gate. Since the number of branches can grow exponentially, the value of χ^2 is calculated for each track branch and unlikely ones are rejected. Also, for each input track seeds number of created branches is calculated and if it exceeds the limit then the tracking continues using 'nn' approach. For the second method, no track branches are created. The 'nn' method attaches the hit with the smallest v, if lying in the validation region.

4.3.6.3 Track selection

After the track finding, the selection of track is done. This routine is based on the rejection of clone and ghost tracks and keeping the correctly found track with high efficiency. If two tracks consist of similar set of hits, i.e., the track is essentially found twice, are called clone tracks. Moreover, tracks consisting of random set of hits are called ghost tracks. Selection criteria involves sorting of tracks by their qualities defined by track length and χ^2, starting with the highest quality tracks and checking all the hits associated with the tracks. Particularly, the number of hits shared with other tracks is calculated and track is rejected if 15% of hits are shared. For the reconstruction of tracks in MuCh, the primary vertex determination is done by the associated STS track.

4.3.7 Performance of track reconstruction at MuCh

In order to test the performance of tracking algorithm, central Au+Au collisions at 25 *AGeV* were simulated with UrQMD [76]. These events were used to estimate the background in which the signal of interest, i.e., muons from the primary vertex were embedded. For enhancing statistics, 5 primary μ^+ and μ^- each were embedded in each UrQMD event using SIS300 detector set-up. The hits are calculated from MC information as input. For efficiency calculations, the level of correspondence between the found and simulated tracks is estimated. A track is defined to be correctly found if it has more than 70% of hits from one MC track, otherwise it is taken as ghost track. The track reconstruction efficiency is defined as

$$\epsilon_{track} = \frac{N_{reco}}{N_{acc}} \tag{4.7}$$

where, N_{reco} corresponds to the number of correctly found tracks after reconstruction and N_{acc} is the number of reconstructable tracks in the MuCh acceptance, i.e., tracks that have at least 6 detected hits in the MuCh. Results shown are for muon tracks since these are the most important ones for muon simulations. Fig. 4.17 exhibits the track reconstruction efficiency as a function of momentum for MuCh and global tracking efficiency for STS + MuCh for 25 $AGeV$ beam energy. The MuCh track reconstruction efficiency integrated over the momentum range 0 - 10 GeV/c is 95.9% for 'nn' method and 95.8% for the branching method. The mean efficiency for the tracking in STS + MuCh is 95.1% for the 'nn' and 94.9% for the branching method. Both the methods yield almost the same efficiency but the 'nn' approach is easier to

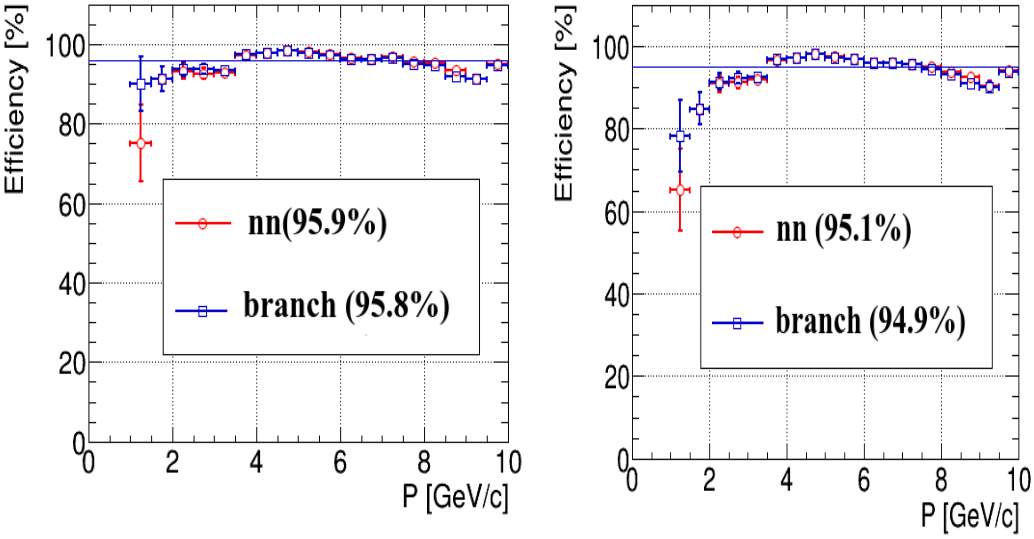

Fig. 4.17 Track reconstruction efficiency for the primary muon tracks from J/Ψ as a function of momentum for two tracking algorithms: nearest-neighbour, nn, (red) and branching, branch, (blue). The plot on the left shows MuCh tracking efficiency, the plot on the right exhibits STS + MuCh tracking efficiency. Horizontal lines represent numbers integrated over momentum.

implement and is also faster. This method was used by default in the event reconstruction.

4.3.8 Identification of muons

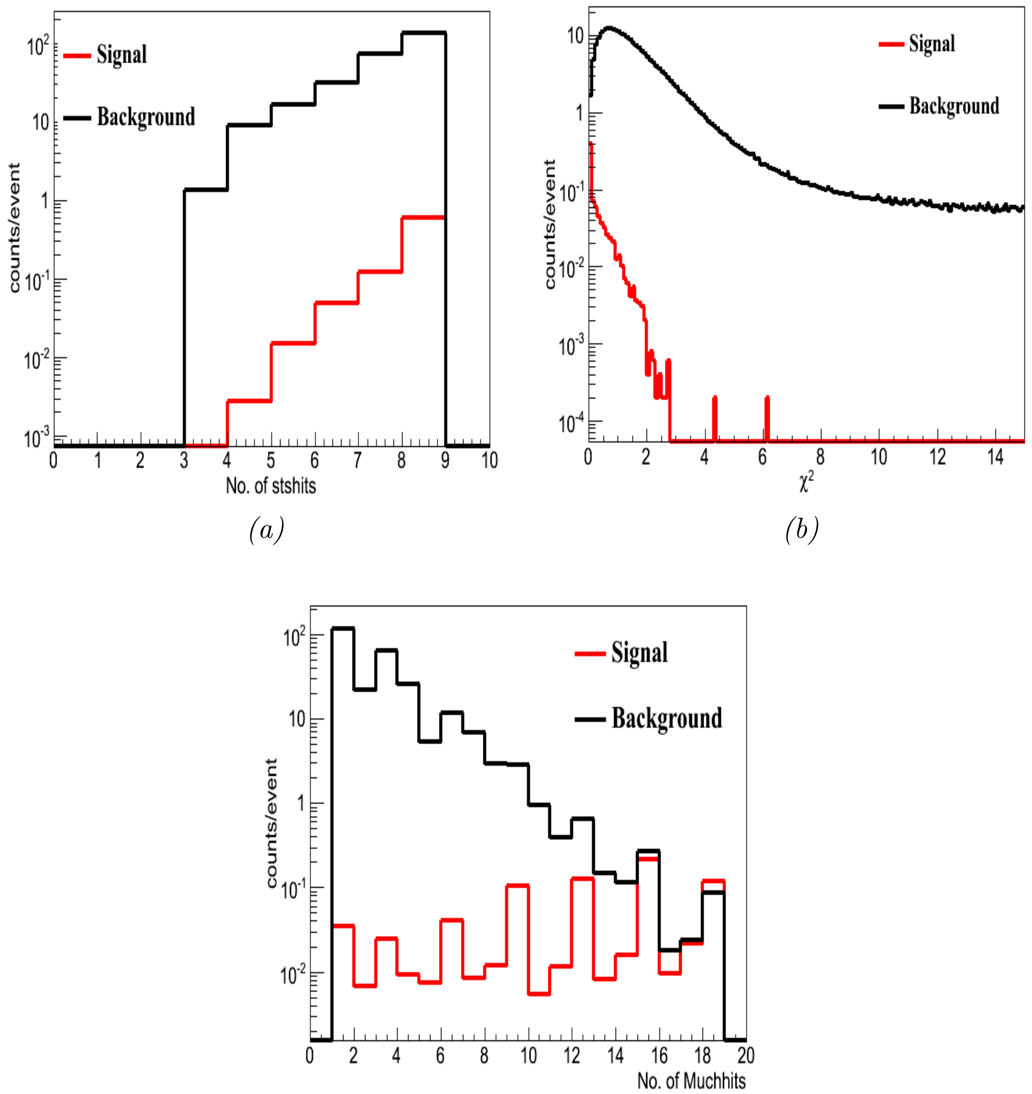

(a) (b)

(c)

Fig. 4.18 Various parameter values extracted for signal ω^0 and background, central Au+Au collisions at 25 AGeV. (a) shows number of STS hits (layers), (b) displays χ^2 of primary vertex and (c) exhibits number of MuCh hits (layers).

From the global reconstructed tracks, certain set of cuts at the analysis level are applied to identify muons. This is done to reduce the background contributed by non-muonic tracks and secondary muons which arise from the weak decays of pions and kaons. The applied cuts for the selection of muon candidates are : (a) number of hits in STS, (b) number of hits in MUCH layers, (c) χ^2 (= χ^2/n.d.f of MuCh tracks) of MuCh track segment and (d) χ^2_{vertex} (=χ^2_{vertex}/n.d.f of primary vertex), where n.d.f is number of degree of freedom. In Fig. 4.18 the distributions of these parameters for ω^0 signal and background are displayed as simulated for the PLUTO and UrQMD events at 25 $AGeV$. The left panel in Fig. 4.18 illustrates the distribution of the number of STS layers, the right panel depicts the χ^2 distribution and in the the lower panel the variation of the number of MuCh layers are shown for the signal and background. Based on the separation powers of these cuts to discriminate between signal and background, we obtained a set of final cuts that have been used in this analysis for the selection of muon candidates. It should be noted that for the selection of muons from LMVM and charmonia, the numbers of MuCh hits in a track are taken to be different. Muons coming from the decays of J/Ψ are relatively harder and thus are expected to cross the full absorber and reach the last station (trigger station). For selecting track candidates for J/Ψ, the tracks should have at least 16 MuCh hits for SIS300 set-up and 12 hits for SIS100 set-up. However, the muons coming from the decays of LMVM are much softer, they are, therefore, expected to stop inside the last 100 cm thick iron block. Hence, for them the required number of MuCh hits does not exceed 15 for SIS300 set-up and 11 for SIS100 set-up.

Several tests have been performed using the MC data for the evaluation of the performance of MuCh. One of these is the test of the survival of primary (signal) and secondary (background) particles with the variation of the cut parameters as already discussed. Since UrQMD contributes only to the background, thus the decay muons are present only in the secondary data samples. Application of STS hits ≥ 7 and $\chi^2 \leq 2$ will remove most of the pions and other particles without removing muons significantly. The cuts used, therefore, works as the effect of absorber in addition to acceptance and track finding.

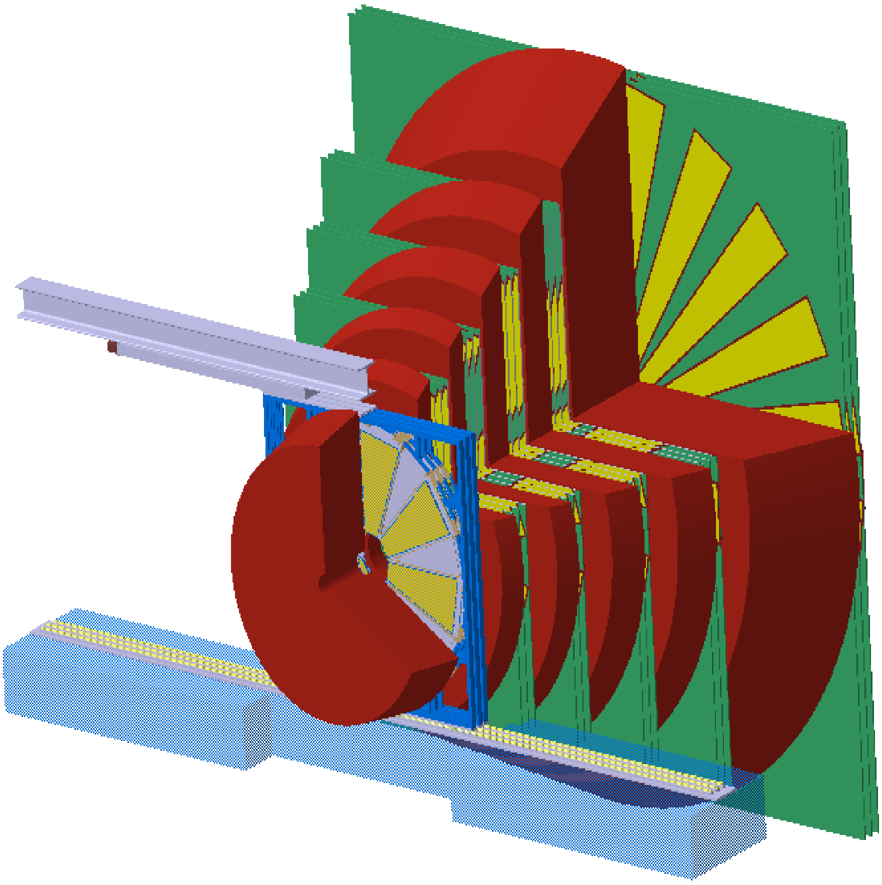

Performance Study and Segmentation Optimization of MuCh

Chapter 5

Performance Study and Segmentation Optimization of MuCh

Optimization of the geometry for the muon detection system of the CBM experiment has already been discussed in detail in Chapter 4; the details about the simulation studies are also presented. The tracking chambers used in carrying out simulation are based on GEM technology. The detector module is divided into small segments called pads. This chapter starts with a brief description of the simulation procedure, followed by a performance study for ω^0 meson detection at SIS100 set-up. Importance of segmentation of the detector chambers into pads is stressed and the results on the optimization of pad sizes are also presented in this chapter.

5.1 Simulation procedure

Simulation for the segmentation optimization for the MuCh set-up is performed within the *CBMRoot Framework*, which allows full event simulation and reconstruction. In addition to *CBMRoot Framework*, event generators, PLUTO and UrQMD, are used for generating signal and background. The produced particles are transported through the detector set-up **(STS + MuCh + TOF)** by GEANT3.

5.1.1 Input for simulation study

One million ω^0 ($\rightarrow \mu^+\mu^-$) meson events as signal, generated by **PLUTO** [102], are embedded into the background (without embedding) generated by **UrQMD** [76] for the central ($b = 0.0\ fm$) Au+Au collisions at $E_{Lab} = 8$ $AGeV$ as input, where b represents impact parameter. PLUTO generates phase-space distribution and decays of LMVM and charmonia. The values of the parameters required by PLUTO for generating ω^0 mesons at $E_{Lab} = 8$ $AGeV$ and corresponding signal multiplicities obtained from HSD model [108] and branching ratio for dimuon channel ($\omega^0 \rightarrow \mu^+\mu^-$) [117], needed for the estimation of signal to background ratio, are listed in Table 5.1.

Table 5.1 Values of the parameters required by PLUTO, T and σ_y, for generating ω^0 mesons and, its multiplicity and BR for estimating signal to background ratio.

Parameter	E_{Lab} **= 8** $AGeV$ **(SIS100)**
Temperature (MeV)	115
σ_y	0.41
Multiplicity	19
Branching ratio (BR)	$(9 \pm 3) \times 10^{-5}$ %

Fig. 5.1 exhibits the invariant mass distribution for ω^0 ($\rightarrow \mu^+\mu^-$) decays at 8 $AGeV$. Fig. 5.2 shows the distributions of various observables such as transverse momentum (p_T), momentum (p), rapidity (y) and y-p_T plot at E_{Lab} = 8 $AGeV$ for ω^0 ($\rightarrow \mu^+\mu^-$) meson input. The ω^0 decays into muon pairs and distributions of these observables for single muons are exhibited in Fig. 5.3 for the same energy.

5.1.2 Detector geometry

Generated particles are transported through the detector set-up consisting of STS + MuCh + TOF systems by using GEANT3. The STS geometry consists of 8 stations located at distances of 30, 40, 50, 60, 70, 80, 90 and 100 cm from the target made up of 250 μm thick gold target and is mounted inside the dipole magnet. The STS is used for tracking charged particles and determining

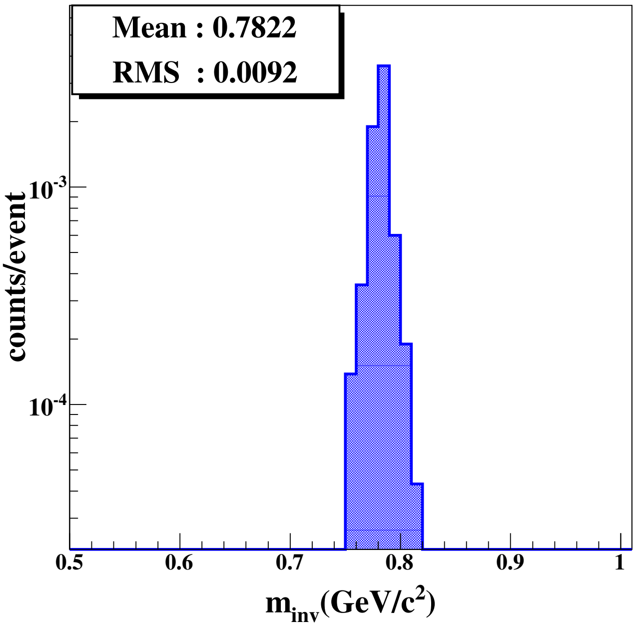

Fig. 5.1 Invariant mass distribution for $\omega^0(\rightarrow \mu^+\mu^-)$ *mesons generated by PLUTO at* E_{Lab} = *8 AGeV.*

their momenta. The charged particle tracks are then propagated through the absorber segments and MuCh tracking chambers. The configuration of MuCh set-up used in the analysis is SIS100 mode, which consists of 4 absorber layer and 12 (4 × 3) tracking chambers. Tracking chambers are based on GEM technology and the GEM detectors have an acceptance of 5 - 25°. Segmented shielding with lead as shielding material for the first absorber and iron for the rest is used for reducing the background due to secondary electrons. No shielding is present in the detector layer region as discernible in the right panel of Fig. 5.4 [94]. The muon detection system is followed by TOF detector for further suppression of background and is placed at a distance of ∼ 650 *cm* for SIS100 set-up. Fig. 5.4 shows a sketch of SIS100 configuration.

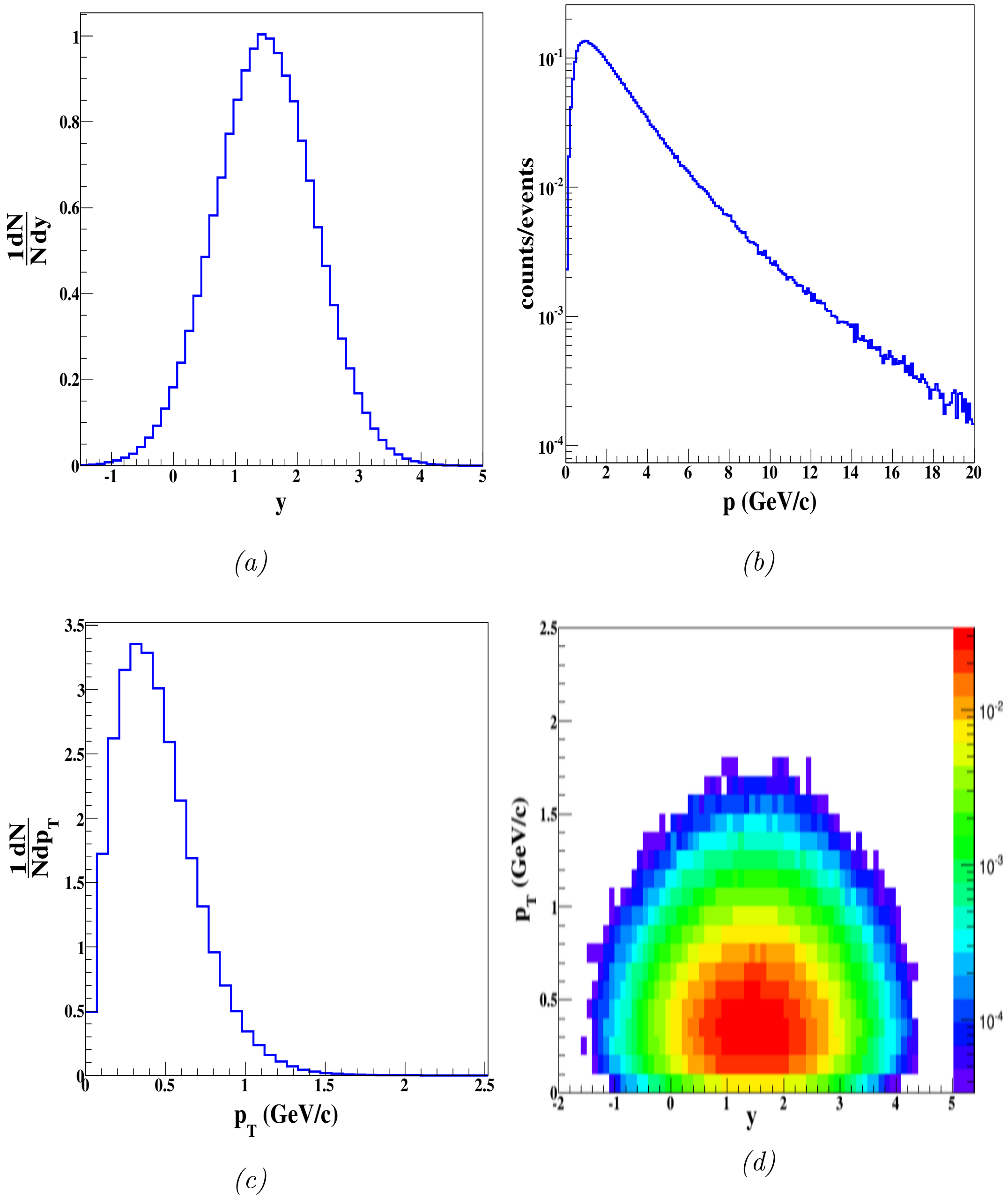

(a) *(b)*

(c) *(d)*

Fig. 5.2 Distributions of various observables for input ω^0 mesons decaying into $\mu^+\mu^-$ pairs at 8 AGeV (SIS100) generated from PLUTO : (a) distribution of rapidity, (b) momentum distribution, (c) p_T distribution and (d) acceptance (or y-p_T)plot for dimuon pairs produced via decays of ω^0 mesons.

5.2 Feasibility study for MuCh

One of the main aims of simulation study is to investigate the performance of the MuCh system for detecting LMVM reconstruction by utilizing the real

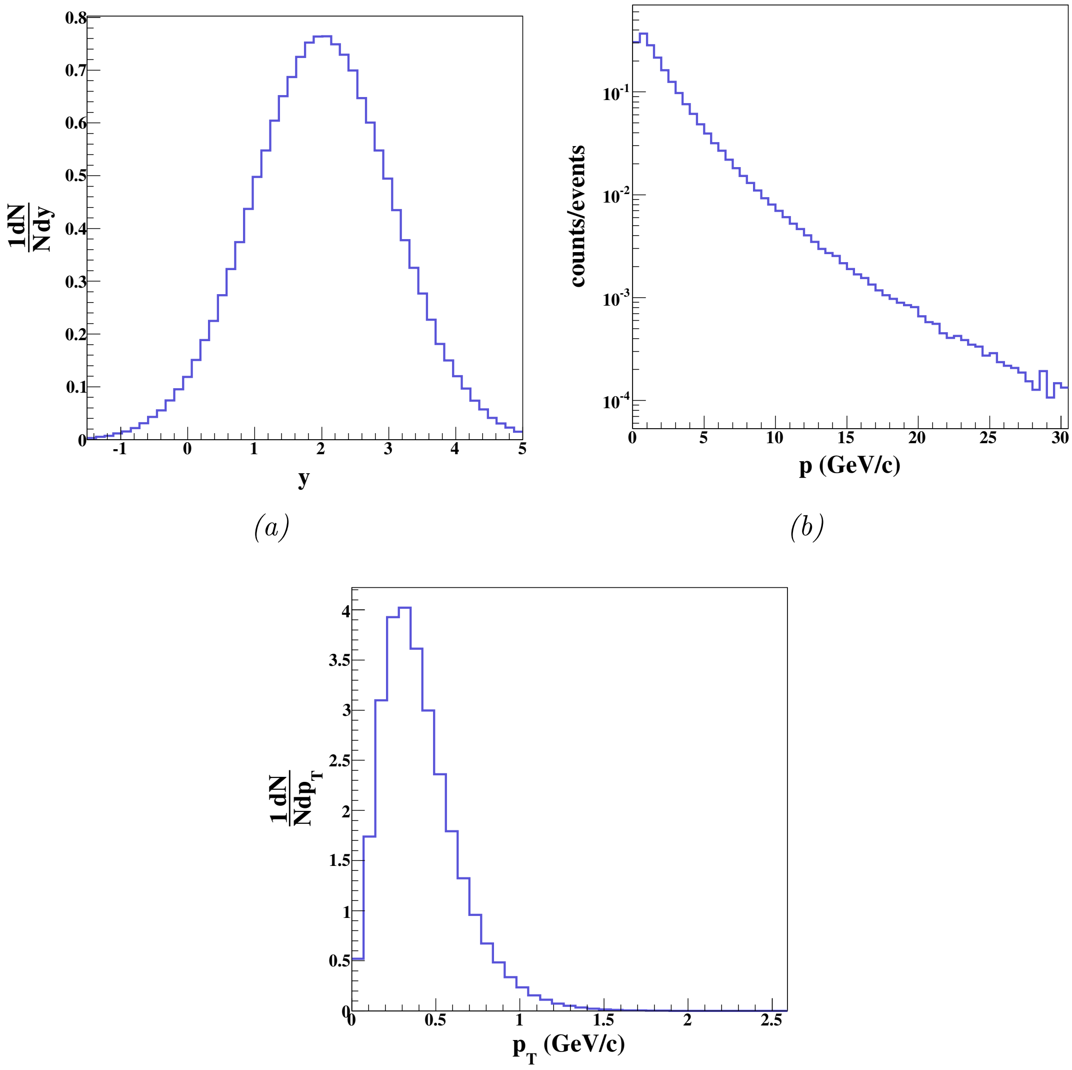

(a) *(b)*

(c)

Fig. 5.3 Distributions of various variables for single muons created by decay of input ω^0 mesons at 8 AGeV (SIS100) generated from PLUTO : (a) distribution of rapidity, (b) momentum distribution and (c) transverse momentum distribution.

detector set-up. The study is focused for measuring ω^0 mesons via their decays into $\mu^+\mu^-$ pairs. The simulations were performed for the central Au+Au collisions at 8 $AGeV$. Since the maximum number of particles are produced in the central collisions, therefore, chosen for feasibility study.

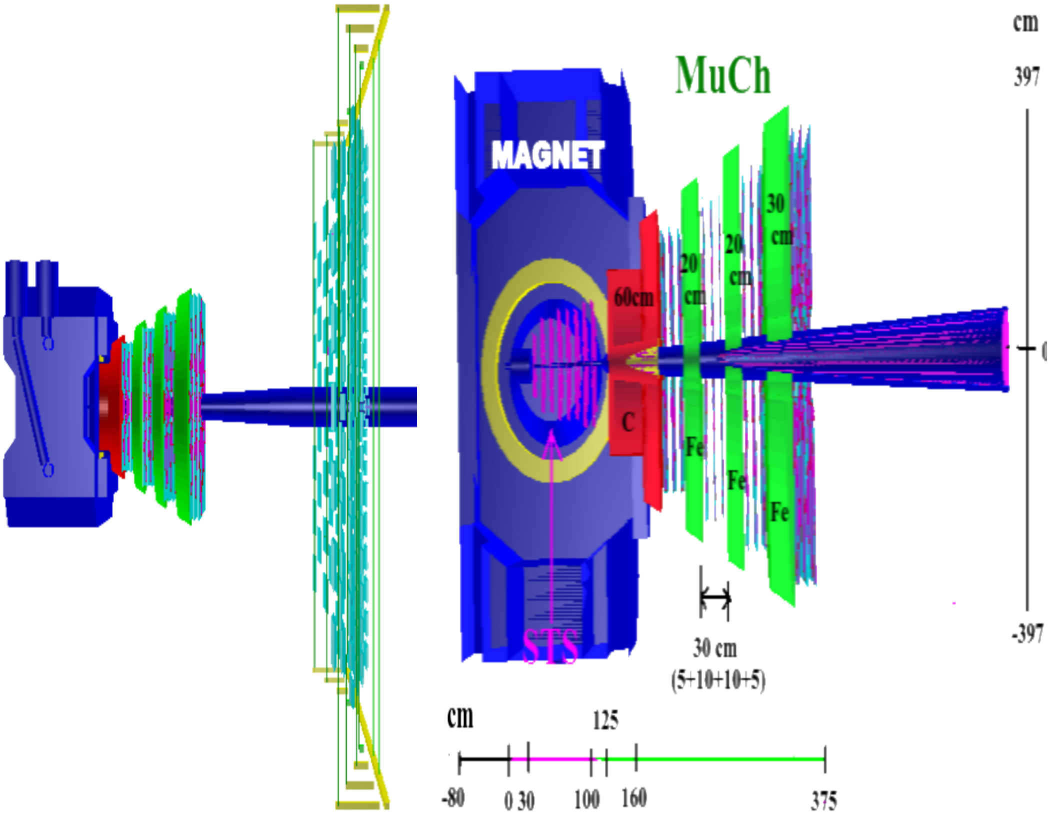

(a) (b)

Fig. 5.4 A schematic view of MuCh SIS100 detector with TOF system : (a) sketch of SIS100 with 12 detector layers and 4 absorbers and (b) complete layout of the SIS100 set-up.

5.2.1 Invariant mass distribution for signal ($\omega^0 \rightarrow \mu^+\mu^-$) and background

The generated particles after their passage through the detector set-up are reconstructed. Reconstructions are performed both in the STS and MuCh detectors. The reconstructed tracks are then utilized further for analysis, which involves reconstruction of invariant mass both for signal and background. The invariant mass calculation for ω^0 ($\rightarrow \mu^+\mu^-$) is done on event-by-event basis in which four-momenta of μ^+ and μ^- produced in the same event are combined as

$$m_{inv(\omega^0)} = P_{\mu^+} + P_{\mu^-} \tag{5.1}$$

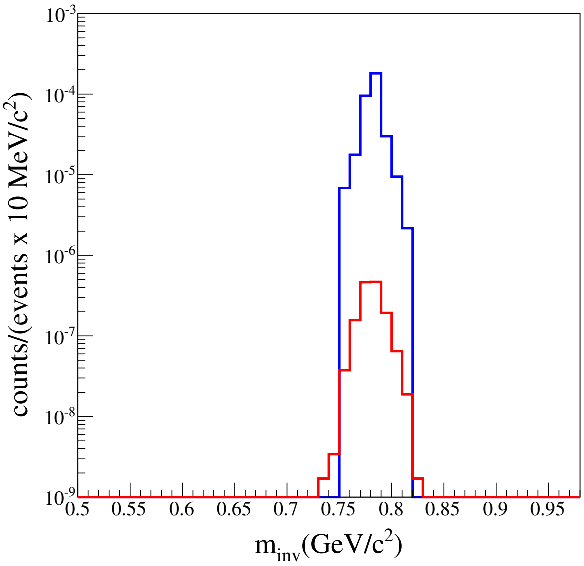

Fig. 5.5 Invariant mass distribution of reconstructed ω^0 mesons (red curve) for SIS100 set-up at 8 AGeV superposed with its input (blue curve).

where P_{μ^+} and P_{μ^-} are the four-momenta of μ^+ and μ^-. Fig. 5.5 exhibits the invariant mass distribution of ω^0 decays into $\mu^+\mu^-$ in central Au+Au collisions at 8 $AGeV$ normalized with proper multiplicity and branching ratio as given in Table 5.1. The invariant mass distribution of ω^0 meson after reconstruction is observed to be purely Gaussian, which essentially arise due to finite momenta of single muon tracks with no dispersion tails even at a region away from the mean value of the mass. This is due to the fact that momenta of muons are determined by STS in CBM experiment, where there is a minimum effect of multiple scattering as well as energy loss due to low material budget [94]. The reconstructed acceptance plot for omega mesons is displayed in Fig. 5.6; the figure indicates that maximum phase-space is covered.

To understand the effect of absorbers on signal muons, the reconstructed momentum distribution of single muons originating from the decay of ω^0 superposed with the input distribution obtained from PLUTO is shown in Fig. 5.7. Following important observations can be made from the figure : (a) absorbers introduce a threshold of $\sim p_\mu^{min} = 1\ GeV/c$ on a single muon momentum, below which all the signal muons are absorbed. The corresponding

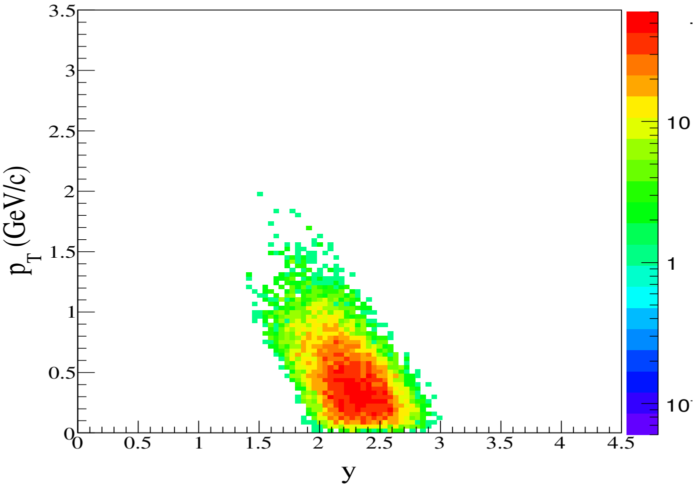

Fig. 5.6 Phase-space distribution of the reconstructed ω^0 *mesons in y-*p_T *plane for the central Au+Au collisions at 8 AGeV.*

threshold momentum for ω^0 meson is $p_\mu^{min} \approx 2.4\ GeV/c$ below which no ω^0 meson is reconstructed as is clear from the figure (b). Since the absorbers are placed along the forward direction, a cut is applicable on the longitudinal component instead of the transverse component of the momentum, which is clearly visible in p_T distribution of ω^0 mesons plotted in (a) of Fig. 5.8. The p_T range is identical for both input and reconstructed mesons. The rapidity distribution is displayed in (b) of the same figure and it is seen from the figure that the low rapidity ω^0 mesons are absorbed in the rapidity range corresponding to reconstructed ω^0 : $1.4 < \mathrm{y}_{\omega^0} < 3.2$ in the laboratory frame with midrapidity = 2.3. The corresponding rapidity coverage in the centre-of-mass frame comes out to be $-0.05 < \mathrm{y}_{\omega^0} < 1.8$, which shows the combined effects of finite geometrical acceptance of the muon set-up of the CBM as well as absorption of the low momenta muons by absorbers.

For the production of single ω^0 meson of mean multiplicity of 19 in central Au+Au collisions at 8 $AGeV$, which decays into dimuonic channel of branching ratio $9 \times 10^{-5}\%$, $\sim 6{\times}10^4$ collisions are required. To obtain a better statistics for ω^0 meson study, a large number of collisions should be simulated (several hundreds of a million). Due to limitation of the CPU calculation time, it is not

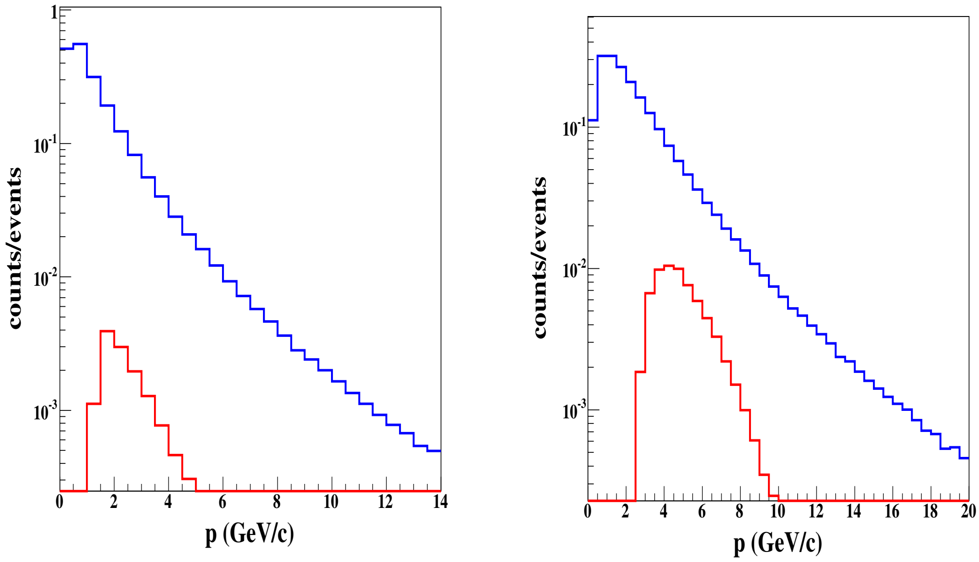

(a) *(b)*

Fig. 5.7 Distributions of momentum for reconstructed signal muons and ω^0 mesons in central Au+Au collisions at 8 AGeV (SIS100). Both the distributions are superposed on their respective input distributions. The blue and red curves correspond to reconstructed and input ω^0 mesons respectively.

easy to simulate such a huge data. To overcome this difficulty, Super-Event Technique is used in the present study. This technique is inspired by the event-mixing technique in the estimation of the combinatorial background for the experimental data. In this technique positively charged tracks are combined with each negatively charged ones of different events. Suppose that in a single central Au+Au collision, p and n represent the numbers of the tracks of positively and negatively charged particles respectively, then the number of combinations of two oppositely charged particles is equal to $p\times n$. If the tracks from N central collisions are combined using the Super-Event Technique,‘ then the number of pairs formed would be : $(N\times p)\times(N\times n) = N^2\times p\times n$, which correspond to N^2 equivalent events. With this approach, it is possible to enhance the statistics by a factor of N and overcome the CPU time limitation. In Fig. 5.9 invariant mass distribution of combinatorial background obtained by Super-Event Technique is displayed. In the Super-Event Technique, background is mostly generated by uncorrelated muon pairs,

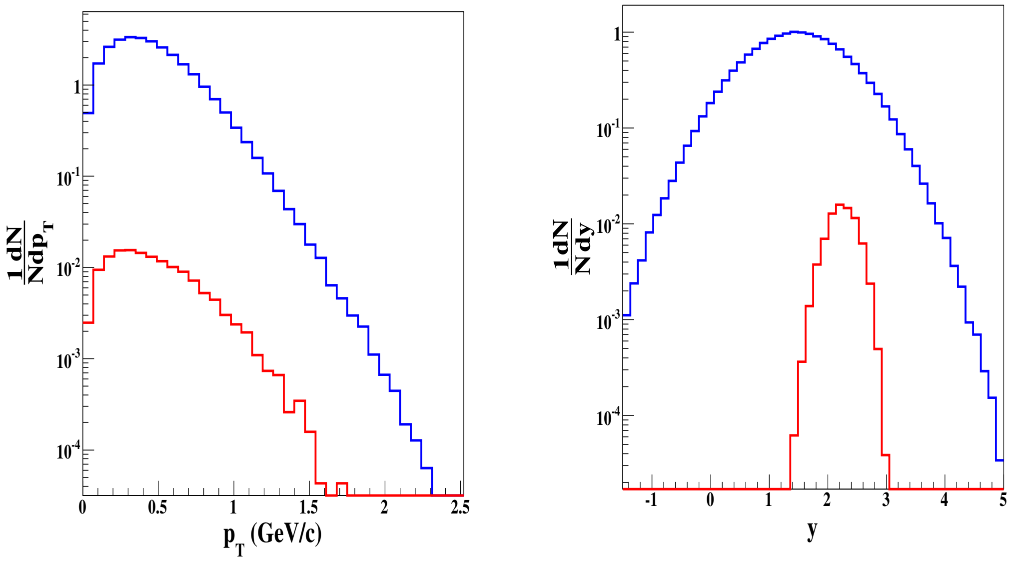

(a) *(b)*

Fig. 5.8 (a) Distributions of normalized transverse momenta and (b) rapidity plots, for reconstructed ω^0 mesons at 8 AGeV central Au+Au collisions. Both the distributions are superposed on their respective input (from PLUTO) distributions. The blue and red curves corresponds to reconstructed and input ω^0 mesons respectively.

whereas signals are generated by the correlated muon pairs. The background contains the contribution from hadrons, such as pions, kaons and protons, ghost tracks and other tracks. Beside these, a major component of background is the secondary muons, which arise due to weak decays of mesons.

For efficient detection of the signal, the background has to be substantially reduced by applying appropriate analysis cuts during the reconstruction procedure. The optimized analysis cuts include *STS Hits* ≥ 7, *MUCH Hits* ≥ 11, $\chi^2_{vertex}/n.d.f \leq 2.0$, and $\chi^2_{MUCH}/n.d.f \leq 1.3$. The final tracks which are selected after the application of optimal set of these analysis cuts are then projected on the TOF plane, where the TOF mass cut is applied as the final selection cut for the suppression of background due to pions, kaons and protons as shown in Fig. 5.10. The resulting invariant mass spectra are displayed in Figs. 5.5, 5.9 and 5.11. Fig. 5.11 shows the invariant mass spectra obtained by superposing ω^0 meson on the background according to their respective 'weights'. A small peak of ω^0 meson is visible, thus they can be efficiently

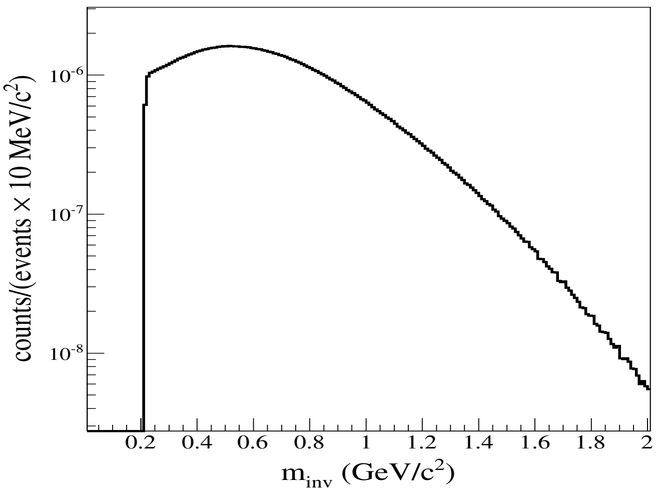

Fig. 5.9 Invariant mass distribution of combinatorial background for the central Au+Au collisions at 8 AGeV.

detected by MuCh (SIS100) set-up.

5.2.2 Invariant mass resolution

To evaluate the reconstruction efficiency, the reconstructed invariant mass distribution of ω^0 ($\rightarrow \mu^+\mu^-$) is fitted by the following Gauss fit function given as:

$$f(x) \;=\; p_0 \times \exp -0.5 \times (((x - p_1)/p_2)^2)) \tag{5.2}$$

where p_0 is a constant, p_1 is the mean value and p_2 is the standard deviation or RMS width of the invariant mass distribution having Gaussian shape. The value of invariant mass resolution is performed as $p_1 \pm 2\times\ p_2$. In this case, p_1 is equivalent to mean mass and p_2 is the RMS value as seen from Fig. 5.12. The mass of ω^0 meson used as input in the simulations was taken to be 782 MeV/c^2 from reference [118]. According to the method, the mass of ω^0 was found to be $p_1 \pm 2\times\ p_2 =$ (781.40 ± 11.84) MeV/c^2, which is consistent with the input value within the error bars. The width of the distribution originates from detector effects rather than from the width of the resonance mass of ω^0, which is very small. The very satisfactory invariant mass resolution of only $\sim$

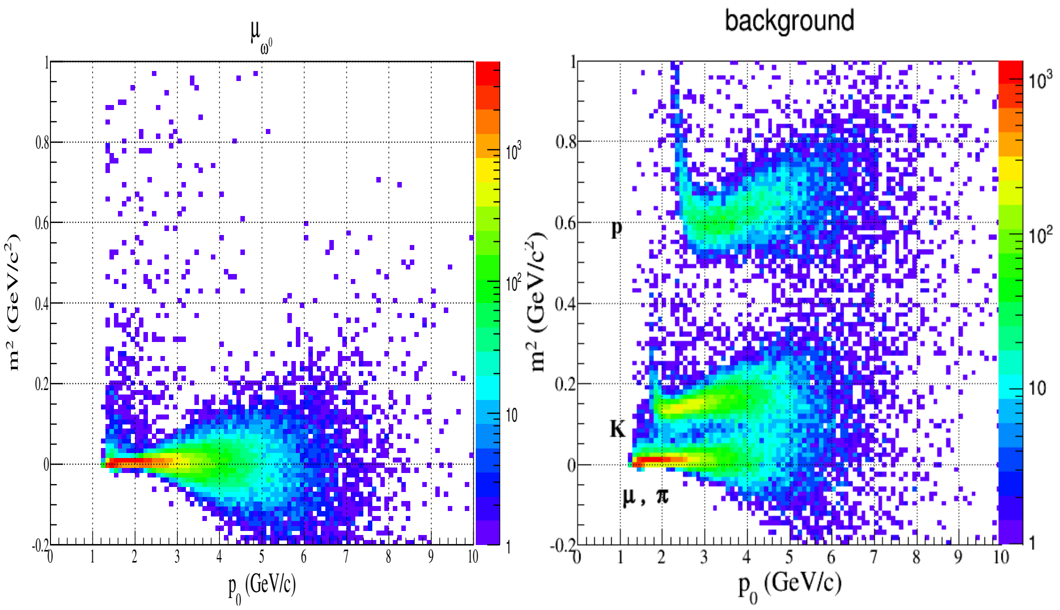

(a) *(b)*

Fig. 5.10 Mass squared as measured by the TOF detector versus particle momentum simulated for the central Au+Au collisions at 8 AGeV. Left panel shows muons from ω^0 decays and [right panel] exhibits background consisting of secondary muons, pions, kaons and protons.

11.84 MeV/c^2 can be considered as a success of the tracking algorithm and the very accurate STS, which leads to a momentum resolution of $\sim 1\%$. It is particularly helpful as the ω^0 mesons can be found in a narrow invariant mass window. This leads to better extraction of the signal and, therefore, reasonably good signal to background ratio.

5.2.3 Determination of reconstruction efficiency

One of the most important parameters required for assessing the performance of MuCh detector set-up is reconstruction efficiency. The reconstruction efficiency is evaluated by taking into account the ratio of the number of reconstructed signal pairs found within the mass region of interest obtained after applying the optimum analysis cuts to the total number of input signal pairs.

In order to evaluate the reconstruction efficiency, the reconstructed invariant mass distribution of ω^0 ($\rightarrow \mu^+\mu^-$) is fitted by Gauss's fit function given by Eq. 5.2. The invariant mass region of interest is selected between

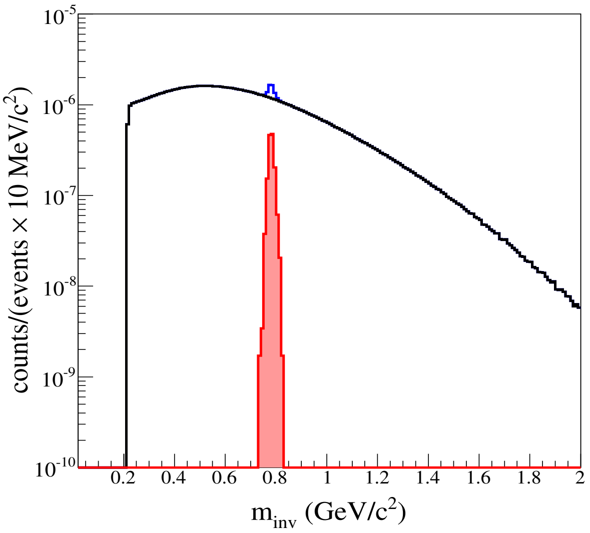

Fig. 5.11 The total reconstructed invariant mass spectra obtained by adding properly weighted signal and background.

bin_{max} and bin_{min}, where, bin_{max} = p_1 + $2p_2$ and bin_{min} = p_1 - $2p_2$. The integration of signal entries lie within this region and gives the number of signal entries. This choice is dictated by the fact that roughly 95.5% of all the signal entries are included in this region of the Gaussian fit function. If N is the total number of input signal and I_N is the number of entries within the selected region, then the reconstruction efficiency is expressed as :

$$\epsilon = \frac{I_N}{N} \tag{5.3}$$

The reconstruction efficiency turns out to be $\sim$ 0.83%.

5.2.4 Estimation of signal to background ratio

Another important parameter required for evaluating the performance of MuCh detector set-up is signal to background ratio. It is evaluated by taking the entries of the background lying within the selected mass region as discussed above. Suppose 'Bg' represents the number of background entries in the area of interest of invariant mass region and 'S' is the number of normalized (normalized by suitable multiplicity and branching ratio) signal entries, then the signal to background ratio is,

$$\frac{S}{B} = \frac{S}{Bg} \tag{5.4}$$

The pictorial representation of the calculation of signal to background ratio is illustrated in Fig. 5.12. The evaluted value of signal to background ratio is found to be ~ 0.30.

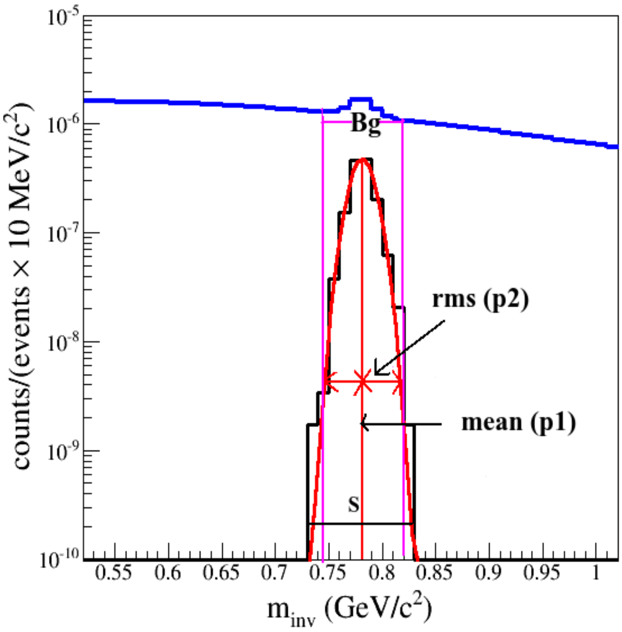

Fig. 5.12 Invariant mass spectra with mean and upper and lower limits for the estimation of signal to background ratio at 8 AGeV central Au+Au collisions.

5.3 Segmentation of detector module into pads

MuCh consists of sliced absorbers and triplet of tracking chambers based on GEM technology, which are placed inside the air gap of width 30 cm between two absorbers. To take into account the realistic scenario, this modular structure has been implemented. Each detector layer is divided in several modules of size 30 $cm \times 30$ cm and is filled with Ar+CO$_2$ gas mixture. However, one of the disadvantages of modular design is non-availability of larger size GEM modules, which results in complex design and large number of dead zones. One of the practical solutions to address this difficulty is to divide the detector planes into several sectors instead of modules. In the case of sector design, large GEM foils limited by 60 *cm* size (width) in one direction and no restriction on length are available and are being made by CMS and other experiments [119]. The number of sectors are tunable. The GEM detectors are equipped with readout planes. The experimental challenge faced by MuCh is to extract muonic tracks from the environment of high multiplicity of other charged particles. The required readout planes are not suitable for the detection of such a larger number of tracks with high precision. In order to account for realistic signal generation, the readout planes of the modules are segmented into smaller 2-dimensional detection units called *pads* for obtaining final detectable response.

Study of segmentation is important due to the following reasons :

- values of occupancy and multi-hit probability determines the feasibility of tracking and efficiency of muon measurements,
- the total number of pads influences the cost and
- the small pad size is important from the point of view of fabrication and signal strength.

5.4 Data rate of tracking chambers

The CBM experiment has been designed to measure the rare diagnostic probes coming from the fireball and, therefore, will be operated at reaction rates of $\approx 10\ MHz$. This poses challenges with respect to the rate capability and radiation hardness on the muon chambers. It is, therefore, necessary to perform a study of the particle density and detector occupancy.

5.4.1 Point density

Point density is defined as the number of MuCh points or MC points per unit area per event on the tracking chamber planes. They provide information about the estimated particle rate incident on the chamber planes; the point density is maximum at the first station and falls with distance from the beam pipe as displayed in Fig. 5.13 for 10^5 central Au+Au collisions at 8 $AGeV$. For the minimum bias events, the number is scaled by a factor of 0.25 [94]. For the pads of dimensions 1 cm × 1 cm, the maximum peak data rate in the central zone will be 10 MHz (beam rate) × 0.1 (peak value of particle density) = 1 MHz on the first station and for minimum bias zone it is scaled by factor of 0.25 and its value ≈ 0.75 MHz [94].

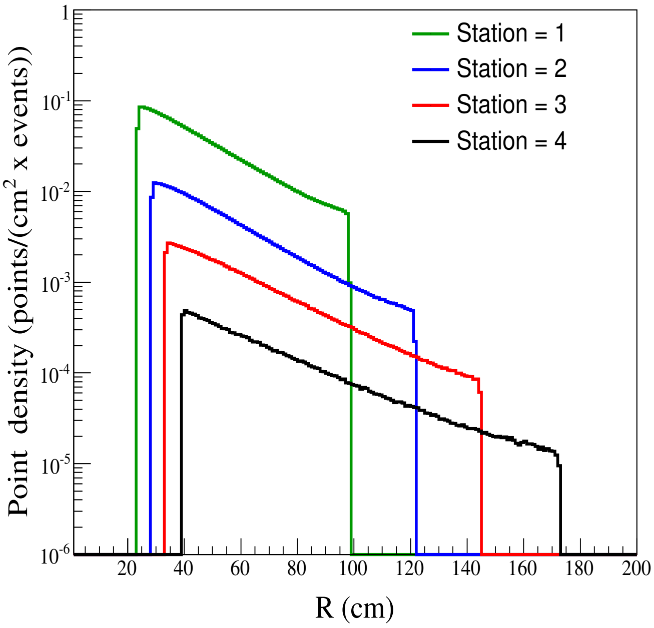

Fig. 5.13 Point densities in the tracking chambers of all the stations for central Au+Au collisions at 8 AGeV.

5.4.2 Detector occupancy

Particles while passing through GEM detector interact with the gaseous medium and ionize, thereby depositing their energies. After digitization, the ionization process (primary and avalanche) adds to the profile of MuCh points and increase the data volume accordingly. The data rate estimated for the pads of dimensions : 1 cm × 1 cm, will reduce according to the pad size. Another quantity called occupancy, is defined as the fraction of fired pads per event, which determines the hit rate. The radial distribution of occupancy for trapezoidal modules for 8 $AGeV$ central Au+Au collisions is exhibited in Fig. 5.14.

As the first station has the highest particle density, therefore, the number

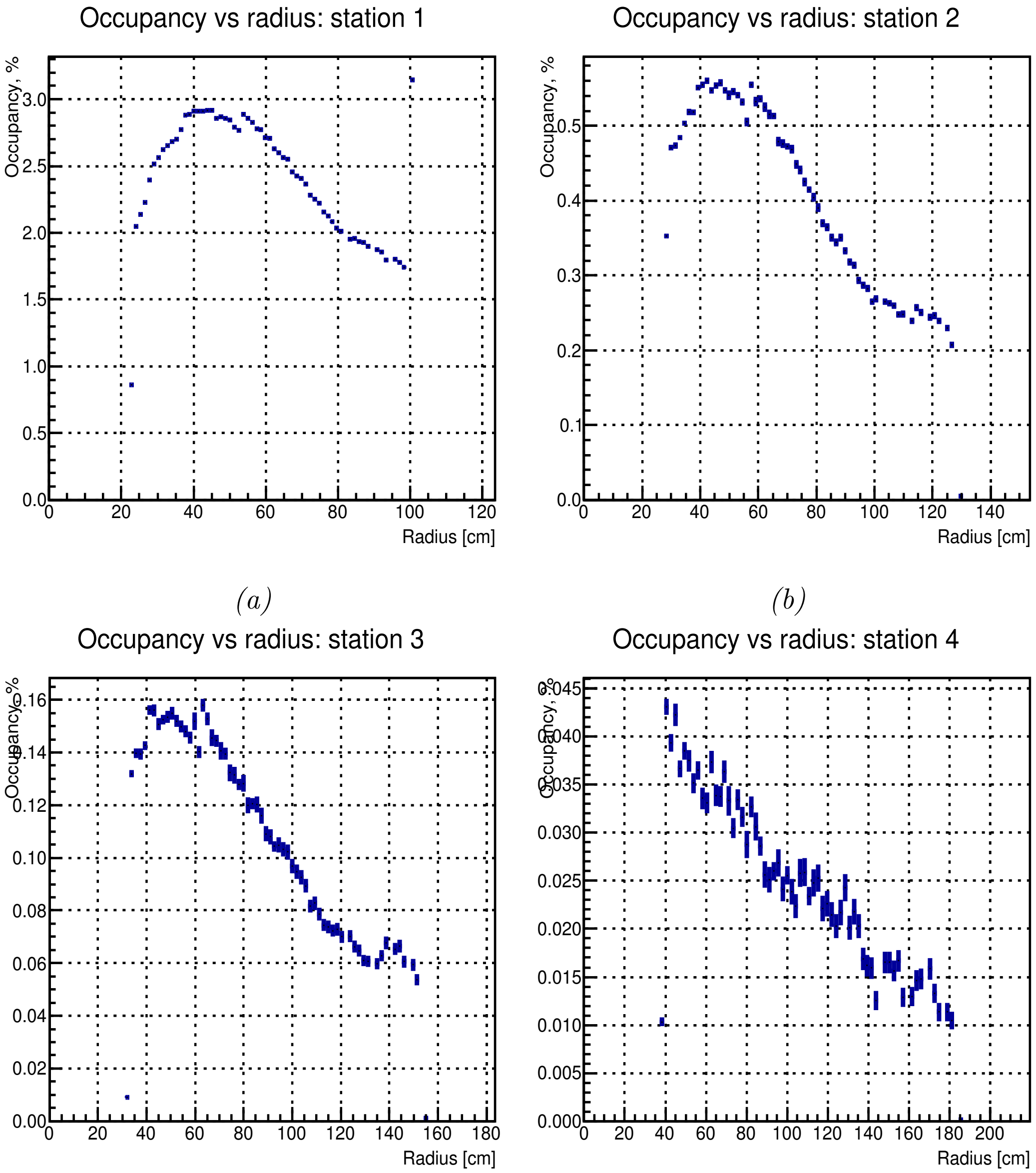

(a) *(b)*

(c) *(d)*

Fig. 5.14 Radial distribution of occupancy for the four stations of MuCh (SIS100) geometry with trapezoidal modules. The plot is generated for central Au+Au collisions at 8 $AGeV$.

of pads fired in the first station is the maximum. For a pad area projected according to the hit rate has constant occupancy over the entire radial distance.

However, we have considered a square pad approximation with pad length corresponding to 1° in azimuth. This, therefore, results in decrease in occupancy with distance as discernible from Fig. 5.14. It is seen from the figure that even for the beam energy of 8 $AGeV$, the maximum occupancy obtained at the first station is 3%, which is less than the expected for a designed value of 5% occupancy. It should, however, be mentioned that for the self-triggered system, more useful quantity for the hit rate is the occupancy by minimum bias events, which is roughly 2% in the region around the first station near the beam pipe.

5.4.3 Hit density

Simulation study has been done by using GEANT3 transport code for estimating hit density; hit density is defined as :

$$Hit\ density = \frac{Number\ of\ hits}{cm^2 \times\ event} \tag{5.5}$$

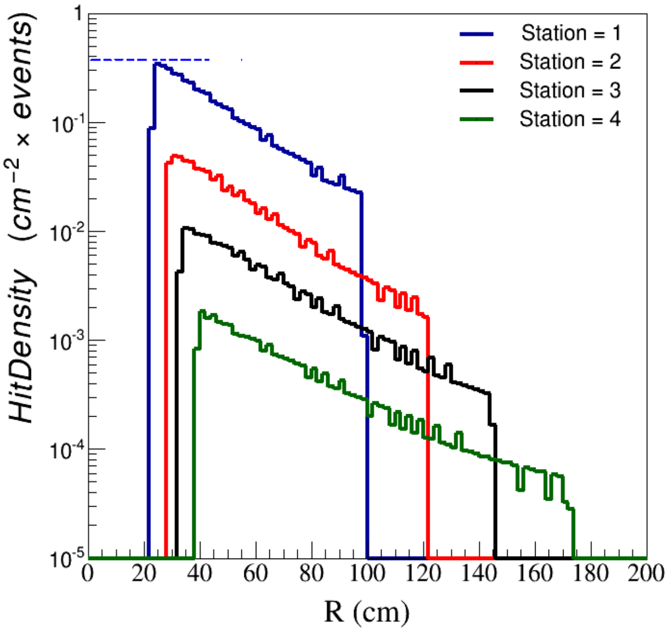

Fig. 5.15 Hit densities in the tracking chambers of all the stations for central Au+Au collisions at 8 $AGeV$ obtained by using UrQMD and GEANT3 transport codes. Figure shows the variation of hit density with radial distance from beam pipe for 8 $AGeV$.

Fig. 5.15 exhibits the plot of hit density as a function of radial distance from the beam axis for all the stations, estimated with UrQMD event generator for the central Au+Au collisions at 8 $AGeV$. It can be seen from the figure that the hit density falls with distance from the beam axis; the maximum value is obviously for the first station. The hit density for the innermost part of layer of the first detector reaches $\sim 0.03\ cm^{-2} event^{-1}$ at 8 $AGeV$. As the MuCh (SIS100) can handle interaction rates $\sim 10\ MHz$, hit rate faced by the innermost layer of the first detector will be $\sim 0.3\ MHz/cm^2$ (hit density × interaction rate) at 8 $AGeV$. To take into account the variation of hit density with radial distance from the beam pipe, the MuCh readout planes are segmented into different annular regions as displayed in Fig. 5.16 with small pads of appropriate shapes and sizes in order to achieve the desired pad occupancy ($\sim 5\%$). The main constraints relating to pad size optimization are : hit occupancy and spatial resolution. The sizes of the pads are determined by the angular separation in the transverse plane.

For optimizing the value of pad sizes, detector layers are divided into various annular regions as shown in Fig. 5.16. These annular regions are filled with square pads of varying sizes as function of azimuthal angle satisfying the condition : $dr = r\Delta\phi$. This segmentation scheme helps maintain the occupancy close to a constant value, which in turn enables one to avoid a radial dependence of the detector response. A simulation study has been done by varying the azimuthal angle from 0.4 to 1.2°. The detector is segmented into the same segmentation angle through out the MuCh detectors.

5.5 Results of segmentation optimization

In this section, final results on the segmentation optimization are given for various segmentation angles for 8 $AGeV$ Au+Au central collisions. Fig. 5.17 shows the radial distribution of the hit densities for different segmentation angles for the first station, where the hit or point density is the highest. It can be seen from Fig. 5.17 that hit density is the maximum near the beam pipe

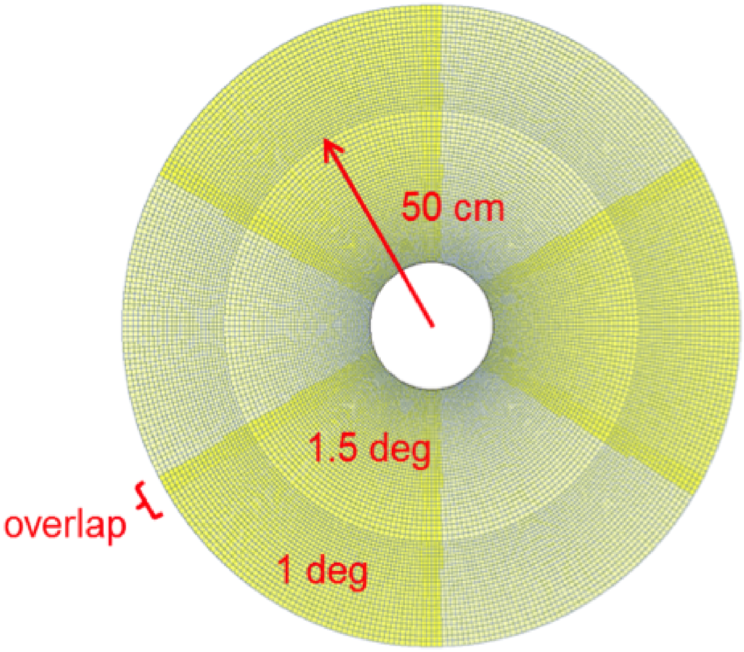

Fig. 5.16 A schematic view of segmentation of the detector layers into annular region with small pads of varying sizes.

and falls with increasing distance from the beam pipe. The trends are similar for all the segmentation angles. It is observed from the figure that the hit density is nearly independent of the segmentation angle. As the point density is maximum near the beam pipe, hence the hit density and point density are the highest. Since the pad size depends on the segmentation angle, the pad sizes are smaller for smaller segmentation angles. The pads of smaller sizes will have higher hit density than the pads of larger sizes due no loss of hits due to overlapping of hit falling on the same pads for larger pad sizes, which is more prominently visible at a larger distances. The hit efficiency is defined as:

$$Hit\ efficiency = \frac{Number\ of\ hits}{Number\ of\ MC\ points} \tag{5.6}$$

The variation of hit efficiency as a function of segmentation angle is displayed in Fig. 5.18. The hit efficiency decreases with increasing angle. As hit density is the highest for the smallest angle, therefore, the hit efficiency is maximum for smaller angles. The hit efficiency decreases with segmentation angle from

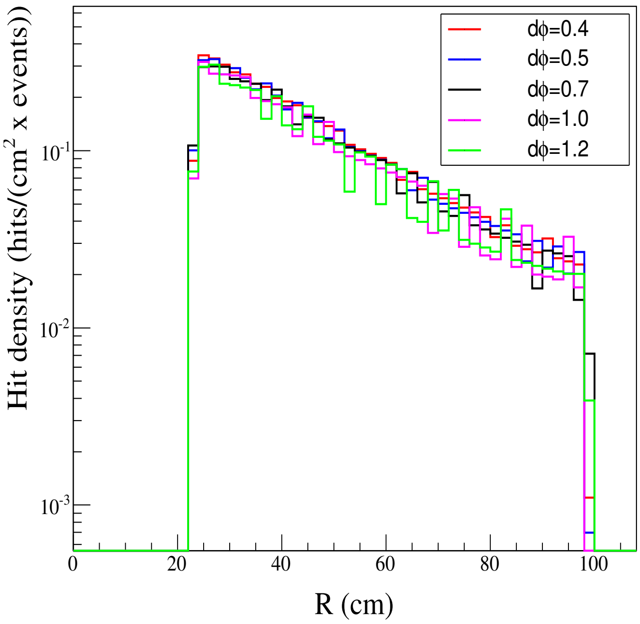

Fig. 5.17 The radial distribution of hit densities for the first station as a function of the segmentation angle.

$\sim 98\%$ for $d\phi = 0.4°$ to $\sim 85\%$ corresponding to $d\phi = 1.2°$. Fig. 5.19 exhibits the dependence of occupancy on segmentation angle for the first station. It can be seen from the figure that occupancy increases with increasing segmentation angle. As the sizes of the pads increase the number of fired pads increase which results in an increase in occupancy. The maximum occupancy for different segmentation angles is close to the expected value : 5 % required for the fabrication of the detector, even for the largest segmentation angle, 1.2° the value is 4%. So they are suitable for the fabrication of the detector.

The optimized pad size must have low hit density and low occupancy value in order to reduce cost of fabrication of the detector. On the basis of these requirements, details of dimensions of the pads for different segmentation angles are given in Table. 5.2.

To examine the performance of the optimized pad sizes, the reconstruction efficiency and signal to background ratio are calculated. The effect of segmentation angle on invariant mass distributions of background and signal are exhibited in Fig. 5.20.

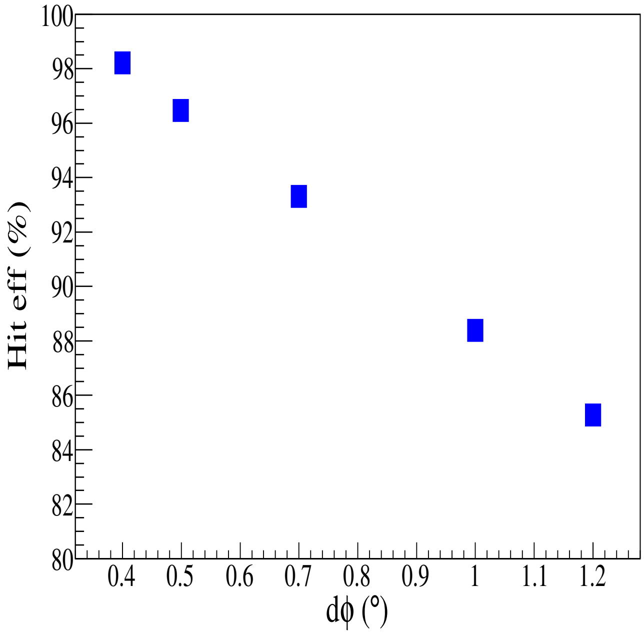

Fig. 5.18 Variation of hit efficiency with segmentation angle.

Table 5.2 The estimated values of the pad sizes and number of pads for triplet layer of tracking chambers for different segmentation angle.

$d\phi$ (°)	**min. pad size** (mm^2)	**max. pad size** (mm^2)	**No of pads (total for 3 layers)**
0.4	1.4 × 1.4	6.5 ×6.5	615600
0.5	1.7 × 1.7	8.1 × 8.1	393120
0.7	2.4 × 2.4	11.4 × 11.4	202114
1.0	3.5 × 3.5	16.2 × 16.2	99360
1.2	4.2 × 4.2	19.5 × 19.5	69300

The peak height of the invariant mass distribution of the reconstructed background increases with segmentation angle, whereas it decreases for the signal ω^0 mesons. The sizes of the pads for smaller segmentation angles are smaller and the pad size increases with increasing segmentation angle. Hence, the number of hits falling on the single pad will be reduced for smaller segmentation angles. This will minimize the mismatch between the tracks in STS and MuCh. The mismatch gets enhanced with increasing segmentation angle due to larger pad sizes and overlapping of the fired pads, thereby

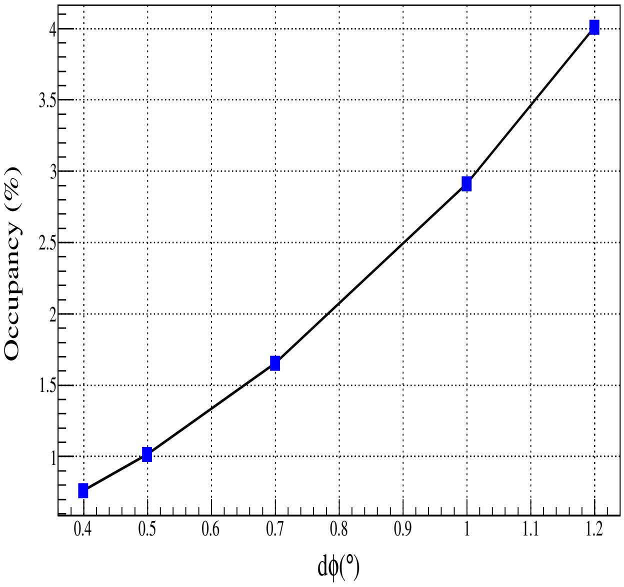

Fig. 5.19 The variation of occupancy with segmentation angle.

increasing the background. Moreover, in the case of signal mesons, it is essentially constant due high momenta muons. This effect is less sharp in the case of the signal. To demonstrate the significance of the optimized value of segmentation angle in obtaining pad size of appropriate dimensions with reduced cost, the values of reconstruction efficiency and signal to background ratio are calculated for a set of segmentation angles and the results are presented in Table. 5.3.

Table 5.3 Estimated values of reconstruction efficiency (ϵ_{ω^0}), signal to background ratio (S/B) and mass resolution σ_{ω^0} of ω^0 meson for different segmentation angles.

$d\phi$ (°)	ϵ_{ω^0} (%)	**S/B**	σ_{ω^0} (MeV/c^2)
0.4	0.98	0.39	0.01112
0.5	0.95	0.36	0.01110
0.7	0.92	0.33	0.0.01108
1.0	0.83	0.30	0.01102
1.2	0.78	0.29	0.01099

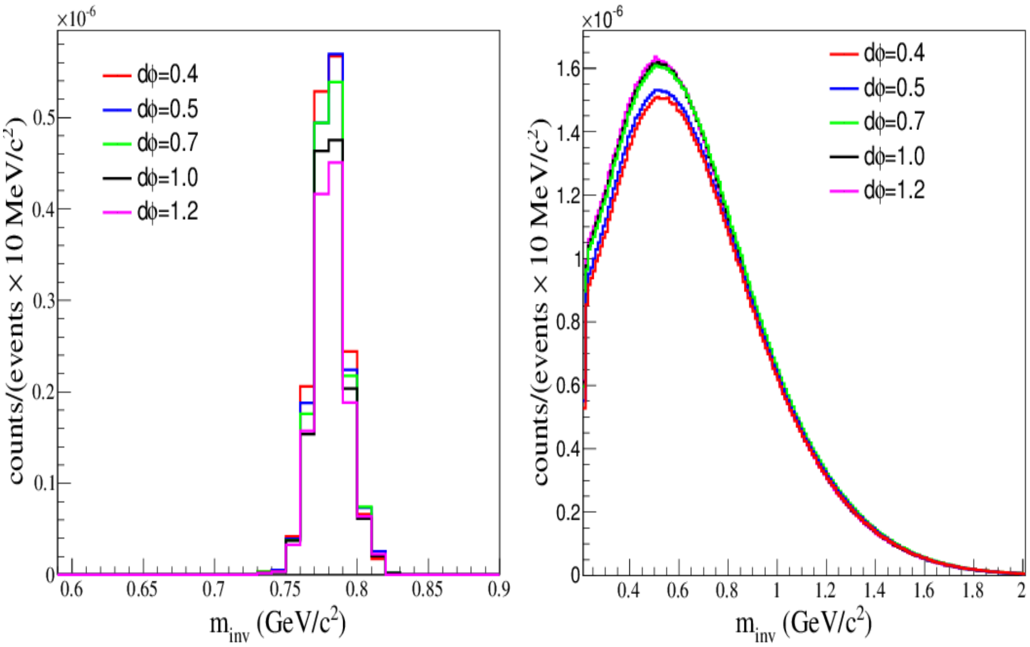

(a) *(b)*

Fig. 5.20 Invariant mass distributions for signal ω^0 mesons and background as a function of segmentation angle ($d\phi$). Dependence of the peak height of the invariant mass distribution for : a) ω^0 mesons and b) background, as a function of segmentation angles.

Table. 5.3 depicts that with increasing segmentation angle, reconstruction efficiency as well as signal to background decreases. It may be noted that segmentation angles, $d\phi = 0.7°$ or $1°$ is the optimized value. However, the dimensions of the pads corresponding to $d\phi = 0.7°$ is $2.4 \times 2.4\ mm^2$ and for $d\phi = 1°$ is $3.5 \times 3.5\ mm^2$. The number of pads will relatively be lesser for $1°$ in comparison to the value for $d\phi = 0.7°$. The GEM detectors segmented with pad of $d\phi = 1°$ for MuCh will substantially reduce the cost of fabrication of the detector. Thus, segmentation angle $d\phi = 1°$ seems to be the optimum choice for the fabrication of GEM detector [120, 121], segmented into pads.

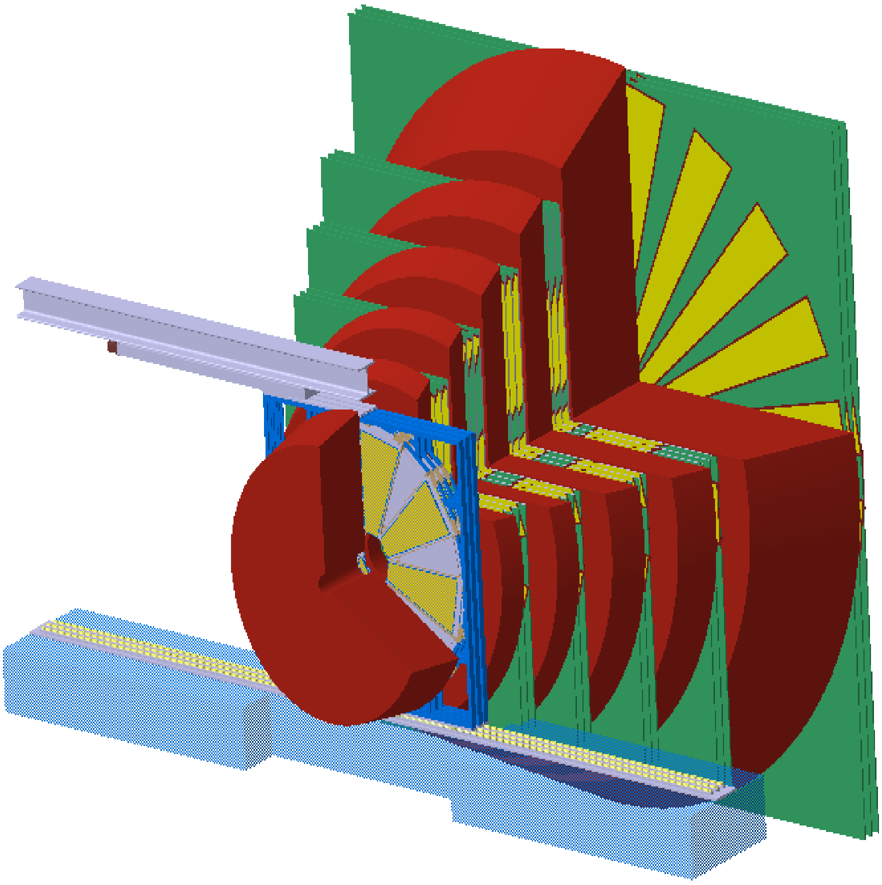

Multi-strange hyperons production at FAIR energies

Chapter 6

Multi-strange hyperons production at FAIR energies

Nuclear collisions at FAIR energies are envisaged to produce net baryon densities ≈ 5 - 6 times higher than the normal nuclear matter density. At such high densities, baryons start melting into their constituents, the quarks and gluons, forming a mixed or even deconfined medium. Such collisions will be explored at FAIR. As multi-strange hadrons plays a major role as diagnostic probes of the dense QCD matter. Hence, a simulation study is carried out by employing transport models at the FAIR energies.

This chapter begins with an introduction to strangeness enhancement as one of the signatures of the formation of QGP; models used are also discussed. The results of the study are summarized in the end of this chapter.

6.1 Introduction

One of the main objectives of relativistic heavy-ion collision experiments is to study the strongly interacting nuclear matter under extreme conditions of temperature and/or baryon chemical potential. Under these conditions, nuclear matter is expected to undergo a transition to a medium of free quarks and gluons, known as quark-gluon plasma [122]. Several signatures have been proposed to probe creation of such a novel state of matter. One of the proposed signatures is the relative enhancement of strangeness production, measured by the ratios of yields of multi-strange hyperons in A+A collisions in comparison to those in p+p collisions or central to peripheral A+A collisions. Unlike up and down quarks, strange quarks and antistrange quarks are formed in pair in the collisions between the constituents of the plasma and was not present in the colliding nuclei. The production of strange particles is, therefore, considered as a probe of QGP formation.

The dominant mechanism of production of $s\bar{s}$ pairs in QGP is via gluon fusion ($gg \rightarrow s\bar{s}$) followed by chemical equilibration (time, $\tau_{QGP}^{eq} \approx 10\ fm/c$), contrary to the case of a pure hadronic scenario, where such reactions are almost absent [123–126].

If QGP is formed at large baryon chemical potential, which is likely to occur in heavy-ion collisions in the beam energy range : 5 - 40 AGeV, there might be an enhancement in the production of s and $\bar{s}$ quarks in comparison to u and d quarks production [123–129]. This happens due to the suppression of the creation of light-quark pairs due to the Pauli exclusion principle [130]. As a result, the production of strange baryons will be enhanced [131]. The effect will be more pronounced in the case of production of multi-strange baryons and antibaryons, thus making them to be sensitive probes for the QGP formation. Therefore, it has been proposed to study the relative enhancement of Ξ^- and Ω^- production in heavy-ion collisions in comparision to p+p or p+A collisions [132–140].

Several experiments have been performed to study hadron production in relativistic nucleus-nucleus collisions [80, 141]. It has been observed that the enhancement increases with the number of strange quarks and centrality of the collision [134]. The strangeness enhancements were observed at all the beam energies, from top SPS and RHIC energies down to AGS energy [142, 143]. At AGS energies the production of Λ is more in comparison to those at the top SPS or RHIC energies [144].

One important production process for multi-strange hyperons as implemented in the transport models are strangeness exchange reactions like $\Lambda K^- \rightarrow \Xi^- \pi^0$, $\Lambda\Lambda \rightarrow \Xi^- p$ and $\Lambda\Xi^- \rightarrow \Omega^- n$ and $\Xi^- K^- \rightarrow \Omega^- \pi^-$ [145]. These multistep processes depend on the density of the medium, and hence, the production of multi-strange baryons has the potential to probe the density and the EOS of the medium. In the grand canonical ensemble scenario, the statistical hadronization model explains reasonably well the relative yields of strange hyperons in the central A+A collisions with the highest Λ/π^- and Ξ/π^- ratios at beam energies ≈ 30 $AGeV$ [146, 147]. Below this energy, strange baryons contribute significantly to strangeness production because of the very large value of the chemical potential. Transport models like UrQMD or the statistical hadronization model explain fairly well the yields of non-strange and particles with a single strange quarks. However, the production of multi-strange particles are always underestimated by these models. For example, at subthreshold beam energies $\Xi^-/(\Lambda^0+\Sigma^0)$ ratio was found to be significantly higher than the model predictions [148].

In experiments at AGS and SPS up to beam energies of 30 $AGeV$, mostly non-strange and singly-strange or at the most doubly-strange particles were studied. For example, only about 300 Ξ^- hyperon have been measured in Au+Au collisions at 6 $AGeV$, and no Ω^- hyperon was found up to beam energies around 30 $AGeV$ [144]. The reason for the poor data situation at AGS and low SPS energies is the low rate capability of the detectors used so far. In contrast, the Compressed Baryonic Matter (CBM) experiment at FAIR is designed for unprecedented reaction rates (up to 10 MHz). It will allow precision measurement of multi-strange hyperon production in heavy-ion collisions at beam energies close or even below the thresholds energy [149].

Thus, model based systematic study of the production of strange particles with varying strangenesses quantum number has been carried out by using several commonly used transport models at FAIR energies. In Section 6.2, a brief description of the basic features of the models (AMPT and UrQMD) and the production mechanism of multi-strange particles in heavy-ion collisions has been presented. In Section 6.3, the results and model predictions for the production of the particles with higher strangeness contents has been given.

Finally, the conclusion based on the analysis will be comprehensively discussed in Section 6.4.

6.2 Models

We have used the microscopic transport model UrQMD [150, 151] and the hybrid transport model AMPT [152]. These models were extensively used earlier to explain the strangeness production data on p+p, p+A and A+A collisions at AGS to RHIC energies. In this section, we briefly describe the basic and essential features of these models.

6.2.1 UrQMD

The UrQMD model is based on the concept of strings, which produce hadrons by fragmentation. The rescattering of the strings and the products of their interactions are taken into account. The production of particles proceeds via the decays of meson and baryon resonances or string excitation and fragmentation. The production of multi-strange particles can be enhanced by reducing the corresponding quark masses of the fragmented part of the initial strings in the dense matter, or by increasing the string tension [153]. The reactions required for the production of multi-strange particles include multi-mesonic channels such as $Y + N \leftrightarrow n\pi + n_Y \bar{K}$ or $\bar{Y} + N \leftrightarrow n\pi + n_{\bar{Y}} K$, where n, n$_Y$ and n$_{\bar{Y}}$ denote respectively the numbers of pions, strange and antistrange quarks within the hyperons,Y , and antihyperons, $\bar{Y}$ [154–156]. For our investigation we have used version UrQMD 3.4 of the model [157].

6.2.2 AMPT

In the AMPT transport model, the HIJING model [158] is used to obtain initial spatial and momentum distributions of hard minijet partons and soft strings, which undergo rescattering described by Zhangs Parton Cascade (ZPC) [159]; ZPC includes two-body scattering with scattering cross section for parton-parton scattering obtained from pQCD with screening mass. Then the produced partons or strings undergo hadronization by Lund String Fragmentation model

[160] (in default mode) or by Quark Coalescence Model (QCM) (in string melting mode) which is similar to ACOLOR model approach [161–164]. The interaction of the produced hadronic matter is then further treated by ART [165, 166]. It is important to emphasize that AMPT is a hybrid transport model and considers initial partonic and final hadronic states undergoing interactions and phase transition between these two states of the nuclear matter. In order to examine whether hyperon production is sensitive to the degrees of freedom in the collision volume, both the string melting (partonic matter) [167–169] and the default mode (hadronic matter) [170, 171] of the AMPT model are used for calculating the particle yields. In the default mode, the partons remain attached to its parent string and when the interactions stop, they fragment into hadrons according to the Lund String Fragmentaion model. However, in the AMPT string melting mode, these strings are converted into partons, which undergo elastic collisions, and finally convert into hadrons by quark coalescence where the nearest partons combine to form hadrons. The production of multi-strange baryons in AMPT default model is realized via the following strangeness-exchange reactions [172]:

$$\bar{K}\Lambda \leftrightarrow \Xi\pi, \quad \bar{K}\Sigma \leftrightarrow \Xi\pi, \quad \bar{K}\Xi \leftrightarrow \Omega\pi, \tag{6.1}$$

and

$$K\bar{\Lambda} \leftrightarrow \bar{\Xi}\pi, \quad K\bar{\Sigma} \leftrightarrow \bar{\Xi}\pi, \quad \bar{\Xi} \leftrightarrow \bar{\Omega}\pi. \tag{6.2}$$

As there are no experimental results on the reaction cross sections for the above processes, they are derived by assuming that for multi-strange hyperon production processes, the transition matrix elements above threshold energies are similar to the matrix elements for $\bar{K}N \leftrightarrow \pi\Sigma$ reaction [173].

The multi-strange hyperon production in AMPT string melting mode takes place by the recombination of the partons into hadrons by QCM. In order to perform simulation study we have used the AMPT transport model versions AMPT-1.26t4 [174].

6.3 Multi-strange hyperon production

Particle yields in central Au+Au collisions ($b < 3\ fm$) at energy from 5 to 90 $AGeV$ using 1 million events are calculated. The energy dependence of the yields of strange particle and the ratio of yields of strange particle relative to pion yields is also investigated. The analysis is done using the particles produced in the mid-rapidity region, -0.5 < y < 0.5.

6.3.1 Excitation function for hyperon production

The average multiplicities of Λ^0, Ξ^- and Ω^- and their antiparticles are plotted as a function of beam energy in Figs. 6.1 and 6.2.

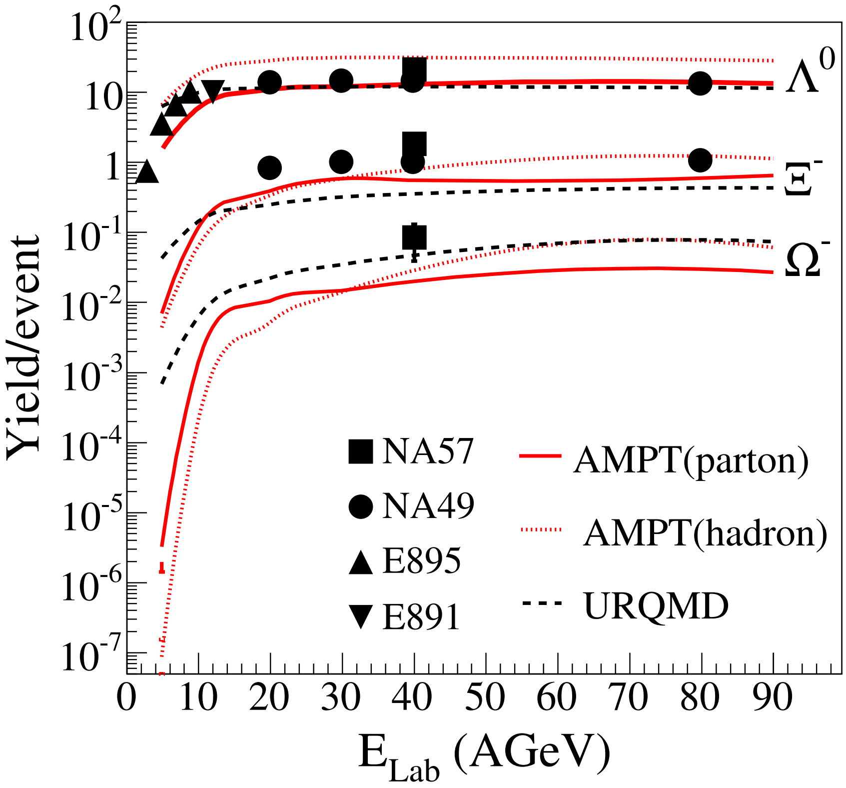

Fig. 6.1 Mean multiplicities of Λ^0, Ξ^-, *and* Ω^- *hyperons for central Au+Au collisions as a function of beam energy. Lines represent the results of model calculations and various symbols (▼,▲,●,■) denote experimental data (AGS, NA49, NA57) [133, 136, 175].*

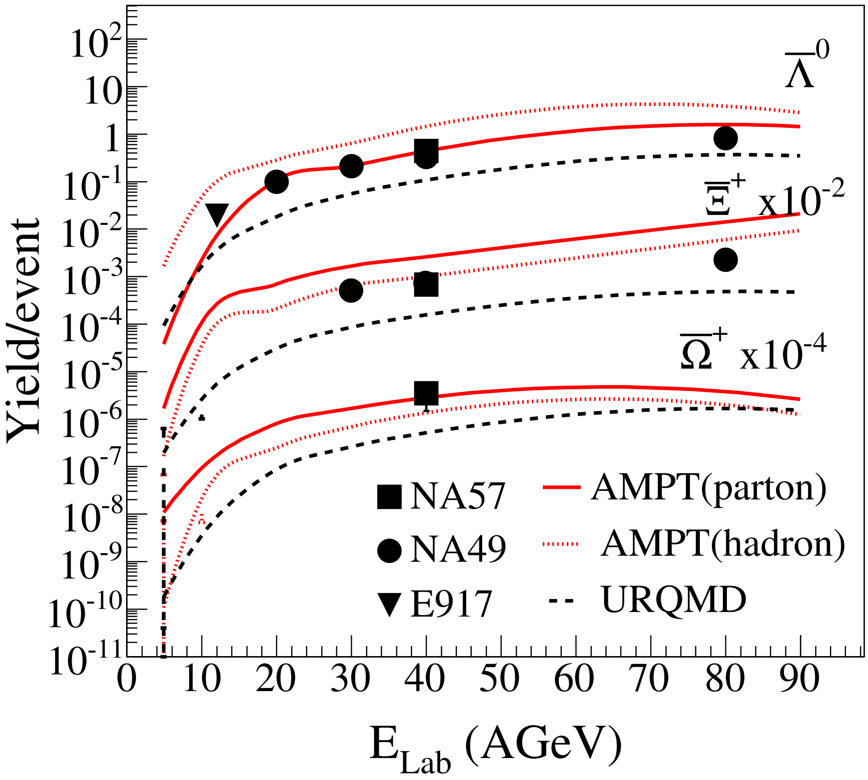

Fig. 6.2 Mean Multiplicities of antihyperons $\bar{\Lambda}^0$, $\bar{\Xi}^+$ ($\times$ 10^{-2}), and $\bar{\Omega}^+$ ($\times$ 10^{-4})for central Au+Au collisions as a function of beam energy. Lines are results of model calculations, whereas, symbols (▼,▲,●,■)represents experimental data (AGS, NA49, NA57).[133, 136, 175]

The lines correspond to the results of the AMPT model calculations for both hadron and parton modes and UrQMD, whereas the symbols (▼,▲,●,■) represent available experimental data [133, 136, 175]. The average yields of anti-hyperon in Fig. 6.2 are scaled for a better visualization. From Figs. 6.1 and 6.2, the following statements can be made regarding the models :

- The UrQMD model reproduces reasonably well the average yields of Λ^0 hyperons, but underestimates the average yields of multi-strange hyperons. The anti-hyperon yields are underestimated by a factor of about 5.

- The AMPT (hadronic) mode of the model overestimates the average yields of Λ^0 hyperons, and significantly underestimates the average yields of multi-strange hyperons. The yield of $\bar{\Lambda}^0$ hyperons is also overestimated, whereas the multi-strange antihyperons are described reasonably well. The partonic mode of AMPT model underestimates the measured data points, in particular for the multi-strange hyperons, but overestimates the production of $\bar{\Lambda}^0$ and $\bar{\Xi}^+$ hyperons. The $\bar{\Omega}^+$ data points are reproduced fairly well.

It is worth mentioning that above a beam energy of about 30 *AGeV* the predicted values from models are more or less saturated and keep their relative differences. However, at beam energies below 30 *AGeV*, the different models exhibit different slopes as displayed by the figure. This is particularly true for the two versions of the AMPT transport model. For example, at a beam energy of 10 *AGeV*, the AMPT hadron mode predicts a higher average yield of Λ^0 hyperon than those from parton mode, whereas, there are an opposite trends for Ξ^- and Ω^- hyperons. The similar trends are observed for the antihyperons.

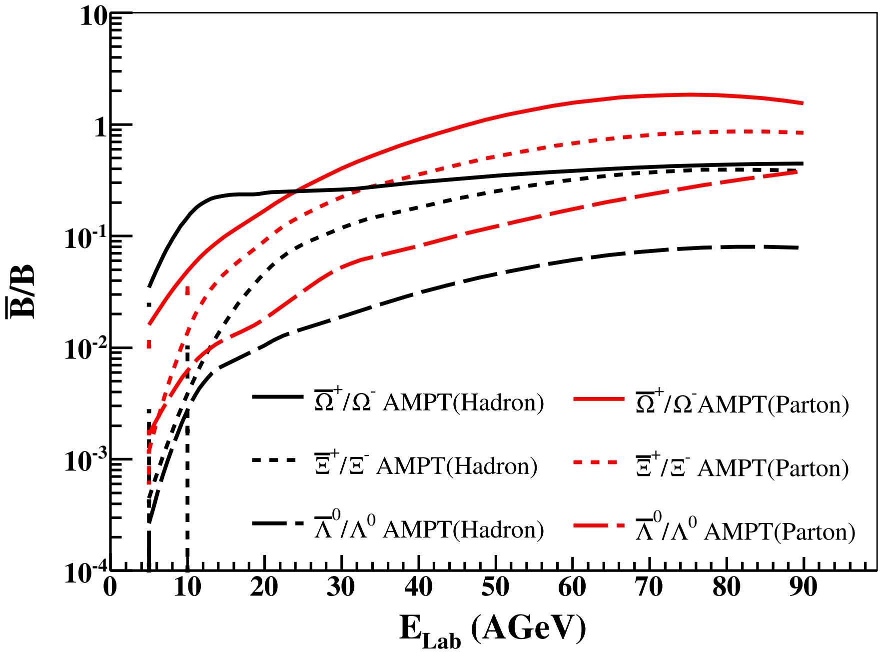

Fig. 6.3 Mean multiplicity ratios of hyperons and antihyperons as calculated with the AMPT model for the hadronic and the partonic scenarios for central Au+Au collisions as a function of beam energy.

According to the simulations studies performed with the AMPT transport code, the hadronic scenario could be distinguished from the partonic one by the steepness of the excitation functions of multi-strange hyperons and antihyperons production in heavy-ion collisions at beam energies up to around 20 *AGeV*. This is reflected in Fig. 6.3, which depicts the ratios of the average multiplicities of Λ^0, Ξ^-, Ω^- and their antiparticles as a function of beam energy for central Au+Au collisions. The increase of the particle ratios with increasing beam energy of up to 20 *AGeV* is significantly steeper for the partonic than for the hadronic mode.

It is interesting to note that at a beam energy of about 10 *AGeV*, the ratio $\bar{\Omega}^+/\Omega^-$ is about 10 times higher than the ratio $\bar{\Xi}^+/\Xi^-$, which is again 10 times higher than the ratio $\bar{\Lambda}^0/\Lambda^0$. This effect might indicate that at low beam energies, production of multi-strange antihyperons strongly depends on multiple collisions of partons or hadrons, production of which are enhanced at high densities. Multi-strange antihyperons are, therefore, very promising diagnostic probes of the density reached in the fireball and hence, of the equation-of-state of dense QCD matter.

6.3.2 Excitation function of hyperon to pion ratios

The ratios of average yields of strange particle relative to average yields of pions provide information on the production of strange quarks in comparison to the production of u and d quarks. The observation of an enhanced production of strange quarks is considered to be a prominent signature of the formation of the partonic medium. A famous example is the so called “horn”, which was observed in the excitation function of the K^+/π^+ ratio at a beam energy ≈ 30 *AGeV* in central Pb+Pb collisions [61]. It was suggested that this structure is an indication for the onset of deconfinement [61, 176].

In order to study excitation functions of hyperon to pion ratios we have calculated the average yields of pion as function of beam energy using different models. The average multiplicities of π^+ and π^- for central Au+Au collisions as function of beam energy are exhibited in Fig. 6.4. It can be seen that these models reproduce the experimental data points within 20 - 30% difference,

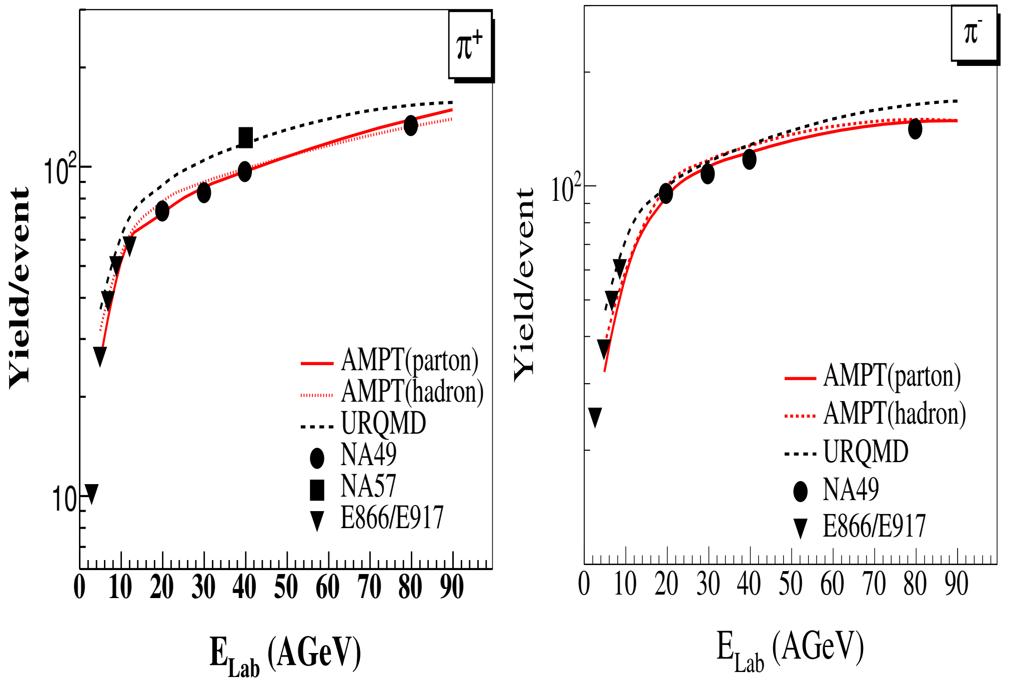

(a) *(b)*

Fig. 6.4 Average multiplicities of π^+ and π^- mesons for central Au+Au collisions as a function of beam energy. Lines are results of model calculations. The symbols represents experimental data (AGS and NA49) [61, 177–179].

but AMPT (parton) approach leads to relatively better agreement with the experimental data.

The ratios of average yields of hyperons and antihyperons relative to pion average yields for central Au+Au collisions are shown in Figs. 6.5 and 6.6. The pion mean multiplicity is defined as $\pi = 1.5 \times (\pi^+ + \pi^-)$ to take into account neutral pions. In the Λ^0/π ratio all models exhibit a peak-like structure at a beam energy slightly more than 10 $AGeV$, followed by a decrease of the ratios towards higher beam energies, reflecting the decreasing baryon chemical potential. The same feature is seen in the case of the ratios Ξ^-/π and Ω^-/π for the AMPT (hadronic) version, whereas, UrQMD model predicts a rise followed by a saturation. Below beam energies of about 20 $AGeV$, the partonic mode of the AMPT code predicts a clear enhancement of multi-strange hyperon production in comparison to those for the hadronic mode, suggesting that

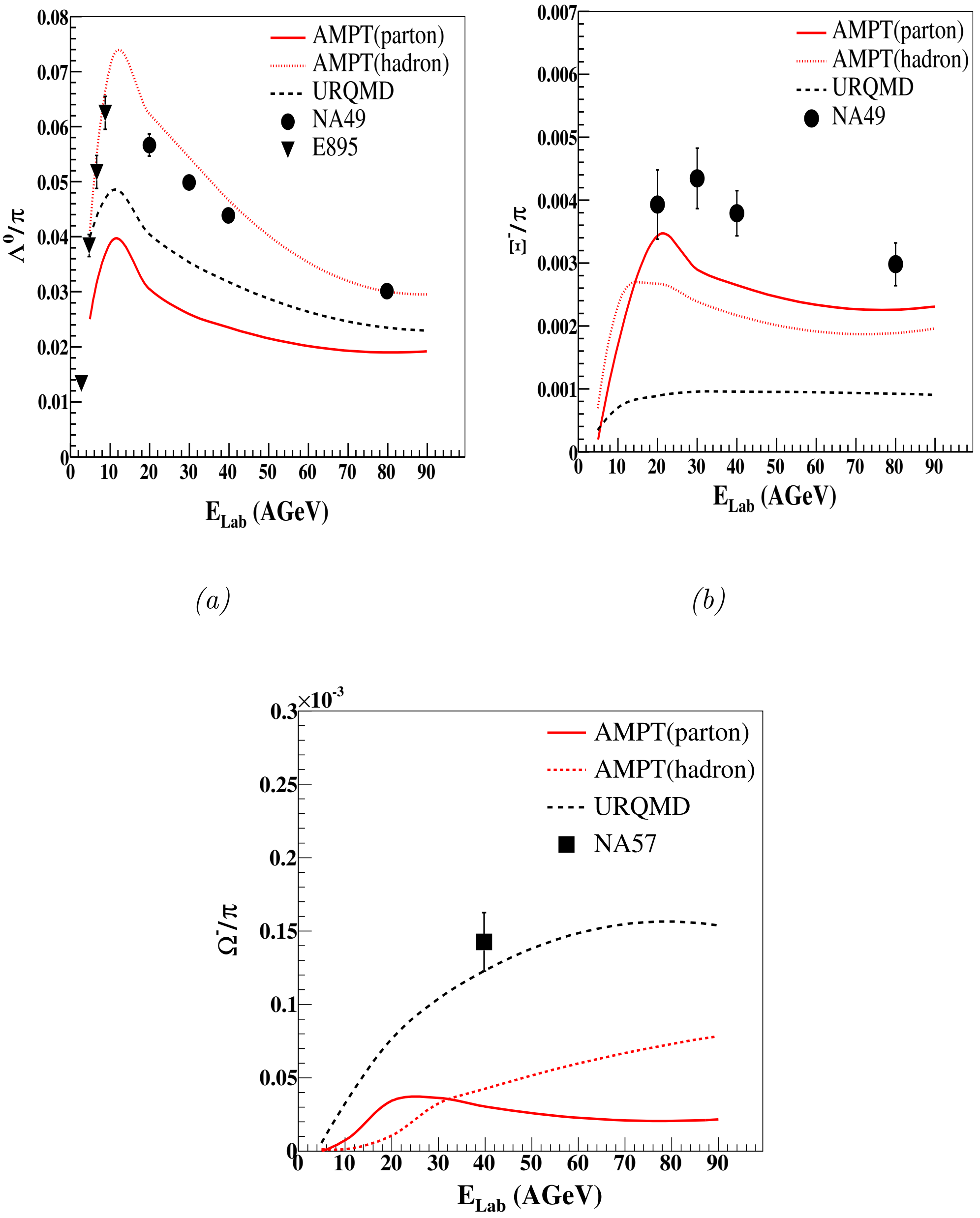

(a) *(b)*

(c)

Fig. 6.5 Ratios of the average yields of Λ^0, Ξ^- *and* Ω^- *relative to pion* (π = *1.5* $\times$ $(\pi^+ + \pi^-)$*) average yields for central Au+Au collisions as function of beam energy calculated by using different models and compared with the corresponding experimental data.*

multi-strange particles are a sensitive probe of QCD matter at large baryon densities. It may be interseting to note that no peak-like structure is found in the ratios of average yields of antihyperons relative to average yields of pion as reflected in Fig. 6.6. UrQMD model underpredicts the experimental data,

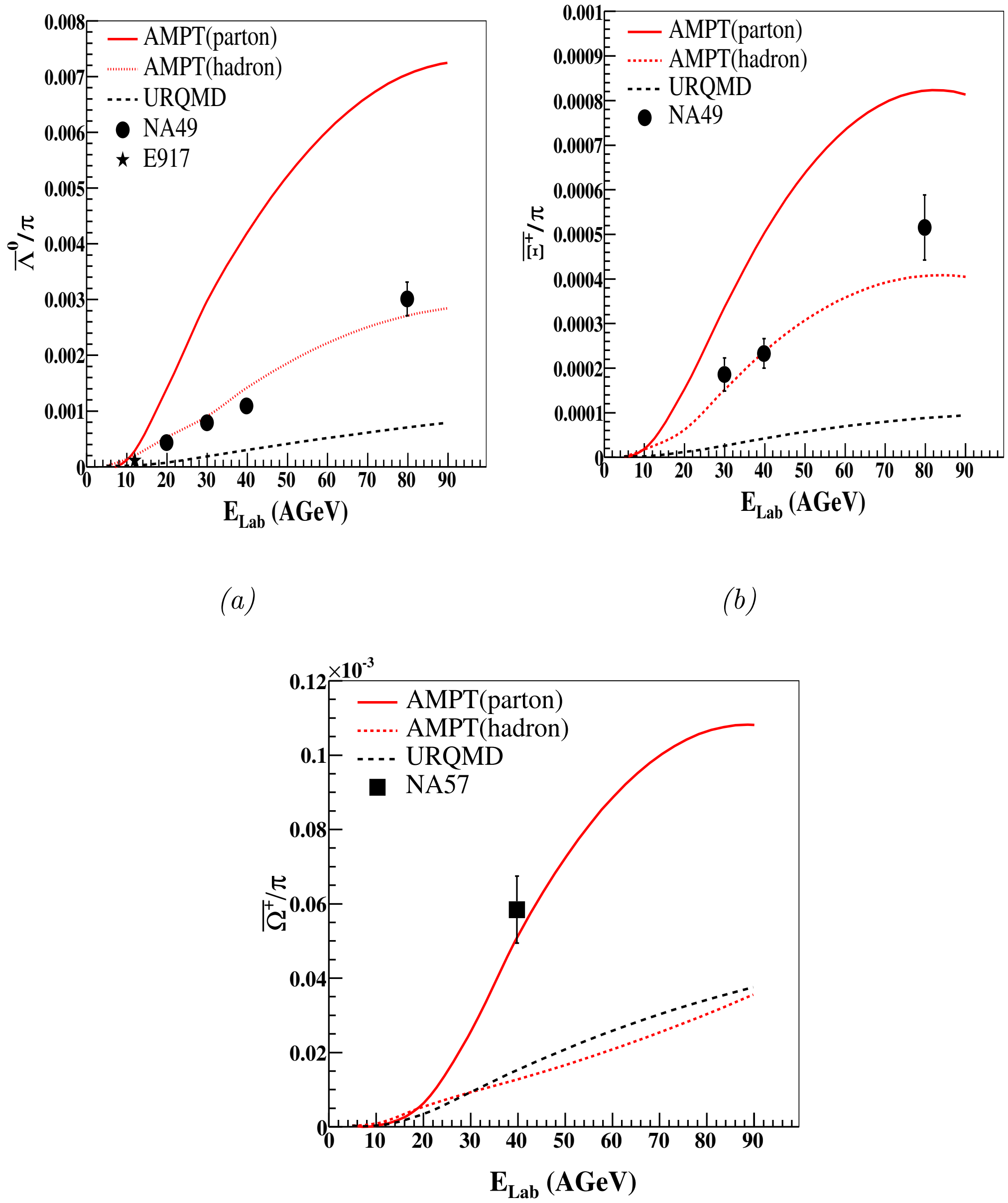

(a) *(b)*

(c)

Fig. 6.6 Ratios of the average yields of $\bar{\Lambda}^0$ *and* $\bar{\Xi}^+$, $\bar{\Omega}^+$ *and pion (with* $\pi = 1.5 \times (\pi^+ + \pi^-)$*) average yields for central Au+Au collisions as function of beam energy predicted by different models and compared with the available experimental data.*

whereas AMPT (partonic mode) overshoots the existing data. In the hadronic version, the AMPT code overpredicts the $\bar{\Lambda}^0/\pi$ ratio, but reproduces very well the few existing data sets on the $\bar{\Xi}^+/\pi$ and $\bar{\Omega}^+/\pi$ ratios.

6.4 Discussion

Measurement of the yields of strange particles in nuclear collisions at FAIR energies are quite important for studying the properties of the colliding systems. Earlier experiments revealed that production of s and $\bar{s}$ quarks and hence strange mesons and baryons would increase in the deconfined medium. The yields of multi-strange hyperons would also increase by exchange mechanism predominantly in the medium with higher baryon contents. Very high net baryon density in nuclear collisions at FAIR energies, coupled with the enhanced production of strange baryons by charge exchange reaction are envisaged to play significant role in studying the production of multi-strange hadrons. Hence, simulations have been performed for strange baryon production in central Au + Au collisions as a function of beam energy using different transport codes, and have compared the results with the available data. The results of the calculations agree reasonably well with data on Λ^0 and $\bar{\Lambda}^0$, which have been measured over a large beam energy range by several experiments. For multi-strange hyperons, however, poor scare data is available and the results of the models calculations differ by one order of magnitude. This is particularly true for beam energies below 30 $AGeV$, where the highest net baryon densities are expected to reach. It is also observed that production of antihyperons are more enhanced in the partonic mode as compared to the enhancement of hyperons, the trend is quite opposite in AMPT (hadronic) mode. Nevertheless, the predictions of the AMPT code indicates that the production of multi-strange hyperons is considerably enhanced in the partonic mode as compared to those for the hadronic scenario at beam energies up to 20 $AGeV$. These particles, therefore, seem to be a very promising observable, which may help to shed light on the degrees of freedom of QCD matter in neutron star core densities. The experimental verification of these predictions requires a detector system which can be operated at extremely high reaction rates in order to compensate the small production cross sections for multi-strange hyperons and antihyperons in the beam energy range up to 20 $AGeV$. To meet these requirements the

Compressed Baryonic Matter (CBM) detector system is being designed at FAIR.

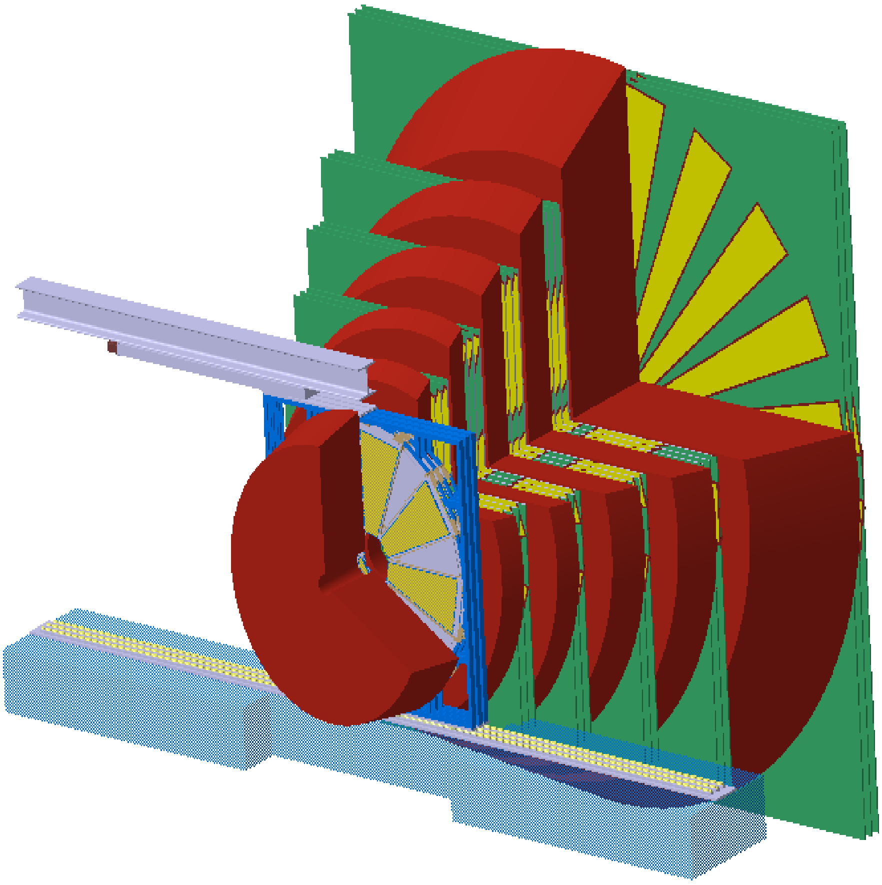

Summary and Outlook

Chapter 7

Summary and Outlook

Heavy-ion beams of widely different energies, being delivered by the present-day accelerators, are providing promising probes to explore QCD phase diagarm of strongly interacting nuclear matter under extreme conditions of temperature and/or net baryon density. One of the upcoming accelerator facilities will be created at FAIR, GSI, Darmstadt, Germany. The two complex synchrotron facilities at FAIR with bending powers of 100 (SIS100) and 300 (SIS300) Tm respectively, will deliver high intensity beams of protons of energies up to 89 GeV, light ions of up to 45 $AGeV$ energies and heavy-ions of energies up to 35 $AGeV$. The beams to be supplied by these two accelerators offer the most outstanding research opportunities in multifarious fronts of scientific program.

The heavy-ion beams of unprecedented quality, highest intensities and widely different energies at FAIR are envisaged to lead to production of the compressed nuclear matter in the laboratory, termed as Compressed Baryonic Matter. The CBM experiment is focused predominantly on the investigation of the QCD phase diagram in the domain of moderate temperatures and high net baryon densities. The CBM experiment is designed for detecting signals coming from the early and dense stage of relativistic heavy-ion collisions and offers an unique opportunity to investigate the signatures of partonic degrees of freedom and to locate the conjectured onset of the first order deconfinement phase transition and QCD critical point. These signals are rarely produced, either due to low cross section or small branching ratio into lepton pairs created via decays of LMVM or charmonia. The CBM experimental program, therefore, requires heavy-ion beams of unprecedented intensities to be supplied from the accelerators at FAIR and very fast detectors capable of handling high collision rates.

Till date, experimental data on dileptons, originating from the decays of LMVM or charmonia are not available in the energy range, 10 - 40 $AGeV$. For the first time, CBM experiment at FAIR, is planning to perform a detailed study of the production of dileptons in heavy-ion nuclear collisions at beam energies, E_{Lab} = 2 - 40 $AGeV$. Measurement of dielectrons, and dimuons, will provide a comprehensive information on dilepton radiation off dense baryonic matter. For measuring dimuons, **Muon Chambers** (MuCh) are being fabricated at CBM; its design and fabrication is the joint responsibility of the Russia and Indian groups involved in the CBM Collaboration.

The most critical experimental challenge of measuring muons in heavy-ion collisions in the FAIR energy regime is identification of low momenta muons created in the decays of LMVM in the environment of high particle density. Hence, a systematic simulation study has been done for optimizing the geometry and pad sizes of the muon chambers. The CBM muon detector system consists of a segmented absorber with triplets of tracking chambers based on GEM technology. Optimizations of MuCh geometry has been done in terms of the materials of the absorbers, their thicknesses, thickness of the gap between the absorbers and the detector chambers, detector granularity, etc. The optimizied detector has carbon as its first absorber with thickness of 60 cm and iron for other absorbers. The total thickness of the MuCh system is 1.2 m for LMVM and 2.25 m for charmonia measurements. The total thickness equivalent to a nuclear interaction length of 7.5 λ_I for LMVM and 13.5 λ_I for charmonia. The triplets of tracking chambers are located in between the absorbers with air gaps of thickness 30 cm. The acceptance of the detector is 5 - 25 ° and covers the region from mid-rapidity towards forward rapidity due to absorption of soft muons in the absorbers of the detector.

The optimized MuCh set-up is used for measuring LMVM embedded in the background, comprising high momenta hadrons, secondary muons and electrons, which arise from the decays of pions and kaons and ghost tracks, at the lowest energy (SIS100). Entire simulation chain for the selection of dimuon track candidates within a realistic scenario is discussed. The reconstructed invariant mass spectrum clearly shows a distinct peak above the continuum of background, suggesting that even at the lowest energy, there seems to be no inexpensive version of the MuCh set-up capable of the measurement LMVM.

Segmentation optimization has been done in order to evaluate an appropriate value of the segmentation angle of the pads. It is found that the hit density decreases and occupancy increases with segmentation angle. Smaller segmentation angles lead to pads of smaller size. Thus, single particle will fall on single pads, thereby increasing the number of hits and the hit density. As the segmentation angle increases some of the hits are lost in the clustering and result in a decrease of the hit density. However, an increase in the segmentation angle will lead to decrease in the number of pads, thereby increasing the occupancy of the detector. For the fabrication of the MuCh detector, the hit density should be low for proper handling by the detector with an occupancy of $\sim 5\%$. These requirements are met if the segmentation angle is 0.7 or 1 °.

The height of the peak of the invariant mass spectrum of ω^0 mesons decreases and that of the background increases with the segmentation angle and efficiency and signal to background ratio decreases with segmentation angle. Maximum efficiency and signal to background ratio and the minimum pad size of dimensions : $3.5\ mm \times 3.5\ mm$ or 1° azimuthal angle are the optimal choices; pads of this size are relatively easier and cheaper to fabricate. A real-size GEM detector prototype based on the above mentioned optimized parameters has been developed at VECC, Kolkata and tested. A realistic MuCh detector set-up with Straw Tubes and TRD as the last station and inclusion of various infrastructures such as cables, cooling lines, crates, etc., are the issues for future studies.

Measurement of the yields of strange particles in nuclear collisions at

FAIR energies are quite important for studying the properties of the colliding systems. Earlier experiments revealed that production of s and $\bar{s}$ quarks and hence strange mesons and baryons would increase in the deconfined medium. The yields of multi-strange hadrons would also increase by exchange mechanism, predominantly in the medium with higher baryon contents. Very high net baryon density in nuclear collisions at FAIR energies, coupled with the enhanced production of strange baryons by charge exchange reaction are envisaged to play important role in studying the production of multi-strange hadrons. Hence, simulations have been performed for strange baryon production in 1 million events of central Au+Au collisions as a function of beam energy using different transport codes (AMPT and UrQMD), and the results have been compared with the available data. The simulation results compare reasonably well with data on Λ^0 and $\bar{\Lambda}^0$, which have been measured over a wide beam energy range by several experiments. For multi-strange hyperons, however, poor scare data is available and the results of the models calculations differ by one order of magnitude. This is particularly true for the beam energies below 30 $AGeV$, where the highest net baryon densities are expected to exist.

It is observed that productions of antihyperons is more enhanced in the AMPT (partonic) mode in comparison to the enhancement of production of hyperons. An opposite trends is observed in AMPT (hadronic) mode. Nevertheless, the predictions of the AMPT codes indicate that the production of multi-strange hyperons is significantly enhanced in the partonic in comparison to the hadronic scenario at beam energies, up to 20 $AGeV$. These particles, therefore, seem to be very promising observables which shed light on the degrees of freedom of QCD matter in neutron star core densities. Experimental verification of these predictions requires a detector system which may be operated at extremely high reaction rates in order to compensate the small production cross sections of multi-strange hyperons and antihyperons in the beam energy range up to 20 $AGeV$. Such an experimental set-up - the CBM detector system, is being designed and fabricated at FAIR.

Appendix A

List of Acronyms

Table A.1 A collection of some important acronyms

Acronyms	Explanation
ADC	Analogue to Digital Converter
AGS	Alternating Gradient Synchrotron
AMPT	A Multi-Phase Transport model
APPA	Atomic, Plasma Physics and Application
ASIC	Application-Specific Integrated Circuit
BES	Beam Energy Scan
BNL	Brookhaven National Laboratory
CBM	Compressed Baryonic Matter
CDF	Collider Detector at Fermilab experimental collaboration
CEA	Commissariat *é l′*EnergieB Atomique collaboration
CERES	Cherenkov Ring Electron Spectrometer
CERN	Conseil Europ*é*en pour la Recherche Nucl*é*aire
CMS	Compact Muon Solenoid
CR	Collector Ring
DAQ	Data AcQuisition
DGLAP	Dokshitzer-Gribov-Lipatov-Altarelli-Parisi
DLS	DiLepton Spectrometer
DØ	DZero experiment
ECAL	Electromagnetic CALorimeter
EOS	Equation Of State
ESR	Experimental Storage Ring
FAIR	Facility for Antiproton and Ion Research
FLUKA	FLUktuierende KAskade
GEANT	GEometry ANd Tracking
GEM	Gas Electron Multiplier
GSI	Gesellschaft f*ü*r Schwerionenforschung
HADES	High Acceptance DiElectron Spectrometer
HESR	High-Energy Storage Ring
HSD	Hadron-String Dynamics model
IHEP	Institute of High Energy Physics
JINR	Joint Institute for Nuclear Research
LHC	Large Hadron Collider

Acronyms	Explanation
LD	Limited by Luminosity
LL	Limited by Detector
LMVM	Low Mass Vector Meson
MAPD	Multi-Avalanche Photo-Diodes
MAPMTs	Multi-Anode Photon Multiplier Tubes
MAPS	Mono-lithic Active Pixel Sensors
MC	Monte Carlo
MIP	Minimum Ionizing Particles
MPD	Multi-Purpose Detector
MRP	Multi-gap Resistive Plate Chambers
MuCh	Muon Chamber system
MVD	Micro-Vertex Detector
MWPC	Multi-Wire Proportional Chamber (Counter)
NESR	New Experimental Storage Ring
NDF	Number of Degree of Freedom
NICA	National Interscholastic Cycling Association
NN	Nearest-Neighbour
NUSTAR	NUclear STucture and Astrophysics and Reactions
PANDA	anti-Proton ANnihilation at DArmstadt
PHENIX	Pioneering High Energy Nuclear Interaction EXperiment
PHSD	Parton-Hadron-String Dynamics
PLUTO	event generator for hadronic interactions
PMT	Photon Multiplier Tube
PSD	Projectile Spectator Detector
PYTHIA	event generator for hadronic interactions
QCD	Quantum ChromoDynamics
QED	Quantum ElectroDynamics
QGP	Quark-Gluon Plasma
RESR	Recycled Experimental Storage Ring
RF	Radio Frequency system
RHIC	Relativistic Heavy Ion Collider
RICH	Ring Imaging CHerenkov detector
RPC	Resistive Plate Chamber
ROOT	Rapid Object-Oriented Technology
S/B	Signal to Background
SIS	SchwerIonen Synchrotron
SLAC	Stanford Linear Accelerator Center
SHINE	SPS Heavy Ion and Neutrino Experiment
SPS	Super Proton Synchrotron
sQGP	strongly coupled Quark-Gluon Plasma
STAR	Solenoidal TrAckeR
STS	Silicon Tracking System
Super-FRS	Superconducting FRagment Separator
TOF	Time Of Flight
TRD	Transition Radiation Detector
UNILAC	UNIversal Linear Accelerator
UrQMD	Ultra relativistic Quantum Molecular Dynamics
WLS	WaveLength Shifting

Appendix B

Kinematical variables

A brief definition of various kinematical variables used for dimuon analysis are given in this section.

In high-energy experiments, a physical quantity termed as rapidity,y is defined as

$$Y_L = \frac{1}{2}\log\frac{E+p_z}{E-p_z} \tag{B.1}$$

where E is the total energy and p_z represents longitudinal component of three-momenta. In the case of dimuon analysis, the total energy for the dimuon is represented as sum of the energy of the positive and negative muon, $E = E_1 + E_2$ and $p_z = p_{z,\mu_1} + p_z, \mu_2$ is the longitudinal component of three-momenta of dimuon.

A transformation of rapidity from laboratory to centre-of-mass frame can take place as :

$$Y_{CM} = Y_L \ - \ Y^* \tag{B.2}$$

where Y_{CM} is the rapidity of the particle in centre-of-mass frame and is expressed as:

$$Y^* = \frac{1}{2}\log\frac{1+\beta_c}{1-\beta_c} \tag{B.3}$$

where β_c is the velocity of the center-of-mass of the colliding system in the laboratory and can be calculated from

$$\beta_c = \frac{|\vec{p}_{Lab}|}{E_{Lab}} = \frac{|\vec{p}_{Beam}|}{E_{Beam} + m_{inc}} \tag{B.4}$$

where $\vec{p}_{Beam}$ and E_{Beam} are the projectile three-momentum and total energy and m_{inc} is the mass of the target.

The 4-momentum vector for single muon is defined as :

$$P_\mu = (E_\mu, \vec{p_\mu}) \tag{B.5}$$

where E_μ ($= \sqrt{m_\mu^2 + \vec{p}_\mu^2}$) is the total energy of a single muon track and $\vec{p_\mu}$ is its three momentum.

The 4-momentum for dimuon can be constructed from a single muon and is expressed as:

$$P_{\mu_1\mu_2} = P_{\mu_1} + P_{\mu_2} = (E_\mu 1 + E_\mu 2, \vec{p}_{\mu_1} + \vec{p}_{\mu_2}) \tag{B.6}$$

This formulation can be used to construct the invariant mass, m_{inv}, of a dimuon pair produced by the decay of LMVM and charmonia at rest, which due to energy-momentum conservation should be equal to the rest mass of the parent particle. The invariant mass formula is

$$m_{inv}^2 = P_{\mu_1\mu_2}^2 = (E_\mu 1 + E_\mu 2)^2 - (\vec{p}_{\mu_1} + \vec{p}_{\mu_2})^2 \tag{B.7}$$

$$m_{inv}^2 = 2m_\mu^2 + 2(E_1 E_2 + \vec{p}_{\mu_1}\vec{p}_{\mu_2}) \tag{B.8}$$

$$m_{inv} = \sqrt{2m_\mu^2 + 2(E_1 E_2 + \vec{p}_{\mu_1}\vec{p}_{\mu_2})} \tag{B.9}$$

where m_μ = 105 MeV is the rest mass of the muon. Being norm of a 4-vector m_{inv} is invariant under Lorentz transformation.

Apart from m_{inv} for dimuon other kinematical variables measured for the muon pairs are pair p_T, pair azimuthal angle, ϕ, etc. . The pair p_T is defined as

$$p_{T},_{\mu_1\,\mu_2} = \sqrt{p_x^2,_{\mu_1\,\mu_2} + p_y^2,_{\mu_1\,\mu_2}} \tag{B.10}$$

where $p_i,_{\mu_1\,\mu_2} = p_i,_{\mu_1} + p_i, \mu_2$ is the total three-momentum corresponding to i = x,y,z.

Bibliography

[1] Andrew Robert Steere. *A TIMELINE OF MAJOR PARTICLE ACCELERATORS*. Master's thesis, Michigan State University, United States, 2005.

[2] M. Breidenbach et al. *Phys. Rev. Lett.* **23**, 935, (1969).

[3] M. Gell-Mann. *Phys. Lett.* **8**, 214, (1964).

[4] G. Zweig. Technical Report CERN-TH-401, CERN, Geneva, Jan (1964).

[5] G. Zweig. Technical Report CERN-TH-412, NP-14146, PRINT-64-170, (1964).

[6] Particle Data Group. *"Particle Physics Booklet"*. (2014). http://pdg.lbl.gov/2014/download/rpp-2014-booklet.pdf.

[7] R. Michael Barnett, Henry Muehry, Helen R. Quinn, G.J. Aubrecht, R.N. Cahn, J. Dorfan, M. Dresden, G. Goldhaber, J.D. Jackson, and K. Olive. *The Charm of Strange Quarks: Mysteries and Revolutions of Particle Physics*. Springer, (2012). ISBN 1468495100,9781468495102.

[8] D. H. Perkins. *Introduction to High Energy Physics*. Cambridge University Press, 4^{th} edition edition, (2000). ISBN 0521621968.

[9] G. P. Salam. *CERN Yellow Report CERN-2010-002*. page 45, (2011). http://arxiv.org/abs/1011.5131.

[10] D. J. Gross and F. Wilczek. *Phys. Rev. Lett.* **30**, 1343, (1973).

[11] H. D. Politzer. *Phys. Rev. Lett.* **30**, 1346, (1973).

[12] H. Satz. *Nucl. Phys.* **A418**, 447c, (1984).

[13] K. Schweda et al. *arXiv:nucl-ex/0610043 v1.* 30 October (2006).

[14] K. Fukushima and T. Hatsuda. *Rept. Prog. Phys.* **74**, 014001, (2011).

[15] J. Adams et al (STAR Collaboration). *Nucl. Phys.* **A757**, 102, (2005).

[16] Y. Aoki et al. *Nature.* **443**, 675, (2006).

[17] A. Basavov et al. *Phys. Rev.* **D85**, 054503, (2012).

[18] Z. Fodor and S.D. Katz. *JHEP.* **0404**, 050, (2004).

[19] A. Basavov et al. *Nucl. Phys.* **A837**, 65, (2010).

[20] M. Alford. *Annual Review of Nuclear and Particle Science.* **51**, 131, (2001).

[21] J. Letessier and J. Rafelski. *Hadrons and Quark-Gluon Plasma.* Cambridge University Press, (2002).

[22] J. D. Bjorken. *Phys. Rev.* **D27**, 140, (1983).

[23] E. V. Shuryak. *Phys. Lett.* **B78**, 150, (1978).

[24] S. Salur. *Investigation of Hadronic Resonances with STAR.* PhD thesis, Yale, 2006.

[25] N. S. Amelin, E. F. Staubo, L. P. Csernai, V. D. Toneev, K.K. Gudima, and D. Strottman. *Phys. Lett.* **B261**, 52, (1991).

[26] L. P. Csernai. *Introduction to Relativistic Heavy Ion Collisions.* Wiley, (2008). ISBN 0471934208.

[27] http://www.gsi.de/zukunftsprojekt/indexe.html.

[28] C. Y. Wong. *Introduction to High-Energy Heavy-Ion Collisions.* World Scientific Publishing Company, (1994).

[29] T. Matsui and H. Satz. *Phys. Lett.* **B178**, 416, (1986).

[30] J. Rafelski et. al. *Phys. Rev. Lett.* **48**, 1066, (1982).

[31] Helmut Satz Sourav Sarkar and Bikash Sinha. volume Lecture Notes in Physics 785. (2010).

[32] J. Y. Ollitrault. *Phys. Rev.* **D46**, 229, (1992).

[33] S. Voloshin and Y. Zhang. *Zeitschrift für Physik.* **70**, C665, (1996).

[34] D. Teaney. *Quark-Gluon Plasma 4.* World Scientific, Singapore, (2010).

[35] J. Nagle, P. Steinberg, and W. Zajc. *Phys. Rev.* **C81**, 024901, (2010).

[36] M.M. Aggarwal et al. (WA98 Collaboration). *Phys. Rev.* **C65**, 054912, (2002).

[37] S. Jeon and V. Koch. *Phys. Rev. Lett.* **85**, 2076, (2000).

[38] E. V. Shuryak and M.A. Stephanov. *Phys. Rev.* **C63**, 064903, (2001).

[39] Jan-e Alam Bedangadas Mohanty and Tapan K. Nayak. *Phys. Rev.* **C67**, 024904, (2003).

[40] H. Heiselberg. *Phys. Rep.* **161**, (2001).

[41] S. Jeon and V. Koch. *Phys. Rev. Lett.* **83**, 5435, (1999).

[42] S. Jeon and V. Koch. *Phys. Rev. Lett.* **85**, 2076, (2000).

[43] S. Gavin and C. Pruneau. *Phys. Rev.* **C61**, 044901, (2000).

[44] J. Adams et al. (STAR Collaboration). *Phys. Rev.* **C68**, 044905, (2003).

[45] J. Adams et al. (STAR Collaboration). *Phys. Rev.* **C71**, 064906, (2005).

[46] H. Appelshäuser et al. (NA49 Collaboration). *Phys. Lett.* **B459**, 679, (1999).

[47] A. Peikert F. Karsch, E. Laermann. *Nucl. Phys.* **B605**, 579, (2001). http://arxiv.org/pdf/hep-lat/0012023v1.

[48] K. Redlich P.Braun Munzinger and J. Stachel. (2003). http://arxiv.org/abs/nucl-th/0304013.

[49] M. C. Abreu et al. (NA50 Collaboration). *Phys. Lett.* **B450**, 456, (1999).

[50] L. Ramello. *Nucl. Phys.* **A774**, 59, (2006).

[51] R. Arnaldi (NA60 Collaboration). *Nucl. Phys.* **A783**, 261, (2007).

[52] R. Vogt, P. Koch M. Prakash, and T. H. Hansson. *Phys. Lett.* **B207**, 263, (1988).

[53] S. Gavin, M. Gyulassy, and A. Jackson). *Phys. Lett.* **B207**, 257, (1988).

[54] K. Adcox et al. (PHENIX Collaboration). *Nucl. Phys.* **A757**, 184, (2005).

[55] J. Adams et al. (STAR Collaboration). *Nucl. Phys.* **A757**, 102, (2005).

[56] B.B.Back et al. (PHOBOS Collaboration). *Nucl. Phys.* **A757**, 28, (2005).

[57] J. Adams et al. (STAR Collaboration). *Phys. Rev. Lett.* **91**, 072304, (2003).

[58] Y. Zhang. *J. Phys.* **G35**, 104022, (2008).

[59] J. Adams et al. (STAR Collaboration). *Phys. Rev. Lett.* **92**, 052302, (2004).

[60] S. S. Adler et al. (PHENIX Collaboration). *Phys. Rev. Lett.* **91**, 182301, (2003).

[61] C. Alt et al. (NA49 collaboration). *Phys. Rev.* **C77**, 024903, (2008).

[62] J. Cleymans et al.. *Phys. Rev.* **C60**, 054908, (1999).

[63] P. Braun-Munzinger et al. *Nucl. Phys.* **A697**, 902, (2002).

[64] E. L. Bratkovskaya et al. *Phys. Rev.* **C69**, 054907, (2004).

[65] A. Andronic, P. Braun-Munzinger, and J. Stachel. *Phys. Lett.* **B673**, 054907, (2009).

[66] P. Braun-Munzinger and J. Stachel. *Phys. Lett.* **B490**, 196, (2000).

[67] I. Augustin. Accelerator and Scientific Infrastructure. Technical report, Dec. (2006). https://www-alt.gsi.de/documents/DOC-2006-Dec-94.html.

[68] FAIR Joint Core Team. Green paper - fair modularized start version. Technical report, Nov. (2009). https://www-alt.gsi.de/documents/DOC-2009-Nov-124.html.

[69] B. Friman et al. *The CBM physics book: Compressed Baryonic Matter in Laboratory Experiments*, volume 814. (2011). ISBN 978-3-642-13292-6.

[70] A.D. Kovalenko. Status of the nuclotron. *proceedings of EPAC94.* **161**, (1995).

[71] Oliver Boine-Frankenheim. The fair accelerators: Highlights and challenges. *Conf. Proc.* **C100523**, (2010).

[72] I. Augustin. Btr_accelerator and scientific infrastructure. Technical report, July (2006). https://www-alt.gsi.de/documents/DOC-2006-Jul-40.html.

[73] P. J. Spiller et al. *Design Status of the FAIR Synchrotrons SIS100 and SIS300 and the High-Energy Beam Transport System.* volume C0806233, (2008).

[74] S. Chattopadhyay. *Nucl. Phys.* **A931**, 267, (2014).

[75] I. C. Arsene. *Phys. Rev.* **C75**, 034902, (2007).

[76] S.A. Bass et al. *Prog. Part. Nucl. Phys.* **41**, 255, (1998).

[77] http://www.fair-center.eu/for-users/experiments/cbm/introduction.html.

[78] D.H. Rischke, S. Bernard, and J.A. Maruhn. *Nucl. Phys.* **A595**, 346, (1995).

[79] D.H. Rischke, Y. Pursun, and J.A. Maruhn. *Nucl. Phys.* **A595**, 383, (1995).

[80] A. Andronic, P. Braun-Munzinger, and J. Stachel. *Nucl. Phys.* **A167**, 772, (2006).

[81] P. Braun-Munzinger and J. Stachel. *J. Phys.* **G21**, L17, (1995).

[82] J. Randrup and J. Cleymans. *Phys. Rev.* **C74**, 047901, (2006).

[83] J. Cleymans et al. *Phys. Rev.* **C73**, 034905, (2006).

[84] J. Randrup and J. Cleymans. *arXiv:0905.2824v1 [nucl-th].* (2009).

[85] C. Höehne. Physics of compressed baryonic matter. May (2012). https://www-alt.gsi.de/documents/DOC-2012-Dec-62.html.

[86] W. Cassing, E.L. Bratkovskaya, and A. Sibirtsev. *Nucl. Phys.* **A691**, 753, (2001).

[87] H. Sato et al. *Prog. Rep.* **43**, 180, (2010).

[88] H. Sato et al. *IEEE Trans. ASC.* **23**, 450030180, (2013).

[89] P. Akishin et al. CBM Progress Report 2013. Technical report, Darmstadt, (2014). http://www-alt.gsi.de/documents/DOC-2014-Mar-16-1.pdf.

[90] J. Heuser, W. Müller, V. Pugatch, P. Senger, C. J. Schmidt, C. Sturm, and U. Frankenfeld, editors. *[GSI Report 2013-4] Technical Design Report for the CBM Silicon Tracking System (STS).* GSI, Darmstadt, 2013. http://repository.gsi.de/record/54798.

[91] J. M. Heuser. *Nucl. Instrum. Meth.* **A582**, 910, (2007).

[92] C. Höhne et al. *Nucl. Instrum. Meth.* **A639**, 294, (2010).

[93] C. Höhne. Technical Design Report for the CBM Ring Imaging Cherenkov Detector. Technical report, (2010). http://repository.gsi.de/record/65526.

[94] MUCH Workgroup and the CBM Collaboration. Technical design report for the cbm muon chamber (much) detector. December (2013). https://www-alt.gsi.de/documents/DOC-2014-Nov-58.html.

[95] A. Akindinov et al. *Nucl. Instrum. Meth.* **A572**, 676, (2007).

[96] D. Kresan and C. Höhne. CBM Progress Report 2009. Technical report, Darmstadt, (2009). https://www-alt.gsi.de/documents/DOC-2010-Apr-17-1.pdf.

[97] T. Matsui and H. Satz. *Phys. Lett.* **B178**, 416, (1986).

[98] R. J. Porter et al. *Phys. Rev. Lett.* **79**, 1229, (1997).

[99] G . Agakishiev et al. *Phys. Rev.* **C84**, 014902, (2011).

[100] G. Agakishiev et al. *Eur. Phys. J.* **C41**, 475, (2005).

[101] /http://www.fair-center.eu/for-users/experiments/cbm.html.

[102] I. Fröhlich, T. Galatyuk, R. Holzmann, J. Markert, B. Ramstein, P. Salabura, and J. Stroth. *J. Phys.: Conf. Ser.* **219**, 032039, (2010).

[103] R. Brun et al. Geant3. *CERN/DD/EE/84-1, (1986).* long writeup W5013, (1993).

[104] S. Ahmad, P.P. Bhaduri, and H. Jahan et al.. *Nucl. Instrum. Meth.* **A775**, 139, (2015).

[105] R. Brun and F. Rademakers. Root - an object oriented data analysis framework.. *Nucl. Instrum. Meth.* **A389**, 81, (1997).

[106] S. Agostinelli et al. *Nucl. Instrum. Meth.* **A506**, 250, (2003).

[107] G. Battistoni et al. The fluka code: Description and benchmarking. volume 896, page 31, (2007).

[108] W. Cassing, E. Bratkovskaya, and S. Juchem.. *Nucl. Phys.* **A674**, 249, (2000).

[109] I. Smirnov. Heed simulation program for energy loss.

[110] I. Kisel. *Nucl. Instr. and Meth.* **A566**, 85, (2006).

[111] R. Kalman. *Journal of Basic Engineering Series.* **D82**, 35, (1960).

[112] R. Fruhwirth. *Nucl. Instr. and Meth.* **A262**, 444, (1987).

[113] C. Amsler et al. *Phys. Lett.* **B667**, 35, (2008).

[114] William H Press et al. *Numerical recipes : the art of scientific computing.* Cambridge University Press, third edition, (2007). ISBN 978-0-511-33555-6, 0-511-33555-5, 978-0-521-88068-8, 0-521-88068-8.

[115] R. Fruhwirth et. al. *Data Analysis Techniques for High-Energy Physic.* Cambridge University Press, second edition, (2000).

[116] Andrey Lebedev, Darmstadt Ososkov, Gennady [GSI, and Dubna] JINR. Lit track propagation for cbm, Dec. (2008). https://www-alt.gsi.de/documents/DOC-2008-Dec-182.html.

[117] http://pdg.lbl.gov/2014/listings/rpp2014-list-omega-782.pdf.

[118] J. Beringer et al. (Particle Data Group). "particle physics booklet". *Phys. Rev.* **D86**, 010001, (2012). http://pdg.lbl.gov/2014/listings/rpp2014-list-omega-782.pdf.

[119] S. Chattopadhyay at al. In *Proceedings of the DAE Symp. on Nucl. Phys. 56*, (2011).

[120] Hushnud et al. In *Proceedings of the DAE Symp. on Nucl. Phys. 58*, (2013).

[121] H. Ansari et al. Cbm progress report 2012. Technical report, Darmstadt, (2013). https://www-alt.gsi.de/documents/DOC-2013-Mar-49-1.pdf.

[122] H. Satz S. Sarkar and B. Sinha. *The Physics of the Quark Gluon Plasma.* Springer-Verlag Berlin Heidelberg, (2010). ISBN 978-3-642-02285-2, 978-3-642-02286-9.

[123] J. Rafelski and B. Müller. *Phys. Rev. Lett.* **48**, 1066, (1982).

[124] J. Rafelski. *Phys. Rep.* **88**, 331, (1982).

[125] W. Greiner P. Koch, J. Rafelski. *Phys. Lett.* **B123**, 151, (1983).

[126] B. Müller P. Koch and J. Rafelski. *Phys. Rep.* **142**, 167, (1986).

[127] J. Rafelski. *Nucl. Phys.* **A418**, 215c, (1984).

[128] T. S. Biro and J. Zimanyi. *Phys. Lett.* **B113**, 6, (1982).

[129] T. S. Biro and J. Zimanyi. *Nucl. Phys.* **A395**, 525, (1983).

[130] T. Matsui, B. Svetitsky, and L.D. McLerran. *Phys. Rev.* **D34**, 783, (1986).

[131] S. Uddin and C. P. Singh. *Phys. Lett.* **B278**, 357, (1992).

[132] E. Andersen et al. (WA97 Collaboration). *Phys. Lett.* **B449**, 401, (1999).

[133] F. Antinori et al. (NA57 Collaboration). *J. Phys.* **G32**, 427, (2006).

[134] F. Antinori et al. (NA57 Collaboration). *J. Phys.* **G32**, 045105, (2010).

[135] C. Alt et al. (NA49 Collaboration). *Phys. Rev. Lett.* **94**, 192301, (2005).

[136] C. Alt et al. (NA49 Collaboration). *Phys. Rev.* **C78**, 034918, (2008). http://arxiv.org/abs/0804.3770.

[137] T. Anticic et al. (NA49 Collaboration). *Phys. Rev. Lett.* **80**, 034906, (2009).

[138] J. Adams et al. (STAR Collaboration). *Phys. Rev. Lett.* **92**, 182301, (2004).

[139] J. Adams et al. (STAR Collaboration). *Phys. Rev. Lett.* **98**, 62301, (2007).

[140] B.I. Abelev et al. (STAR Collaboration). *Phys. Rev.* **C77**, 044908, (2008).

[141] C. Blume. *J. Phys.* **G31**, S57, (2005).

[142] M. Mitrovski. *J. Phys.* **G37**, 094003, (2010).

[143] B. B. Back et al (E917 Collaboration). *J. Phys.* **G27**, 301, (2001).

[144] C. Blume and C. Markert. *Prog. Part. Nucl. Phys.* **66**, 834, (2011).

[145] P. Senger and V. Friese (CBM Collaboration). Nuclear matter physics at sis-100, Feb (2012). https://www-alt.gsi.de/documents/DOC-2011-Aug-29.html.

[146] A. Andronic, P. Braun-Munzinger, and J. Stachel. *Phys. Lett.* **B673**, 142, (2009).

[147] A. Andronic, P. Braun-Munzinger, and J. Stachel. *Phys. Lett.* **B678**, 516, (2009).

[148] G. Agakishiev et al (HADES collaboration). *Phys. Rev. Lett.* **B103**, 132301, (2009).

[149] S. Chattopadhyay. *Nucl. Phys.* **A931**, 267, (2014).

[150] S.A. Bass et al. *Prog. Part. Nucl. Phys.* **41**, 255, (1998).

[151] M. Bleicher et al. *J. Phys.* **G25**, 1859, (1999).

[152] Z.W. Lin, C.M. Ko, B.A. Li, B. Zhanga, and S. Pal. *Phys. Rev.* **C72**, 064901, (2005).

[153] S. Soff, J. Randrup, H. Stöcker, and Nu Xua. *Phys. Lett.* **B551**, 115, (2003).

[154] C. Greiner. *AIP Conf. Proc.* **664**, 337, (2003).

[155] C. Greiner. *Heavy Ion Phys.* **14**, 149, (2001).

[156] C. Greiner. *J. Phys.* **G27**, L95, (2001).

[157] http://urqmd.org/download/.

[158] X. N. Wang and M. Gyulassy. *Phys. Rev.* **D44**, 3501, (1991).

[159] B. Zhang. *Comput. Phys. Commun.* **109**, 193, (1998).

[160] B. Andersson, G. Gustafson, and B. Soderberg. *Z. Phys.* **C20**, 317, (1983).

[161] T. S. Biro, P. Levai, and J. Zimanyi. *Phys. Lett.* **B347**, 6, (1995).

[162] T. S. Biro. *arXiv:hep-ph/0005067.* **82**, 74, (2000). http://www.thep.lu.se/tf2/staff/torbjorn/Pythia.html.

[163] J. Zimanyi, T. S. Biro, T. Csorgo, and P. Levai. *Phys. Lett.* **B472**, 243, (2000).

[164] J. Zimanyi, P. Levai, T. Csorgo, and T. S. Biro. *arXiv:hep-ph/0103156.* page 243, (2001).

[165] B. A. Li and C.M. Ko. *Phys. Rev.* **C52**, 2037, (1995).

[166] B. Li, A. T. Sustich, B. Zhang, and C.M. Ko. *Int. J. Mod. Phys.* **E10**, 267, (2001).

[167] Z. W. Lin and C. M. Ko. *Phys. Rev.* **C65**, 034904, (2002).

[168] Z. W. Lin, C. M. Ko, and S. Pal. *Phys. Rev. Lett.* **89**, 152301, (2002).

[169] Z. W. Lin and C. M. Ko. *J. Phys.* **G30**, S263, (2004).

[170] B. Zhang, C.M. Ko, B.A. Li, and Z.W. Lin. *Phys. Rev.* **C61**, 067901, (2000).

[171] Z.W. Lin, S. Pal, C.M. Ko, B.A. Li, and B. Zhang. *Phys. Rev.* **C64**, 011902(R), (2001).

[172] S. Pal, C.M. Ko, and Z. W. Lin. *Nucl. Phys.* **A730**, 143, (2004).

[173] P. Koch, B. Muller, and J. Rafelski. *Phys. Rept.* **142**, 167, (1986).

[174] http://personal.ecu.edu/linz/ampt/.

[175] F. Antinori et al. (NA57 Collaboration). *Phys. Lett.* **B595**, 68, (2004).

[176] M. Gazdzicki, M. Gorenstein, and P. Seyboth. *Acta Phys. Polon.* **B42**, 307, (2011).

[177] L. Ahle et al. (E866 and E917 Collaboration). *Phys. Lett.* **B476**, 1, (2000).

[178] L. Ahle et al. (E866 and E917 Collaboration). *Phys. Lett.* **B490**, 53, (2000).

[179] S. V. Afanasiev et al. (NA49 Collaboration). *Phys. Rev.* **C66**, 054902, (2002).

List of Publications

Journals

1. "Design of segmented-absorber based muon detection system for high energy heavy ion collision experiment."
   S. Ahmad, P. P. Bhaduri, **Hushnud Jahan**, A. Senger, R. Adak, S. Samanta, A. Prakash, K. Dey, A. Lebedev, E. Kryshen, S. Chattopadhyay, P. Senger, B. Bhattacharjee, S. K. Ghosh, M. Irfan, N. Ahmad, M. Farooq and B. K. Singh.
   Nuc. Inst. and Meth. A **775**, 139-147 (2015).

2. "Multi-Strange baryon production at FAIR energies."
   Hushnud Jahan, S. Ahmad, P. Senger, N. Ahmad, M. Farooq and S. Choudhury.
   Proceedings of ICPAQGP-2015.
   To be published in *Proceedings Of Science*, ItalyJournal.

3. "Some Aspects of Multiparticle Production in Relativistic Nuclear Collisions."
   M. I. Haque, M. Tariq, **Hushnud Jahan**, T. Hussain.
   JMP, **5**, 1353-1359 (2014).

4. "A Study of Multifractal Spectra and Renyi Dimensions in 14.5 AGeV/c ^{28}Si-Nucleus Collisions."
   N. Ahmad, A. Kamal, M. M. Khan, **Hushnud**, A. Tufail.
   JMP **5**, 1288-1293 (2014).

5. "Propagation of Fluctuations in Au+Au Collisions at FAIR energy."
   S. Ahmad, **Hushnud Jahan**, S. Chattopadhyay, M. Farooq, N. Ahmad and S. Bashir.
   Submitted for Review at *Phys. Rev. C*, August (2014);
   e-Print: arXiv:1408.5107 [hep-ph].

6. "Production of multi-strange hyperons at FAIR energies."

   Hushnud Jahan, S. Ahmad, P. Senger, N. Ahmad, M. Farooq and S. Choudhury.

   Submitted for Review at *Phys. Rev. C* (2015).

Conference Proceedings

1. "Multifractality in Multiparticle Production in 4.5 and 14.5A GeV/c ^{28}Si-AgBr Collisions."

   N. Ahamd, Shakeel Ahmad, M. M. Khan and **Hushnud**. *Proceedings of the DAE Symp. on Nucl. Phys.* **59**, 732 (2014).

2. "Segmentation Optimization for dimuon detection system in CBM Experiment at FAIR."

   Hushnud, S. Ahmad and N. Ahmad.

   Proceedings of the DAE Symp. on Nucl. Phys. **58**, 748 (2013).

3. "On Multiplicity Correlations in Relativistic Nuclear Collisions."

   N. Ahamd, **Hushnud**, M. M. Khan, A. Kamal and A. Shakeel.

   Proceedings of the DAE Symp. on Nucl. Phys. **58**, 744 (2013).

4. "Dynamical fluctuations in multiplicity distribution of particles produced in relativistic nuclear collisions."

   M. Tariq, **Hushnud**, A. Kamal, Tahir Hussain, N. Ahmad, A. R. Khan and M. M. Khan.

   Proceedings of the DAE Symp. on Nucl. Phys. **58**, 708 (2013).

5. "Scaling of charged particle multiplicity distrubutions in relativisitc nuclear collisions."

   N. Ahamd, **Hushnud**, M. M. Khan, M. D. Azmi, A. Tufail, M. Zafar and M. Irfan.

   Proceedings of the DAE Symp. on Nucl. Phys. **56**, 1022 (2011).

6. "Scaling behaviour of multiplicity distribution in relativistic nuclear collisions."

N. Ahmad, M. M. KHAN, **Hushnud Jahan**, A. KAMAL, Tariq Ahmad and M. ZAFAR.
Proceedings of ICPAQGP-2010 (2010).

Technical Reports

1. "Technical Design Report for the CBM, Muon Chamber (MUCH)". S. Chattopadhyay, V. P. Viyogi, A. K. Dubey, P .P. Bhaduri, **Hushnud Jahan** et.al.
   Approved by *ECE-FAIR*, 1-183, July (2015).

2. "Production of Omega hyperons at FAIR energies."
   Hushnud Jahan, S. Chattopadhyay and N. Ahmad.
   CBM Progress Report, **ISBN 978-3-9815227-2-3**, 141 (2014).

3. "Production of hyperons at FAIR energies."
   Hushnud Jahan, S. Chattopadhyay, P. Senger, N. Ahmad, and M. Irfan.
   CBM Progress Report, **ISBN 978-3-9815227-1-6**, 125 (2013).

4. "Segmentation optimization for the MUCH detector."
   Hushnud Jahan, N. Ahmad and M. Irfan.
   CBM Progress Report, **ISBN 978-3-9815227-0-9**, 44 (2012).